Low and high-order hybridised methods for compressible flows

Jordi Vila Pérez

UNIVERSITAT POLITÈCNICA DE CATALUNYA
PROGRAMA DE DOCTORAT EN MATEMÀTICA APLICADA

LABORATORI DE CÀLCUL NUMÈRIC (LaCàN)

LOW AND HIGH-ORDER HYBRIDISED METHODS FOR COMPRESSIBLE FLOWS

by

JORDI VILA PÉREZ

Doctoral Thesis
Advisors: Antonio Huerta
           Matteo Giacomini

Barcelona, November 2020

Abstract

Low and high-order hybridised methods for compressible flows

Jordi Vila Pérez

The aerospace community is challenged as of today for being able to manage accurate overnight computational fluid dynamics (CFD) simulations of compressible flow problems. Well-established CFD solvers based on second-order finite volume (FV) methods provide accurate approximations of steady-state turbulent flows but are incapable to produce reliable predictions of the full flight envelope. Alternatively, promising high-order discretisations, claimed to permit feasible high-fidelity simulations of unsteady turbulent flows, are still subject to strong limitations in robustness and efficiency, placing their level of maturity far away from industrial requirements. In consequence, the CFD paradigm is immersed at this point into the crossroads outlined by the inherent limitations of low-order methods and the yet immature state of high-order discretisations. Accordingly, this thesis develops a twofold strategy for the high-fidelity simulation of compressible flows introducing two methodologies, at the low and high-order levels, respectively, based on hybridised formulations.

First, a new finite volume paradigm, the face-centred finite volume (FCFV) method, is proposed for the formulation of steady-state compressible flows. The present methodology describes a hybrid mixed FV formulation that, following a hybridisation process, defines the unknowns of the problem at the face barycentres. The problem variables, i.e. the conservative quantities and the stress tensor and heat flux in the viscous case, are retrieved with optimal first-order accuracy inside each cell by means of an inexpensive postprocessing step without need of reconstruction of the gradients. Hence, the FCFV solver preserves the accuracy of the approximation even in presence of highly stretched or distorted cells, providing a solver insensitive to mesh quality. In addition, the FCFV method is a monotonicity-preserving scheme, leading to non-oscillatory approximations of sharp gradients without resorting to shock capturing or limiting techniques. Finally, the method is robust in the incompressible limit and is capable of computing accurate solutions for flows at low Mach number without the need of introducing specific pressure correction strategies.

In parallel, the high-order hybridisable discontinuous Galerkin (HDG) method is reviewed in the context of compressible flows, presenting an original unified frame-

work for the derivation of Riemann solvers in hybridised formulations. The framework includes, for the first time in an HDG context, the HLL and HLLEM Riemann solvers as well as the traditional Lax-Friedrichs and Roe solvers. The positivity preserving properties of HLL-type Riemann solvers are displayed, demonstrating their superiority with respect to Roe in supersonic cases. In addition, HLLEM specifically outstands in the approximation of boundary layers because of its shear preservation, which confers it an increased accuracy with respect to HLL and Lax-Friedrichs.

An extensive set of numerical benchmarks of practical interest is introduced along this study in order to validate both the low and high-order approaches. Different examples of compressible flows in a great variety of regimes, from inviscid to viscous laminar flows, from subsonic to supersonic speeds, are presented to verify the accuracy properties of each of the proposed methodologies and the performance of the introduced Riemann solvers.

Contents

List of Figures

xv

Chapter 1

Introduction

The rapid growth of computational resources during the last decades has entailed an increasing relevance of numerical simulations within engineering processes. The development of numerical methods, together with the increasing fidelity of physical models, has allowed computational analysis to become a driving technology not only for industrial development but also for scientific discovery.

The preeminent importance of numerical methods has been specially manifested in the aeronautical industry, where computational fluid dynamics (CFD) has revolutionised the process of aerodynamic design, as described by Johnson et al. (2005). In particular, as Ball (2008) points out, the introduction of CFD in design processes has relegated the costly and time-consuming wind tunnel experiments, predominant in the aerospace sector some decades ago, to validation phases. Because of the ability of CFD to provide predictions of numerous potential configurations at early stages of development, such technology has been widely accepted among engineers, allowing for an enhanced optimisation of final designs.

The uninterrupted growth of computing power over the last decades has driven computational strategies to a far greater extent than ever possible. The development of high-fidelity computational tools has been accompanied by the employment of more accurate models, implying a continuous change of the CFD paradigm, as stated by Kraft (2010). Such increasing complexity has boosted the potential of CFD to deliver a superior understanding and insight into the physics behind. For this reason, CFD has become a powerful technology not only for the development of new products but also for the inspection of new frontiers of knowledge.

1.1   Motivation and state of the art

The role of computational analysis in current research and development stages of aircraft design has been extensively reported by Malik and Bushnell (2012). The profound impact of CFD has been specially relevant on the aerodynamic design in cruise conditions, where the flow remains attached to the body and develops minimal turbulent separation. In those cases, accurate predictions can be obtained with the available tools, mostly based on second-order finite volume (FV) implementations of the Reynolds-averaged Navier-Stokes (RANS) equations. Accordingly, the introduction of these computational strategies has allowed for a substantial reduction of wind tunnel testing, now considered only for final configurations upon validation. Such decrease in wind tunnel experiments has already implied an important reduction of design costs and the fabrication of more efficient products in shorter cycle times.

However, other flight conditions still require experimental analyses for accurate evaluations. Cruise conditions only describe a small part of the flight envelope of a regular aircraft. For other phases, the presence of flow separation or other transient effects limits the application of computational analysis, which still cannot offer reliable predictions of the flowfield. In consequence, CFD is immersed in a double challenge for modelling such more complex flow phenomena within reasonable time. On the one hand, the availability of faster and more powerful machines, and, on the other, the development of more accurate numerical schemes.

The NASA CFD Vision 2030 Study by Slotnick et al. (2014) describes some mid and long-term perspectives of such aspects in CFD computation. For the first, high performance computing (HPC) is aimed at addressing the high demands on computational capacity imposed by complex CFD modelling. To this end, improvements in algorithm and hardware technologies are defined as necessary, enabling as well an evolution towards new programming paradigms based on a higher portability between HPC environments. Nonetheless, the complex challenges faced by CFD require as well a further development of more accurate numerical methods, high-fidelity physics-based models, advanced solvers, adaptivity schemes and management of uncertainties.

In particular, the modelling of separated and transitional turbulent flows remains an open problem for the CFD community. Traditional CFD solvers are still incapable to complete large-scale simulations of transient flows at high Reynolds numbers around complex geometric configurations. To this end, new models, such as

the large-eddy simulation (LES) method, or new highly accurate discretisations have been receiving increasing attention for their promising predictions of unsteady and turbulent flows.

1.1.1 The horizon of high-order methods within CFD

In recent years, high-order methods have experienced a growing interest within the CFD community because of their increased precision at reduced computational cost when compared to low-order counterparts. The claimed superiority of high-order methods has been supported by their low diffusion and dispersion errors, as described by Ekaterinaris (2005), which confer them a major advantage for the simulation of transient problems and transport phenomena.

Precisely, because of their promising potential to efficiently deliver high accuracy in unsteady vortex transport, recent trends in aerodynamics open the way to reliable and feasible LES runs, as introduced by Drikakis (2003) or Moura et al. (2015). This has prompted the extension of low-order strategies to high-order, such as the FV discretisations proposed by Cueto-Felgueroso et al. (2007) or Chassaing et al. (2013), or the stabilised finite element (FE) schemes employed by Chalot and Normand (2010) or Sevilla et al. (2013, 2017). In parallel, new discretisation methods, such as the discontinuous Galerkin (DG) method, popularised by Cockburn et al. (2000) or Arnold et al. (2002), among others, have been recently devised.

DG formulations have become one of the most adopted high-order approaches within the computational engineering community, see for instance Cockburn et al. (1989a), Cockburn and Shu (1998c) or Bassi and Rebay (1997a, 2002). In particular, DG discretisations have been often seen as a methodology to combine the advantages of both FV and FE schemes. On the one hand, contrary to FV methods, DG methods allow to define high-order local approximations. On the other, the stabilisation term required for solving convection dominated problems is easier to define when compared to traditional stabilised FE methods.

The DG framework, reviewed in detail by Cockburn et al. (2000) or Ern and Di Pietro (2011), allows to devise high-order numerical methods that enforce element-by-element conservation. The method provides a suitable discretisation on unstructured meshes and permits an efficient exploitation of parallel computing architectures, as described by Roca et al. (2013). In addition, an easy implementation of adaptive strategies for non-uniform degree approximations is admitted, as confirmed in several

studies, such as those by Hartmann and Houston (2003), Giorgiani et al. (2014), Balan et al. (2015) or Cangiani et al. (2017). However, the duplication of nodes at the interface of neighbouring elements has limited its application mostly to academic problems, see the discussion by Giacomini and Sevilla (2019) and references therein.

1.1.1.1 Hybridised formulations in high-order methods

Hybridisation of DG schemes has been devised as a significantly less expensive alternative to traditional formulations, as studied by Huerta et al. (2013) or Woopen et al. (2014). For this reason, different hybrid discretisation methods have been proposed in recent years. Among the most promising techniques, one can find the hybrid/hybridised DG method introduced by Egger and Schöberl (2009) and Egger and Waluga (2012a,b), the hybrid high-order (HHO) method presented by Di Pietro et al. (2014), Di Pietro and Ern (2015) or Cockburn et al. (2016), or the hybridisable discontinuous Galerkin (HDG) method, developed in a series of publications by Cockburn and Shu (1998a) or Cockburn and Gopalakrishnan (2004).

The HDG approach proposed by Cockburn et al. (2009) reduces the number of globally coupled degrees of freedom via the introduction of a hybrid variable, namely the trace of the unknown on the mesh faces, and the appropriate definition of the inter-element numerical fluxes. Furthermore, special attention has been devoted to the HDG method which relies on a mixed formulation for second-order problems, as described by Cockburn and Gopalakrishnan (2004, 2005a,b, 2009), Nguyen et al. (2011), Nguyen and Peraire (2012), Qiu and Shi (2016), Sevilla and Huerta (2016) or Giacomini et al. (2020).

In the context of compressible flows, different hybrid methods have been devised for the formulation of the inviscid Euler and the laminar compressible Navier-Stokes equations. The HDG method, first introduced by Peraire et al. (2010) and Nguyen and Peraire (2012), has been well-established and employed in several studies, such as those by Jaust and Schütz (2014), Jaust et al. (2015), Williams (2018), and Komala-Sheshachala et al. (2020). Alternatively, other hybrid discretisations, such as the embedded DG (EDG) scheme presented by Peraire et al. (2011), the interior embedded DG (IEDG) method detailed in Nguyen et al. (2015), or the hybrid mixed formulations introduced by Schütz et al. (2012) and Schütz and May (2013b,a), have been also devised. It is worth noting that in the inviscid limit, i.e. for the Euler equations, HDG methods based on primal and mixed formulations are equivalent. In

addition, the resulting scheme is robust in the incompressible limit, circumventing the Ladyzhenskaya-Babuška-Brezzi (LBB), as described by Cockburn and Gopalakrishnan (2009).

Recently, the HDG method has been also employed for the simulation of turbulent compressible flows. Indeed, the HDG discretisation of the RANS equations combined with the Spalart-Allmaras turbulence model has been presented by Moro et al. (2011, 2017), whereas Woopen et al. (2014) introduced a formulation of the $\kappa - \omega$ model. In addition, in the last years, Fernández et al. (2017) have proposed an HDG formulation for turbulent compressible flows based on an LES approach.

A salient feature of the HDG formulation stemming from Peraire et al. (2010) and Nguyen and Peraire (2012) is its associated optimal order of convergence for the viscous stress and the heat flux. Therefore, the method provides an increased accuracy in the computation of typical quantities of interest in aerodynamic applications, such as lift and drag. Such optimal accuracy properties of the method rely on the equal-order approximation of the primal, mixed and hybrid variables. In this context, when the Cauchy stress tensor formulation is employed for the momentum equation, the appropriate choice of the discretisation space for the mixed variable is crucial to ensure the optimal convergence of the method. To this effect, different strategies have been described in the last years, such as the M-decomposition framework, proposed by Cockburn, Fu, and Qiu (2016), Cockburn, Fu, and Sayas (2016) and Cockburn and Fu (2016a,b, 2017), or the utilisation of the reduced stabilisation, detailed by Oikawa (2015, 2016), Qiu and Shi (2016) or Lehrenfeld and Schberl (2016). Alternatively, Sevilla et al. (2018) and Giacomini et al. (2018, 2020) have recently proposed the employment of a pointwise symmetric formulation of the stress tensor by means of Voigt notation.

The promising potential of high-order methods and, in particular, of the HDG scheme, has been closely related to the high-fidelity simulation of transient phenomena. For this reason, high-order spatial discretisations in HDG have been combined with high-order time integration schemes for the solution of unsteady flow problems, as described by Nguyen and Peraire (2012), Jaust and Schütz (2014), Jaust et al. (2014, 2015) or Fernández et al. (2017). It is worth noting that the HDG method has been inherently combined with implicit time integrators. However, although less explored, the recent works by Samii and Dawson (2018) and Samii et al. (2019) have proposed the combination of the HDG method with explicit time-marching al-

gorithms. Nevertheless, the use of implicit time integrators is well-established for the solution of flows at high Reynolds numbers or near boundary layers generating multiscale phenomena. Similarly, implicit methods are especially suited in the incompressible limit, owing to stability requirements posed by the structure of the problem and the treatment of the incompressibility constraint.

1.1.1.2   Current difficulties and limitations of high-order methods

Despite the great capabilities associated to high-order discretisations, the level of maturity of such methods is still far away from industrial requirements, as concluded by Kroll (2009) within the ADIGMA project. Current implementations of high-order schemes are subject to strong limitations and significant progress is still needed for their application to well-established solvers.

The review works by Wang et al. (2013) or Kroll et al. (2015) point out some of the weaknesses that restrict their applicability as of today. Among others, the inherent complexity of high-order methods has been established as one of the main barriers for ther adoption in standard solvers. In conjunction with their claimed high computational cost for solving transient problems and the corresponding memory footprint, these features impose a challenging demand towards efficient and competitive implementations. Additionally, one of the main bottlenecks in CFD simulation nowadays is the difficulty of generating high-order meshes for complex configurations. In particular, unstructured, highly clustered viscous meshes near curved boundaries set one of the main challenges for current research. In those cases, significant user intervention is required as of today to produce suitable, non-intersecting meshes of the desired resolution.

Finally, the applicability of high-order schemes is also constrained by their lack of robustness, specially to guarantee monotonicity in front of discontinuous solutions in high-speed flows. In particular, whereas most of high-order solvers are able to produce converged solutions at desired levels of accuracy for smooth flowfields, the presence of complicated flow physics or complex geometries may reduce their performance. What is more, in those cases, high-order schemes may eventually fail to converge or lead to instabilities breaking the monotonicity, positivity or entropy preservation of the approximation. Such effects are specially noticeable in presence of flow discontinuities or steep gradients, such as shock waves or boundary layers.

1.1.1.3 Monotonicity: from Riemann solvers to shock-capturing

The appropriate handling of discontinuous solutions represents one of the main challenges for high-order methods. Indeed, based on the work by Godunov and Bohachevsky (1959), the monotonicity of the numerical approximation is only guaranteed for first-order accurate schemes. In those cases, conservation and positivity is ensured by means of the appropriate definition of the interface numerical fluxes arising from the corresponding Riemann problems (Riemann, 1860). To this end, several approximate Riemann solvers have been devised for low-order formulations of compressible flows. This is the case of the numerical fluxes by Lax (1954), Roe (1981) or of HLL type, following the derivation by Harten et al. (1983), as detailed in the monograph by Toro (2009).

In particular, the Lax-Friedrichs Riemann solver, introduced by Lax (1954), defines a robust but overdissipative numerical flux, which arises from the extrapolation of scalar convection studies. On the contrary, the Roe Riemann solver provides increased accuracy, but may fail to produce physically admissible solutions because of a lack of dissipation in transonic and supersonic situations, as described by Quirk (1994) or Perthame and Shu (1996). In those cases, a so-called entropy fix may be needed to recover the entropy conditions and satisfy the positiveness of the density and pressure fields. Finally, HLL-type Riemann solvers, such as HLL or HLLEM, first introduced by Harten et al. (1983), provide a robust framework that inherently preserves the positivity of the approximation. In addition, the HLLEM Riemann solver, derived by Einfeldt (1988) and Einfeldt et al. (1991), introduces a special treatment for shear preservation, likewise Roe, thus improving the Lax-Friedrichs and HLL approximation of contact or shear waves.

Because of the seminal importance of numerical fluxes in the conservation and positivity properties of the solution, the definition of approximate Riemann solvers developed for low-order FV schemes has been extended to high-order. Indeed, different numerical fluxes have been employed in traditional DG methods, as described by Cockburn and Shu (1998c), Qiu et al. (2006) or Moura et al. (2017). In contrast, the definition of approximate Riemann solvers for HDG methods has received considerably less attention, and only the traditional Lax-Friedrichs and Roe solvers have been considered, see Peraire et al. (2010, 2011) or Nguyen and Peraire (2012).

Nevertheless, following the idea by Godunov and contrary to first-order schemes, an appropriate definition of Riemann solvers is not sufficient to guarantee the mono-

tonicity of high-order approximations. Indeed, the representation of a discontinuous solution such as a shock wave by means of a high-order discretisation results in the appearance of spurious oscillations leading to instabilities. For this reason, the correct setting of intercell fluxes must be combined with other numerical strategies to ensure a stable and non-oscillatory behaviour of the approximation. To this end, shock-capturing methods, such as flux limiters, ENO and WENO reconstructions or the introduction of artificial diffusion, have been developed to effectively handle flow discontinuities in high-order methods.

Flux or slope limiters were first introduced within DG methods by Cockburn and Shu (1998b) and Cockburn et al. (1989b) in the so-called RKDG methods. These approaches combined Riemann solvers and nonlinear slope limiters in order to satisfy the Total Variation Bounded on the means (TVBM). Such techniques, formulated for the first time in a series of papers by van Leer (1974, 1977a,b, 1979) and based on total variation diminishing (TVD), rely on keeping the solution between certain limits near discontinuities so as to control the corresponding gradients. Different limiter functions, such as *superbee*, *min-mod* or those introduced by van Leer (1974, 1977a,b, 1979) or Osher and Chakravarthy (1986), have been proposed for numerical discretisations.

Nevertheless, the most popular shock-capturing techniques employed in high-order DG and HDG discretisations are based on artificial dissipation. Such approaches rely on the introduction of a certain amount of non-physical viscosity in those elements affected by the flow discontinuity, which are identified by means of a shock sensor. Different combinations of shock sensors and artificial viscosity functions can be found in the literature. Among the most popular approaches, one can find physics-based sensors that identify regions of high compression or sharp gradients, as proposed by Von Neumann and Richtmyer (1950). For instance, this methodology has been recently employed by Moro et al. (2016) and Fernández et al. (2018) to derive physics-based shock-capturing methods for HDG. Alternatively, a completely different strategy for a shock sensor based on a measure of the regularity of the approximate solution was proposed by Persson and Peraire (2006). This approach has been employed both in the context of DG or, more recently, of HDG methods by Casoni et al. (2012) and Jaust et al. (2014, 2015), respectively.

1.1.2 The current legacy of finite volumes

Because of the yet immature state of high-order discretisations, the vast majority of CFD tools are based nowadays on low-order methods. In particular, second-order FV schemes are the most widely employed strategy in open-source, industrial and commercial CFD solvers. See for instance the CFD codes by the NASA Langley Research Center, CFL3D or FUN3D (documented by Bartels et al. (2006) and Biedron et al. (2019), respectively), or the open source solver OpenFOAM (Jasak, 2009). Other examples of FV CFD solvers in those contexts are the FLITE code, developed in Swansea University by Morgan et al. (1991), the TAU code employed by the German Aerospace Center (Gerhold, 2005), or the CFD solver by Dassault Aviation (Chalot and Perrier, 2004). Based on their efficiency and robustness in solving large-scale problems, FV implementations of the RANS equations have become the high-fidelity baseline for engineering standards.

Different formulations within the FV paradigm have emerged over the years, as reviewed by Morton and Sonar (2007). Among them, the cell-centred finite volume (CCFV) method and the vertex-centred finite volume (VCFV) method represent its two main families. In such classification, the two categories are determined by the position of the degrees of freedom of the problem. Indeed, the CCFV scheme, described by Eymard et al. (2000) or Randall J. Leveque (2013) and employed in several studies, such as by Maire et al. (2007), is characterised by defining the unknowns of the problem at the centroid of the mesh cells or elements. Accordingly, their values correspond to the cell averages of the problem solution. Conversely, the VCFV method, used for instance in the works by Sørensen et al. (2003) or Asouti et al. (2010), sets its unknowns at the mesh nodes. This strategy defines the control volumes for each of these nodes by joining the centroids of the neighbouring mesh elements and the midpoints of the corresponding faces. As a result, a dual mesh conformed by this set of nonoverlapping subdomains surrounding each of the nodes of the discretisation is constructed and used for building the numerical approximation. Similarly to the CCFV approach, the computed quantities represent the averages on the control volume. A shared feature in both of the two strategies consists of the gradient reconstruction that is employed to compute the corresponding approximations at the faces of the control volume. In correspondence, first-order accuracy of such reconstruction is required in order to provide second-order accuracy to the corresponding FV method.

In this line, recent needs within computational engineering have established the use of more complex geometries and larger meshes, revealing at the same time one of the major limitations of current FV formulations. Indeed, the first-order accuracy of the gradient reconstruction of both CCFV and VCFV schemes is a key aspect for the overall accuracy of the method. However, as pointed out in different studies, such as those by Svärd et al. (2008), Diskin et al. (2010) or Diskin and Thomas (2011), the accuracy of such reconstructions is in turn limited by the mesh quality. In particular, the use of irregular or highly stretched grids may result in a loss of the second-order convergence of the solution and the first-order accuracy of the viscous stresses and heat flux. In those cases, the quality of typical quantities of interest in engineering applications, such as lift and drag, is strongly compromised.

Recently, the face-centred finite volume (FCFV) paradigm has been proposed by Sevilla et al. (2018, 2019), Giacomini and Sevilla (2020) and Vieira et al. (2020) for a series of linear elliptic partial differential equations (PDEs). The FCFV method utilises a mixed FV formulation and eliminates the degrees of freedom within each cell via a hybridisation step, leading to a problem defined in terms of the unknwons at the face barycentres only. Finally, the variables inside each cell are retrieved via a computationally inexpensive postprocessing step performed independently cell-by-cell.

The FCFV method has shown its versatility in devising approximations based on meshes of different cell types and on hybrid meshes, as described by Sevilla et al. (2018) and Giacomini and Sevilla (2020), proving to be a robust methodology insensitive to element type and mesh quality. Although the FCFV method is known to introduce a larger number of unknowns than CCFV and VCFV approaches, the simplified procedure required to generate meshes suitable for computation and its capability to avoid gradient reconstruction make the FCFV scheme a competitive alternative to traditional FV solvers from the computational viewpoint.

It is worth mentioning that FV methods have been reinterpreted in recent years as particular cases of finite element discretisations, as detailed by Morton and Sonar (2007). Under this perspective, Eymard et al. (2000) and Cockburn et al. (2000) described the CCFV method as a discontinuous Galerkin (DG) method with piecewise constant degree of approximation in each cell. Similarly, Bank and Rose (1987) and Selmin (1993) redefined the VCFV scheme on simplicial meshes as a conforming piecewise linear continuous finite element method. Concerning the FCFV paradigm,

it can be interpreted as the lowest-order version of the hybridisable discontinuous Galerkin (HDG) method, in which constant approximations are selected for all the variables. The resulting FCFV method thus inherits its properties from HDG, including the optimal convergence of primal and mixed variables without need of reconstruction and its stability in the incompressible limit, circumventing the Ladyzhenskaya-Babuška-Brezzi (LBB) condition. Hence, the FCFV method provides accurate approximations of incompressible flows without the need of introducing specific pressure corrections like the well-known SIMPLE algorithm, described by Patankar and Spalding (1972), implemented by commercial and open-source software, see e.g. ANSYS Inc. (2017) or Jasak (2009).

1.2 Objectives and outline

The main goal of this thesis focuses on the high-fidelity simulation of compressible flows by means of hybridisable discontinuous Galerkin methods. In particular, this work is aimed at developing a robust and efficient framework, allowing to address large-scale problems while tackling the inherent complex phenomena associated to compressible flow physics.

Nonetheless, the frame of this work is build within the two paradigms that configure the simulation of compressible flows as of today: the traditional low-order finite volume schemes and the emerging high-order methods. Because of this dual vision within CFD, this work pursues a twofold strategy aimed at contributing at both levels.

For this purpose, the following partial goals are considered:

1. **The formulation of a face-centred finite volume method for the simulation of steady-state compressible flows.**

   Second-order FV methods are well-established within the CFD community for the solution of steady-state flows. Their high level of maturity has provided them with robust and efficient strategies for tackling large-scale problems in short computation times. However, these numerical schemes are limited by the loss of precision that experience in irregular or highly stretched meshes, due to an inaccurate reconstruction of the gradients of the flowfield variables.

For this reason, the face-centred finite volume (FCFV) method, arising from the constant order of approximation of HDG, is proposed for the solution of steady-state compressible flows. The resulting scheme defines the unknowns of the problem on the mesh faces and inherits the convergence properties of HDG. Therefore, it ensures optimal first-order convergence of the conservation quantities, viscous stresses and heat flux without need for reconstruction, hence, regardless of a high stretching or distortion of the mesh. In addition, based on its first-order accuracy, the FCFV scheme is inherently monotonic, which results in no need for shock capturing techniques in the approximation of sharp gradients or discontinuities. Finally, the method displays a robust behaviour in the incompressible limit.

The FCFV formulation of compressible flows is presented in chapter 2 for the solution of steady-state problems. Different test cases of inviscid and viscous flows are displayed so as to examine the accuracy properties of the numerical scheme, together with its robustness in front of high stretching or distortion of the mesh or in the incompressible limit. Finally, a set of numerical benchmarks consisting of transonic 2D and 3D external flows over aerofoils and wings is introduced to demonstrate the capabilities and potential of the proposed methodology and its applicability to large-scale realistic examples.

Additionally, the FCFV method is also extended to the formulation of the RANS equations, equipped with a Spalart-Allmaras turbulence model, in appendix C. By means of an analytical example with manufactured solution, the accuracy properties of the FCFV scheme are evaluated.

2. **The formulation of positivity preserving HLL-type numerical fluxes for compressible flows in hybridisable discontinuous Galerkin methods, developed within a unified framework for the derivation of Riemann solvers.**

The future perspectives of CFD rely on the development of high-order strategies, necessary for the resolution of transient complex flow phenomena arising in conventional aircraft aerodynamics. However, high-order methods are still challenged by the configuration of a robust framework allowing them to manage overnight computations of compressible flows in an effective way. In other words, of being able to produce physically admissible solutions to complex flow

problems within reasonable time and minimal user intervention.

The high-order hybridisable discontinuous Galerkin (HDG) method, which provides optimal accuracy not only for the conservation variables but also for viscous stresses and heat flux, is considered for the high-fidelity simulation of compressible flows. In this context, the study of Riemann solvers has been limited to the use of Lax-Friedrichs and Roe numerical fluxes, contrary to FV or traditional DG schemes, for which multiple alternatives have been devised, as briefly summarised in appendix B. For this reason, this thesis proposes a thorough exploration into the derivation of Riemann solvers in HDG, based on extending existing DG formulations of approximate numerical fluxes.

Therefore, the HDG formulation of compressible flows, equipped with a shock treatment strategy based on artificial viscosity, is described in chapter 3 together with a unified framework for the derivation of Riemann solvers in hybridised methods. This framework allows the formulation, for the first time in an HDG context, of the HLL and HLLEM Riemann solvers as well as the traditional Lax-Friedrichs and Roe solvers.

Then, a comprehensive set of relevant numerical benchmarks of viscous and inviscid compressible flows is presented in chapter 4 to evaluate the robustness and competitiveness of the resulting high-order HDG scheme. In particular, the positivity properties of HLL-type numerical fluxes are thoroughly examined in transonic and supersonic cases, for which the Roe solver may fail to satisfy entropy conditions. In addition, the shear preservation of HLLEM solver is also tested in a series of examples, proving its outstanding performance in the approximation of boundary layers, providing an increased accuracy with respect to HLL and Lax-Friedrichs.

Chapter 2

A face-centred finite volume method for compressible flows [1]

Finite volume (FV) solvers are the most widespread technology within the aerospace community for the simulation of steady-state compressible flows. Their success relies on their capability of providing results for complex large-scale flow problems by means of overnight simulations. Nonetheless, usual FV strategies require delicate mesh generation procedures with limited unstructured regions and distorted cells in order to construct high-quality meshes suitable for computation. In this line, a new mixed hybrid FV paradigm, the face-centred finite volume (FCFV) scheme, has been recently proposed, providing optimal first-order accuracy for the problem variables and their gradients without need of reconstruction strategies. The resulting method is therefore insensitive to mesh quality and offers a competitive alternative to traditional FV solvers from the computational viewpoint.

This chapter introduces the FCFV formulation of steady-state compressible flows, spanning from viscous compressible Navier-Stokes to inviscid Euler equations, which is also robust in the incompressible limit. The resulting method retrieves first-order convergence for the the flow variables, i.e. density, momentum and energy, stress tensor and the heat flux without need of gradient reconstruction strategies. In addition, the FCFV method defines a monotonicity-preserving framework, providing

---

[1]This chapter is a modified version of the in-preparation article: J. Vila-Pérez, M. Giacomini, R. Sevilla, A. Huerta, A non-oscillatory face-centred finite volume method for compressible flows.

15

non-oscillatory approximations of shock waves and sharp fronts without the need of shock capturing techniques.

The organisation of this chapter is detailed as follows. In section 2.1, the compressible Navier-Stokes equations are recalled. Section 2.2 introduces the corresponding FCFV discretisation and the integration of Riemann solvers in the definitions of the numerical fluxes. A set of convergence tests to validate the optimal accuracy properties of the method for inviscid and viscous laminar flows is presented in section 2.3, with special emphasis on the robustness to cell stretching and distortion. Two and three-dimensional benchmarks of external flows of aerodynamic interest are reported in section 2.4 to demonstrate the capabilities of the method in different flow regimes, from inviscid to viscous laminar flows, from transonic to subsonic incompressible flows. Finally, section 2.5 reviews the main results of this work.

Technical details on the symmetry enforcement of the deviatoric strain rate tensor, employed as mixed variable of the problem, are provided in appendix A. In addition, the extension of the FCFV method for the formulation of the RANS equations coupled with the Spalart-Allmaras turbulence model is presented in appendix C.

2.1   Governing equations

Let $\Omega \subset \mathbb{R}^{\mathtt{n_{sd}}}$ be an open bounded domain with boundary $\partial\Omega$, being $\mathtt{n_{sd}}$ the number of spatial dimensions, and $\mathtt{T_{end}} > 0$ the final time of interest. The Navier-Stokes equations, governing unsteady viscous compressible flows in absence of external body forces are expressed in nondimensional conservation form as

$$\frac{\partial \boldsymbol{U}}{\partial t} + \boldsymbol{\nabla} \cdot (\boldsymbol{F}(\boldsymbol{U}) - \boldsymbol{G}(\boldsymbol{U}, \boldsymbol{\nabla U})) = \boldsymbol{0}, \quad \text{in } \Omega \times (0, \mathtt{T_{end}}], \tag{2.1}$$

where $\boldsymbol{U} \in \mathbb{R}^{\mathtt{n_{sd}}+2}$ is the vector of dimensionless conservative variables and $\boldsymbol{F}$ and $\boldsymbol{G} \in \mathbb{R}^{(\mathtt{n_{sd}}+2)\times\mathtt{n_{sd}}}$ are the advection and diffusion flux tensors, respectively, given by

$$\boldsymbol{U} = \left\{\begin{matrix} \rho \\ \rho\boldsymbol{v} \\ \rho E \end{matrix}\right\}, \quad \boldsymbol{F}(\boldsymbol{U}) = \begin{bmatrix} \rho\boldsymbol{v}^T \\ \rho\boldsymbol{v} \otimes \boldsymbol{v} + p\mathbf{I}_{\mathtt{n_{sd}}} \\ (\rho E + p)\boldsymbol{v}^T \end{bmatrix}, \quad \boldsymbol{G}(\boldsymbol{U}, \boldsymbol{\nabla U}) = \begin{bmatrix} \boldsymbol{0} \\ \boldsymbol{\sigma}^d \\ (\boldsymbol{\sigma}^d \boldsymbol{v} + \boldsymbol{q})^T \end{bmatrix}. \tag{2.2}$$

In these expressions, ρ denotes the density, $\boldsymbol{v}$ is the velocity vector, E is the total specific energy, p is the pressure, $\boldsymbol{\sigma}^d$ is the viscous stress tensor and $\boldsymbol{q}$ is the heat flux.

Remark 2.1 (Non-dimensional variables). The dimensionless physical variables are obtained using the following reference free-stream quantities, indicated by the subscript ∞, namely

$$
\begin{aligned}
&\tilde{\rho} = \frac{\rho}{\rho_\infty}, &&\tilde{\boldsymbol{v}} = \frac{\boldsymbol{v}}{v_\infty}, &&\tilde{E} = \frac{E}{v_\infty^2}, &&\tilde{p} = \frac{p}{\rho_\infty v_\infty^2}, \\
&\tilde{\boldsymbol{x}} = \frac{\boldsymbol{x}}{L}, &&\tilde{t} = \frac{t}{L/v_\infty}, &&\tilde{\mu} = \frac{\mu}{\mu_\infty}, &&\tilde{T} = \frac{T}{v_\infty^2/c_p},
\end{aligned}
\tag{2.3}
$$

where T is the temperature, $\boldsymbol{x}$ and t denote spatial position and time, and L is a characteristic length. For the sake of simplicity, tildes for the nondimensional variables are dropped in this work.

The flow is assumed to obey the ideal gas law $\gamma p = (\gamma - 1)\rho T$, where $\gamma = c_p/c_v$ is the ratio of specific heats at constant pressure, c_p, and constant volume, c_v, and takes value $\gamma = 1.4$ for air. Moreover, for a calorically perfect gas, it holds that $p = (\gamma - 1)\rho\left(E - \|\boldsymbol{v}\|^2/2\right)$.

Under Stokes' hypothesis, the viscous stress tensor is expressed as

$$
\boldsymbol{\sigma}^d = \frac{\mu}{Re}\left(2\boldsymbol{\nabla}^{\mathtt{S}}\boldsymbol{v} - \frac{2}{3}(\boldsymbol{\nabla}\cdot\boldsymbol{v})\mathbf{I}_{\mathtt{n_{sd}}}\right),
\tag{2.4}
$$

where $\boldsymbol{\nabla}^{\mathtt{S}} := (\boldsymbol{\nabla} + \boldsymbol{\nabla}^T)/2$ is the symmetric part of the gradient operator.

Remark 2.2 (Cauchy stress tensor). The Cauchy stress tensor, $\boldsymbol{\sigma}$, which assembles the mechanical stresses of the fluid, is the combination of the viscous stress tensor $\boldsymbol{\sigma}^d$ and the thermodynamical pressure p, that is $\boldsymbol{\sigma} = \boldsymbol{\sigma}^d - p\mathbf{I}_{\mathtt{n_{sd}}}$.

In addition, the heat flux is modelled according to Fourier's law of heat conduction, that is

$$
\boldsymbol{q} = \frac{\mu}{PrRe}\boldsymbol{\nabla}T,
\tag{2.5}
$$

and the nondimensional dynamic viscosity, μ, depends on the temperature following Sutherland's law, i.e.

$$
\mu = \left(\frac{T}{T_\infty}\right)^{3/2}\frac{T_\infty + S}{T + S},
\tag{2.6}
$$

where the dimensionless free-stream temperature and the Sutherland constant are expressed, respectively, as $T_\infty = 1/\left((\gamma - 1)M_\infty^2\right)$ and $S = S_0/\left((\gamma - 1)T_{\mathtt{ref}}M_\infty^2\right)$, with $S_0 = 110K$ for a reference temperature of $T_{\mathtt{ref}} = 273K$.

The nondimensional description of the problem is completed with the definition of the Reynolds, Prandtl and Mach numbers, defined respectively as

$$M_\infty = \frac{v_\infty}{c_\infty}, \qquad Re = \frac{\rho_\infty v_\infty L}{\mu_\infty}, \qquad Pr = \frac{c_p \mu_\infty}{\kappa}, \tag{2.7}$$

being $c = \sqrt{\gamma p / \rho}$ the speed of sound and κ the thermal conductivity. The Prandtl number is considered constant and equal to $Pr = 0.71$ for air.

The problem is closed with the prescription of initial and boundary conditions, namely

$$\begin{aligned} \boldsymbol{U} = \boldsymbol{U}^0 \quad &\text{in } \Omega \times \{0\}, \\ \boldsymbol{B}(\boldsymbol{U}, \boldsymbol{\nabla U}) = \boldsymbol{0} \quad &\text{on } \partial\Omega \times (0, \mathrm{T_{end}}], \end{aligned} \tag{2.8}$$

where $\boldsymbol{U}^0$ stands for an initial state and the vector $\boldsymbol{B}$ describes a boundary condition operator, imposing inflow, outflow or wall conditions with isothermal, adiabatic or symmetry properties as detailed in section 2.2.3.

Remark 2.3 (Compressible Euler equations). The compressible Euler equations are recovered in the inviscid limit, that is when $Re \to \infty$. In such case, the set of conservation equations (2.1) becomes a system of first-order hyperbolic PDEs, namely

$$\frac{\partial \boldsymbol{U}}{\partial t} + \boldsymbol{\nabla} \cdot \boldsymbol{F}(\boldsymbol{U}) = \boldsymbol{0}, \quad \text{in } \Omega \times (0, \mathrm{T_{end}}]. \tag{2.9}$$

2.2   FCFV formulation for compressible flows

The FCFV formulation of compressible flows is detailed as follows. To this effect, consider a partition of the domain Ω in $\mathtt{n_{el}}$ disjoint subdomains Ω_e satisfying $\Omega = \bigcup_{e=1}^{\mathtt{n_{el}}} \Omega_e$. Additionally, let $\partial\Omega_e$ denote the boundary of cell Ω_e, obtained as the union of its faces Γ_{ej}, namely

$$\partial\Omega_e := \bigcup_{j=1}^{\mathtt{n_{fa}^e}} \Gamma_{ej}, \tag{2.10}$$

where $\mathtt{n_{fa}^e}$ is the total number of faces of the cell Ω_e. Finally, let Γ denote the *mesh skeleton* or internal interface, defined as

$$\Gamma := \left[\bigcup_{e=1}^{\mathtt{n_{el}}} \partial\Omega_e \right] \setminus \partial\Omega. \tag{2.11}$$

Furthermore, the notation for the *jump* operator, $[\![\odot]\!] = \odot^+ + \odot^-$, is employed, defining the sum of the values in the elements Ω^+ and Ω^- at each side of the internal face Γ_f, respectively.

2.2.1 Introducing a set of mixed variables

Following the HDG and FCFV rationales described by Cockburn et al. (2009), Cockburn and Gopalakrishnan (2009) or Nguyen and Peraire (2012) and Sevilla et al. (2018, 2019), respectively, the second-order problem (2.1) is written as a system of first-order PDEs via the introduction of a set of so-called *mixed variables*. In the context of compressible flows, a detailed review of commonly employed mixed variables is discussed in section 3.1. As indicated, the most common approach relies on defining the mixed variable as the gradient of the so-called *primal variable* $\boldsymbol{U}$, namely $\mathbf{Q} = \boldsymbol{\nabla} \boldsymbol{U}$, such as in Peraire et al. (2010), Nguyen and Peraire (2012), Woopen et al. (2014) or Fernández et al. (2017). Nonetheless, this choice leads to the introduction of a mixed variable, associated with the gradient of density, which is redundant since the mass conservation equation is a first-order PDE. In addition, several nonlinearities appear in the resulting expressions to compute the viscous stress and the heat flux starting from $\boldsymbol{U}$ and $\mathbf{Q}$. Alternatively, the proposed FCFV scheme follows the HDG formulation described in chapter 3 and only two mixed variables, i.e. the deviatoric strain rate tensor and the gradient of temperature, are considered, namely

$$\boldsymbol{\varepsilon}^d = 2\boldsymbol{\nabla}^{\mathrm{S}}\boldsymbol{v} - \frac{2}{3}(\boldsymbol{\nabla} \cdot \boldsymbol{v})\mathbf{I}_{\mathrm{n_{sd}}}, \qquad \boldsymbol{\phi} = \boldsymbol{\nabla} T. \tag{2.12}$$

Remark 2.4 (Deviatoric strain rate). It is worth noticing that the deviatoric strain rate tensor can be expressed as a function of the gradient of velocity as $\boldsymbol{\varepsilon}^d = \mathcal{D}\boldsymbol{\nabla}^{\mathrm{S}}\boldsymbol{v}$, where the linear operator $\mathcal{D}$ is defined as

$$\mathcal{D}\boldsymbol{W} = \left(\boldsymbol{W} + \boldsymbol{W}^T\right) - \frac{2}{3}\mathrm{tr}(\boldsymbol{W})\mathbf{I}. \tag{2.13}$$

Interested readers are referred to appendix A for the details concerning the construction of the operator $\mathcal{D}$ and its implementation.

Besides reducing the number of mixed variables involved, from (2.12) it also follows that the viscous stress tensor and the heat flux vector in equations (2.4) and .2.5 can be obtained using the linear expressions

$$\boldsymbol{\sigma}^d = \frac{\mu}{Re}\boldsymbol{\varepsilon}^d, \qquad \boldsymbol{q} = \frac{\mu}{RePr}\boldsymbol{\phi}. \tag{2.14}$$

2.2.2 A mixed hybrid finite volume framework

The FCFV method solves the compressible Navier-Stokes equations in two stages. First, an independent hybrid variable $\widehat{\boldsymbol{U}}$, representing the vector of conservative vari-

ables on the mesh faces $\Gamma \cup \partial\Omega$, is introduced. Equation (2.1) is thus rewritten in each cell Ω_e, $e = 1, \ldots, \mathtt{n_{el}}$ as

$$\begin{cases} \boldsymbol{\varepsilon}^d - \mathcal{D}\boldsymbol{\nabla}^{\mathrm{S}}\boldsymbol{v} = \boldsymbol{0} & \text{in } \Omega_e \times (0, \mathrm{T_{end}}], \\ \boldsymbol{\phi} - \boldsymbol{\nabla}T = \boldsymbol{0} & \text{in } \Omega_e \times (0, \mathrm{T_{end}}], \\ \dfrac{\partial \boldsymbol{U}}{\partial t} + \boldsymbol{\nabla} \cdot \big(\boldsymbol{F}(\boldsymbol{U}) - \boldsymbol{G}(\boldsymbol{U}, \boldsymbol{\varepsilon}^d, \boldsymbol{\phi})\big) = \boldsymbol{0} & \text{in } \Omega_e \times (0, \mathrm{T_{end}}], \\ \boldsymbol{U} = \boldsymbol{U}^0 & \text{in } \Omega_e \times \{0\}, \\ \boldsymbol{U} = \widehat{\boldsymbol{U}} & \text{on } \partial\Omega_e \times (0, \mathrm{T_{end}}]. \end{cases} \qquad (2.15)$$

Equation (2.15) represents the $\mathtt{n_{el}}$ FCFV local problems. They define the vector of conservative variables and the mixed variables $(\boldsymbol{U}, \boldsymbol{\varepsilon}^d, \boldsymbol{\phi})$ in each cell as functions of the hybrid vector $\widehat{\boldsymbol{U}}$ on the cell faces, in order to reduce the global number of unknowns of the problem.

Second, the vector $\widehat{\boldsymbol{U}}$ of conservative variables on the faces is computed by solving the FCFV global problem, which prescribes the continuity of the conservative variables and of the normal fluxes on Γ and the boundary conditions on $\partial\Omega$, namely

$$\begin{cases} [\![\boldsymbol{U} \otimes \boldsymbol{n}]\!] = \boldsymbol{0} & \text{on } \Gamma \times (0, \mathrm{T_{end}}], \\ [\![\big(\boldsymbol{F}(\boldsymbol{U}) - \boldsymbol{G}(\boldsymbol{U}, \boldsymbol{\varepsilon}^d, \boldsymbol{\phi})\big)\boldsymbol{n}]\!] = \boldsymbol{0} & \text{on } \Gamma \times (0, \mathrm{T_{end}}], \\ \widehat{\boldsymbol{B}}(\boldsymbol{U}, \widehat{\boldsymbol{U}}, \boldsymbol{\varepsilon}^d, \boldsymbol{\phi}) = \boldsymbol{0}, & \text{on } \partial\Omega \times (0, \mathrm{T_{end}}], \end{cases} \qquad (2.16)$$

where $\boldsymbol{n}$ stands for the outward normal vector to the cell face and $[\![\odot]\!] = \odot^+ + \odot^-$ denotes the *jump* operator defined on an internal face as the sum of the values in the neighbouring elements Ω^+ and Ω^-, respectively, as detailed by Montlaur et al. (2008). The trace boundary operator $\widehat{\boldsymbol{B}}(\boldsymbol{U}, \widehat{\boldsymbol{U}}, \boldsymbol{\varepsilon}^d, \boldsymbol{\phi})$ imposes the boundary conditions on $\partial\Omega$ exploiting the hybrid variable, as detailed in section 2.2.3.

It is worth noticing that the first condition in equation (2.16) is automatically satisfied due to the Dirichlet boundary conditions imposed in the local problems (2.15) and because of the unique definition of the hybrid variable $\widehat{\boldsymbol{U}}$ on each face.

2.2.3   Boundary conditions in hybridised formulations

The global problem (2.27) imposes boundary conditions via $\widehat{\boldsymbol{B}} = \widehat{\boldsymbol{B}}(\boldsymbol{U}, \widehat{\boldsymbol{U}}, \boldsymbol{\varepsilon}^d, \boldsymbol{\phi})$, the traces of the corresponding boundary condition operator on the external interface.

Following the philosophy of the works by Peraire et al. (2010),Nguyen and Peraire (2012), Fernández et al. (2017) and Mengaldo et al. (2014), different definitions of

boundary conditions that commonly arise in simulations of compressible flow problems are presented in table 2.1.

Let the boundary $\partial\Omega$ be partitioned as $\partial\Omega = \Gamma_\infty \cup \Gamma_{\text{out}} \cup \Gamma_{\text{ad}} \cup \Gamma_{\text{iso}} \cup \Gamma_{\text{inv}}$, where the introduced portions are disjoint by pairs. From the modelling viewpoint, Γ_∞ refers to a far-field boundary, Γ_{out} is a subsonic outlet with imposed pressure, Γ_{ad} and Γ_{iso} denote adiabatic and isothermal walls, respectively, whereas Γ_{inv} represents a symmetry boundary or an inviscid wall with slip conditions.

Table 2.1: Definition of boundary conditions for compressible flow problems using a hybrid discretisation.

Γ_∞	Far-field, subsonic inlet, supersonic inlet/outlet $\widehat{\boldsymbol{B}} = \boldsymbol{A}_n^+(\widehat{\boldsymbol{U}})(\boldsymbol{U} - \widehat{\boldsymbol{U}}) + \boldsymbol{A}_n^-(\widehat{\boldsymbol{U}})(\boldsymbol{U}_\infty - \widehat{\boldsymbol{U}})$
Γ_{out}	Subsonic outlet (pressure outlet) $\widehat{\boldsymbol{B}} = \left\{ \rho - \widehat{\rho},\, [\rho\boldsymbol{v} - \widehat{\rho\boldsymbol{v}}]^T,\, \dfrac{p_{\text{out}}}{\gamma - 1} + \dfrac{\rho\|\boldsymbol{v}\|^2}{2} - \widehat{\rho E} \right\}^T$
Γ_{ad}	Adiabatic wall $\widehat{\boldsymbol{B}} = \left\{ \rho - \widehat{\rho},\, \widehat{\rho\boldsymbol{v}}^T,\, \dfrac{\mu}{RePr}\boldsymbol{\phi}\boldsymbol{n} - \tau_{\rho E}^d(\rho E - \widehat{\rho E}) \right\}^T$
Γ_{iso}	Isothermal wall $\widehat{\boldsymbol{B}} = \left\{ \rho - \widehat{\rho},\, \widehat{\rho\boldsymbol{v}}^T,\, \dfrac{\rho T_{\text{w}}}{\gamma} - \widehat{\rho E} \right\}^T$
Γ_{inv}	Symmetry surface or inviscid wall $\widehat{\boldsymbol{B}} = \{ \rho - \widehat{\rho},\, [(\mathbf{I}_{\text{n}_{\text{sd}}} - \boldsymbol{n} \otimes \boldsymbol{n})\rho\boldsymbol{v} - \widehat{\rho\boldsymbol{v}}]^T,\, \rho E - \widehat{\rho E}\}^T$

In the expressions listed in table 2.1, $\boldsymbol{U}_\infty$, p_{out} and T_w denote free-stream values of the conserved variables at the far-field and prescribed values of outflow pressure and wall temperature, respectively. Additionally, $\tau_{\rho E}^d = 1/\left[(\gamma - 1)M_\infty^2 RePr\right]$ is a diffusive stabilisation term for the heat flux.

Furthermore, note that inlet and outlet boundaries on Γ_∞ are identified through a 1D characteristics analysis in the direction of the outward normal to the boundary. More precisely, $\boldsymbol{A}_n^\pm := (\boldsymbol{A}_n \pm |\boldsymbol{A}_n|)/2$ denote the positive and negative parts of the matrix $\boldsymbol{A}_n(\widehat{\boldsymbol{U}})$ and they are defined exploiting the spectral decomposition of the Jacobian matrix of the convective flux in the normal direction to the boundary, namely $\boldsymbol{A}_n(\widehat{\boldsymbol{U}}) := [\partial\boldsymbol{F}(\widehat{\boldsymbol{U}})/\partial\widehat{\boldsymbol{U}}] \cdot \boldsymbol{n} = \boldsymbol{R}\boldsymbol{\Lambda}\boldsymbol{L}$. Additionally, $|\boldsymbol{A}_n(\widehat{\boldsymbol{U}})| := \boldsymbol{R}|\boldsymbol{\Lambda}|\boldsymbol{L}$ and the matrix $|\boldsymbol{\Lambda}|$ is a diagonal matrix containing the absolute value of the eigenvalues in $\boldsymbol{\Lambda}$.

The expression of the matrices of eigenvectors and eigenvalues, $\boldsymbol{R}$, $\boldsymbol{L}$ and $\boldsymbol{\Lambda}$, can be found in the work by Rohde (2001).

2.2.4 Integral form of the FCFV local and global problems

For each cell Ω_e, $e = 1, \ldots, \texttt{n}_{\texttt{el}}$, the integral form of the FCFV local problem is obtained by applying the divergence theorem to equation (2.15). Given $\boldsymbol{U} = \boldsymbol{U}^0$ at time $t = 0$, it holds that

$$\int_{\Omega_e} \boldsymbol{\varepsilon}^d \, d\Omega - \int_{\partial\Omega_e} \mathcal{D}\widehat{\boldsymbol{v}} \otimes \boldsymbol{n} \, d\Gamma = \boldsymbol{0}, \tag{2.17a}$$

$$\int_{\Omega_e} \boldsymbol{\phi} \, d\Omega - \int_{\partial\Omega_e} \widehat{T}\boldsymbol{n} \, d\Gamma = \boldsymbol{0}, \tag{2.17b}$$

$$\int_{\Omega_e} \frac{\partial \boldsymbol{U}}{\partial t} \, d\Omega + \int_{\partial\Omega_e} \left(\widehat{\boldsymbol{F}(\boldsymbol{U})\boldsymbol{n}} - \widehat{\boldsymbol{G}(\boldsymbol{U}, \boldsymbol{\varepsilon}^d, \boldsymbol{\phi})\boldsymbol{n}} \right) d\Gamma = \boldsymbol{0}, \tag{2.17c}$$

where $\widehat{\boldsymbol{v}}$ and $\widehat{T}$ denote the velocity and temperature fields on the cell faces $\partial\Omega_e$, respectively, and they are defined using the hybrid vector $\widehat{\boldsymbol{U}}$ of conservative variables. This problem corresponds to the hybridisation step of the FCFV method: the goal is to eliminate the unknowns $(\boldsymbol{U}, \boldsymbol{\varepsilon}^d, \boldsymbol{\phi})$ within each cell by expressing them in terms of the hybrid variable $\widehat{\boldsymbol{U}}$.

The unknown $\widehat{\boldsymbol{U}}$ is thus computed by means of the global problem (2.16) whose integral form is

$$\sum_{e=1}^{\texttt{n}_{\texttt{el}}} \left\{ \int_{\partial\Omega_e \setminus \partial\Omega} \left(\widehat{\boldsymbol{F}(\boldsymbol{U})\boldsymbol{n}} - \widehat{\boldsymbol{G}(\boldsymbol{U}, \boldsymbol{\varepsilon}^d, \boldsymbol{\phi})\boldsymbol{n}} \right) d\Gamma + \int_{\partial\Omega_e \cap \partial\Omega} \widehat{\boldsymbol{B}}(\boldsymbol{U}, \widehat{\boldsymbol{U}}, \boldsymbol{\varepsilon}^d, \boldsymbol{\phi}) \, d\Gamma \right\} = \boldsymbol{0}. \tag{2.18}$$

The terms $\widehat{\boldsymbol{F}(\boldsymbol{U})\boldsymbol{n}}$ and $\widehat{\boldsymbol{G}(\boldsymbol{U}, \boldsymbol{\varepsilon}^d, \boldsymbol{\phi})\boldsymbol{n}}$ appearing in equations (2.17c) and (2.18) stand for the convection and diffusion numerical fluxes of the conservation equations, respectively. It is worth recalling that the approximation of the numerical fluxes in the FCFV method plays a crucial role in the accuracy and stability of the computed solution, see Sevilla et al. (2018, 2019), Vieira et al. (2020) or Giacomini and Sevilla (2020). Therefore, following the rationale introduced by Peraire et al. (2010, 2011), Nguyen and Peraire (2012) or Fernández et al. (2017) for high-order HDG discretisations, the traces of the numerical fluxes on the cell faces are defined as

$$\widehat{\boldsymbol{F}(\boldsymbol{U})\boldsymbol{n}} = \boldsymbol{F}(\widehat{\boldsymbol{U}})\boldsymbol{n} + \boldsymbol{\tau}^a(\widehat{\boldsymbol{U}}) \, (\boldsymbol{U} - \widehat{\boldsymbol{U}}), \tag{2.19a}$$

$$\widehat{\boldsymbol{G}(\boldsymbol{U}, \boldsymbol{\varepsilon}^d, \boldsymbol{\phi})\boldsymbol{n}} = \boldsymbol{G}(\widehat{\boldsymbol{U}}, \boldsymbol{\varepsilon}^d, \boldsymbol{\phi})\boldsymbol{n} - \boldsymbol{\tau}^d \, (\boldsymbol{U} - \widehat{\boldsymbol{U}}). \tag{2.19b}$$

On the one hand, the stabilisation tensor $\boldsymbol{\tau}^a$ is associated with convection phenomena. Different expressions of $\boldsymbol{\tau}^a$ are derived from the theory of Riemann solvers for nonlinear hyperbolic PDEs, as described in section 2.2.5. On the other hand, the term $\boldsymbol{\tau}^d$ stands for the stabilisation tensor related to viscous effects and is defined by means of the diagonal matrix

$$\boldsymbol{\tau}^d = \frac{1}{Re} \operatorname{diag}\left(0, \mathbf{1}_{\mathtt{n_{sd}}}, \frac{1}{(\gamma - 1)M_\infty^2 Pr}\right), \tag{2.20}$$

being $\mathbf{1}_{\mathtt{n_{sd}}}$ an $\mathtt{n_{sd}}$-dimensional vector of ones.

Remark 2.5 (FCFV method for inviscid Euler equations)**.** The inviscid Euler equations are obtained as the limit of the compressible Navier-Stokes equations when $Re \to \infty$. Setting $\boldsymbol{G} = \boldsymbol{0}$, equation (2.1) thus reduces to the well-known system of first-order hyperbolic PDEs modelling inviscid compressible flows. For each cell Ω_e, $e = 1, \ldots, \mathtt{n_{el}}$, the corresponding FCFV local problem for the Euler equations is obtained from equation (2.17) by neglecting the mixed variables and the viscous term, namely

$$\int_{\Omega_e} \frac{\partial \boldsymbol{U}}{\partial t} \, d\Omega + \int_{\partial\Omega_e} \widehat{\boldsymbol{F}(\boldsymbol{U})\boldsymbol{n}} \, d\Gamma = \boldsymbol{0}. \tag{2.21}$$

Similarly, the global problem follows from the simplification of equation (2.18) as

$$\sum_{e=1}^{\mathtt{n_{el}}} \left\{ \int_{\partial\Omega_e \backslash \partial\Omega} \widehat{\boldsymbol{F}(\boldsymbol{U})\boldsymbol{n}} \, d\Gamma + \int_{\partial\Omega_e \cap \partial\Omega} \widehat{\boldsymbol{B}}(\boldsymbol{U}, \widehat{\boldsymbol{U}}) \, d\Gamma \right\} = \boldsymbol{0}. \tag{2.22}$$

2.2.5 Riemann solvers for the FCFV method

In the context of the FCFV method, Riemann solvers are defined implicitly within the convection fluxes, see equation (2.19a), via appropriate expressions of the stabilisation term $\boldsymbol{\tau}^a$. Following the detailed derivation described in section 3.4 for hybridised formulations, the stabilisation terms leading to the Lax-Friedrichs, Roe, HLL and HLLEM numerical fluxes are presented.

The following notation employed by the corresponding Riemann solvers is recalled. First, let $\boldsymbol{A}_n(\widehat{\boldsymbol{U}}) := [\partial \boldsymbol{F}(\widehat{\boldsymbol{U}})/\partial\widehat{\boldsymbol{U}}]\cdot\boldsymbol{n}$ be the Jacobian of the convective fluxes along the normal direction to a cell face. Moreover, denote by $\widehat{\lambda}_{\mathtt{max}} := |\widehat{\boldsymbol{v}} \cdot \boldsymbol{n}| + \widehat{c}$ the maximum eigenvalue in absolute value of the matrix $\boldsymbol{A}_n(\widehat{\boldsymbol{U}})$, $\widehat{\boldsymbol{v}}$ and $\widehat{c}$ being the velocity and the speed of sound evaluated from $\widehat{\boldsymbol{U}}$, respectively.

2.2.5.1 Lax-Friedrichs Riemann solver

The FCFV stabilisation tensor inspired by the Lax-Friedrichs Riemann solver, see Toro (2009), is defined as

$$\boldsymbol{\tau}^a = \widehat{\lambda}_{\mathtt{max}} \mathbf{I}_{\mathtt{n_{sd}}+2}. \tag{2.23a}$$

with $\widehat{\lambda}_{\mathtt{max}} := |\widehat{\boldsymbol{v}} \cdot \boldsymbol{n}| + \widehat{c}$ being the maximum eigenvalue in absolute value of the Jacobian of the convective fluxes, i.e. $\boldsymbol{A}_n(\widehat{\boldsymbol{U}}) := [\partial \boldsymbol{F}(\widehat{\boldsymbol{U}})/\partial \widehat{\boldsymbol{U}}] \cdot \boldsymbol{n}$. Here, $\widehat{\boldsymbol{v}}$ and $\widehat{c}$ are the velocity and speed of sound evaluated at $\widehat{\boldsymbol{U}}$.

2.2.5.2 Roe Riemann solver

Consider the spectral decomposition $\boldsymbol{A}_n(\widehat{\boldsymbol{U}}) = \boldsymbol{R}\boldsymbol{\Lambda}\boldsymbol{L}$. In addition, the diagonal matrix $\boldsymbol{\Phi}$ is given by $\boldsymbol{\Phi} = \mathrm{diag}\,(\varphi_1, \ldots, \varphi_{\mathtt{n_{sd}}+2})$ where $\varphi_i = \max(|\lambda_i|, \delta)$, $\delta \geq 0$ being a user-defined parameter. The Roe Riemann solver equipped with the *entropy fix* by Harten and Hyman (1983) is obtained for the FCFV method by setting

$$\boldsymbol{\tau}^a = |\boldsymbol{A}_n^\delta(\widehat{\boldsymbol{U}})| = \boldsymbol{R}\boldsymbol{\Phi}\boldsymbol{R}^{-1}. \tag{2.23b}$$

The parameter δ represents the threshold value of the aforementioned Harten-Hyman entropy fix. Such correction aims to remedy the failure of entropy conditions of the Roe solver, which may produce nonphysical solutions in transonic and supersonic cases. It is worth noticing that for $\delta = 0$, $\boldsymbol{\Phi} = |\boldsymbol{\Lambda}|$ and the traditional Roe Riemann solver is retrieved, namely $\boldsymbol{\tau}^a = |\boldsymbol{A}_n(\widehat{\boldsymbol{U}})|$.

2.2.5.3 HLL Riemann solver

The Riemann solver by Harten et al. (1983) (HLL) is devised to recover the Rankine-Hugoniot condition, for a simplified scenario in which contact discontinuities are neglected, without the need of any user-defined parameter. The resulting positivity-preserving Riemann solver for the FCFV method is given by

$$\boldsymbol{\tau}^a = s^+ \mathbf{I}_{\mathtt{n_{sd}}+2}, \tag{2.23c}$$

where $s^+ := \max(0, \widehat{\boldsymbol{v}} \cdot \boldsymbol{n} + \widehat{c})$ is an estimate of the largest wave speed of the Riemann problem.

2.2.5.4 HLLEM Riemann solver

The HLLEM Riemann solver was devised by Einfeldt (1988) and Einfeldt et al. (1991) in order to exploit both the positivity-preserving properties of the HLL Riemann solver and the capability of Roe's method to capture shear layers. Accordingly, the corresponding stabilisation tensor for hybridised formulations is constructed as

$$\boldsymbol{\tau}^a = s^+ \boldsymbol{\theta}(\widehat{\boldsymbol{U}}), \tag{2.23d}$$

where s^+ is the HLL wave speed estimate and $\boldsymbol{\theta}(\widehat{\boldsymbol{U}}) = \boldsymbol{R}\boldsymbol{\Theta}\boldsymbol{L}$ replaces the identity $\mathbf{I}_{\mathtt{n_{sd}}+2}$ in equation (2.23c). Note that the definition of $\boldsymbol{\theta}(\widehat{\boldsymbol{U}})$ exploits the matrices of eigenvectors arising from the spectral decomposition of $\boldsymbol{A}_n(\widehat{\boldsymbol{U}})$, whereas the diagonal matrix $\boldsymbol{\Theta}$ is given by $\boldsymbol{\Theta} = \text{diag}\left(1, \widehat{\theta}\mathbf{1}_{\mathtt{n_{sd}}}, 1\right)$, where $\widehat{\theta} = |\widehat{\boldsymbol{v}} \cdot \boldsymbol{n}|/\widehat{\lambda}_{\mathtt{max}}$.

2.2.6 FCFV discrete problem

The discrete form of the FCFV method is obtained by introducing the definition (2.19) of the numerical fluxes into the local (2.17) and global (2.18) problems. In addition, the vector of conservative variables $\boldsymbol{U}$ and the mixed variables $\boldsymbol{\varepsilon}^d$ and $\boldsymbol{\phi}$ are discretised using a constant value at the centroid of each cell, whereas a constant approximation at the barycentre of the faces is employed for the hybrid vector $\widehat{\boldsymbol{U}}$. Finally, a quadrature rule based on a single integration point is utilised to evaluate the integral quantities on cells and faces.

For each cell Ω_e, the sets of all, $\mathcal{A}_e$, internal, $\mathcal{I}_e$, and boundary, $\mathcal{E}_e$, faces are introduced

$$\mathcal{A}_e := \{1, \ldots, \mathtt{n}_{\mathtt{fa}}^e\}, \qquad \mathcal{I}_e := \{j \in \mathcal{A}_e \mid \Gamma_{e,j} \cap \Gamma \neq \emptyset\}, \qquad \mathcal{E}_e := \mathcal{A}_e \setminus \mathcal{I}_e. \tag{2.24}$$

Moreover, $\chi_{\mathcal{I}_e}$ and $\chi_{\mathcal{E}_e}$ are defined to represent the indicator functions associated with the sets $\mathcal{I}_e$ and $\mathcal{E}_e$, respectively.

The semi-discrete form of the FCFV local problem (2.17) is: for $e = 1, \ldots, \mathtt{n_{el}}$, given the initial state $\boldsymbol{U}_e = \boldsymbol{U}_e^0$ at $t = 0$ and the hybrid vector $\widehat{\boldsymbol{U}}_j$ on the faces $\Gamma_{e,j}$, $j = 1, \ldots, \mathtt{n}_{\mathtt{fa}}^e$, compute $(\boldsymbol{U}_e, \boldsymbol{\varepsilon}_e^d, \boldsymbol{\phi}_e)$ that satisfy

$$|\Omega_e|\boldsymbol{\varepsilon}_e^d - \sum_{j \in \mathcal{A}_e} |\Gamma_{e,j}|\mathcal{D}\widehat{\boldsymbol{v}}_j \otimes \boldsymbol{n}_j = \boldsymbol{0}, \tag{2.25a}$$

$$|\Omega_e|\boldsymbol{\phi}_e - \sum_{j \in \mathcal{A}_e} |\Gamma_{e,j}|\widehat{T}_j \boldsymbol{n}_j = \boldsymbol{0}, \tag{2.25b}$$

$$\int_{\Omega_e} \frac{\partial \boldsymbol{U}_e}{\partial t} \, d\Omega + \sum_{j \in \mathcal{A}_e} |\Gamma_{e,j}| \left\{ \boldsymbol{F}(\widehat{\boldsymbol{U}}_j) \boldsymbol{n}_j - \boldsymbol{G}(\widehat{\boldsymbol{U}}_j, \boldsymbol{\varepsilon}_e^d, \boldsymbol{\phi}_e) \boldsymbol{n}_j \right.$$

$$\left. + \left(\boldsymbol{\tau}^a(\widehat{\boldsymbol{U}}_j) + \boldsymbol{\tau}^d \right) (\boldsymbol{U}_e - \widehat{\boldsymbol{U}}_j) \right\} = \boldsymbol{0}. \tag{2.25c}$$

Remark 2.6 (Symmetry of the mixed variable)**.** The mixed variable $\boldsymbol{\varepsilon}^d$ is a second-order symmetric tensor commonly represented using a matrix of dimension $\mathtt{n_{sd}} \times \mathtt{n_{sd}}$. In order to exploit the symmetry property in its discretisation, Voigt notation is employed to store only its $\mathtt{m_{sd}} = \mathtt{n_{sd}}(\mathtt{n_{sd}} + 1)/2$ non-redundant components. This approach, detailed in appendix A, was first proposed in the context of hybrid discretisation methods for high-order HDG formulations by Giacomini et al. (2018, 2020) and Sevilla et al. (2018), and later exploited also for FCFV approaches by Sevilla et al. (2019). For the simulation of weakly-compressible flows, this approximation of the deviatoric strain rate tensor was discussed in La Spina et al. (2020) and is also employed for the high-order HDG formulation of compressible flows detailed in chapter 3.

Remark 2.7 (Voigt notation for the deviatoric strain rate)**.** Because of the particular definition of the mixed variable $\boldsymbol{\varepsilon}^d$, a symmetric tensor or order $\mathtt{n_{sd}}$, its discrete counterpart $\boldsymbol{\varepsilon}_e^d$ can be expressed employing Voigt notation. In this manner, the re-arrangement of the non-redundant components of the $\mathtt{n_{sd}} \times \mathtt{n_{sd}}$ tensor into an $\mathtt{m_{sd}}$-dimensional vector, with $\mathtt{m_{sd}} = \mathtt{n_{sd}}(\mathtt{n_{sd}} + 1)/2$, is exploited. This approach follows directly from the studies by Sevilla et al. (2018) and Giacomini et al. (2018, 2020).

Remark 2.8 (Pseudo-time in steady-state flows)**.** The present work focuses on the development of a novel FV spatial discretisation for steady-state compressible flows. In this context, t represents an artificial pseudo-time and time marching algorithms are introduced to speed-up the convergence of the nonlinear solver, as detailed as follows.

Remark 2.9 (Time integration scheme)**.** In order to obtain the fully-discrete form of the local problem (2.25c), an appropriate time integration scheme needs to be introduced. As previously mentioned, the present work proposes a novel FV spatial discretisations and the numerical examples in sections 2.3 and 2.4 focus on steady-state flows, whence this term is neglected. Nonetheless, it is worth mentioning that time marching based on an artificial time is a common relaxation approach to speed-up the convergence of a nonlinear solver. In this context, time derivative may be

discretised using a backward Euler scheme, that is

$$\int_{\Omega_e} \frac{\partial \boldsymbol{U}_e}{\partial t} \, d\Omega \simeq \frac{|\Omega_e|}{\Delta t} \left(\boldsymbol{U}_e^{n+1} - \boldsymbol{U}_e^n \right), \tag{2.26}$$

where Δt is the artificial time step. Note that similar FCFV discrete problems are obtained using other implicit time integration schemes, such as higher-order backward difference formulae (BDF), providing additional accuracy in the simulation of transient phenomena, see for instance Nguyen and Peraire (2012), Jaust and Schütz (2014) or Komala-Sheshachala et al. (2020). Of course, in the case of transient simulations, Newton-Raphson iterations are performed at each time step to solve the nonlinear problem.

In a similar fashion, the discrete form of the FCFV global problem (2.18) is: compute the hybrid vector $\widehat{\boldsymbol{U}}$ such that

$$\sum_{e=1}^{\mathtt{n_{el}}} |\Gamma_{e,i}| \left\{ \left[\boldsymbol{F}(\widehat{\boldsymbol{U}}_i)\boldsymbol{n}_i - \boldsymbol{G}(\widehat{\boldsymbol{U}}_i, \boldsymbol{\varepsilon}_e^d, \boldsymbol{\phi}_e)\boldsymbol{n}_i + \left(\boldsymbol{\tau}^a(\widehat{\boldsymbol{U}}_i) + \boldsymbol{\tau}^d \right) (\boldsymbol{U}_e - \widehat{\boldsymbol{U}}_i) \right] \chi_{\mathcal{I}_e}(i) \right.$$
$$\left. + \widehat{\boldsymbol{B}}(\boldsymbol{U}, \widehat{\boldsymbol{U}}, \boldsymbol{\varepsilon}^d, \boldsymbol{\phi})\chi_{\mathcal{E}_e}(i) \right\} = \boldsymbol{0}, \quad (2.27)$$

for all $i \in \mathcal{A}_e$.

It is worth noticing that both the local (2.25) and global (2.27) problems are nonlinear. More precisely, let $\boldsymbol{Q}_e = (\boldsymbol{\varepsilon}_e^d, \boldsymbol{\phi}_e)$ be the set of mixed variables introduced by the FCFV formulation in the cell Ω_e. The resulting system of algebraic-differential equations arising from the local problem (2.25) is

$$\mathbf{Q}_e = \mathbf{Q}_e(\widehat{\mathbf{U}}), \tag{2.28a}$$

$$|\Omega_e|\frac{d\mathbf{U}_e}{dt} + \mathbf{R}_e(\mathbf{U}_e, \mathbf{Q}_e, \widehat{\mathbf{U}}) = \mathbf{0}, \tag{2.28b}$$

where $\mathbf{U}_e$ and $\mathbf{Q}_e$ are the vectors containing the values of the local and mixed variables, respectively, at the centroid of the cell, whereas the vector $\widehat{\mathbf{U}}$ collects the values of the hybrid variable at the barycentres of its faces. On the one hand, equations (2.25a) and (2.25b) provide analytical expressions of the mixed variables in terms of the hybrid unknown, see equation (2.28a). On the other hand, equation (2.25c) is nonlinear and the residual vector obtained from its spatial discretisation is denoted by $\mathbf{R}_e$. Upon linearisation of equation (2.28b) via a Newton-Raphson procedure, the $\mathtt{n_{el}}$ local problems allow to express $\mathbf{U}_e$ and $\mathbf{Q}_e$ in each cell Ω_e, $e = 1, \ldots, \mathtt{n_{el}}$ in terms of the

unknown $\widehat{\mathbf{U}}$ on its faces. The resulting expressions are plugged into equation (2.27) and all the degrees of freedom inside the cells are eliminated from the global problem, leading to

$$\sum_{e=1}^{\mathbf{n_{el}}} \widehat{\mathbf{R}}_e(\widehat{\mathbf{U}}) = \mathbf{0}, \tag{2.29}$$

where $\widehat{\mathbf{R}}_e$ is the nonlinear residual vector related to the unknowns $\widehat{\mathbf{U}}$ associated with cell Ω_e. The global problem (2.29), whose structure arising from the hybridisation procedure is detailed as follows, is thus solved by means of a Newton-Raphson linearisation.

2.2.7 Hybridisation of the FCFV solver

The hybrid nature of the FCFV method allows the solution procedure to be featured in two stages, see 2.2.4. First, the $\mathbf{n_{el}}$ local problems (2.25) are devised, in order to eliminate the unknowns $(\boldsymbol{U}_e, \boldsymbol{\varepsilon}_e^d, \boldsymbol{\phi}_e)$ within each cell by expressing them as functions of the hybrid vector $\widehat{\boldsymbol{U}}$. Stemming from equation (2.28), the FCFV local problem for Ω_e, $e = 1, \ldots, \mathbf{n_{el}}$ is given by

$$\mathbf{A}_{QQ}^e \mathbf{Q}_e = \mathbf{A}_{Q\widehat{U}}^e \widehat{\mathbf{U}} + \mathbf{F}_Q^e, \tag{2.30a}$$

$$\mathbf{A}_{UU}^e \mathbf{U}_e + \mathbf{A}_{UQ}^e \mathbf{Q}_e = \mathbf{A}_{U\widehat{U}}^e \widehat{\mathbf{U}} + \mathbf{F}_U^e, \tag{2.30b}$$

where the matrices and vectors above arise from the Newton-Raphson linearisation of nonlinear system of equations (2.25).

Following from the constant degree of approximation utilised to approximate $\mathbf{U}_e$ and $\mathbf{Q}_e$ at the centroid of each cell and $\widehat{\mathbf{U}}$ at the barycentre of each face and from the quadrature rule employing a single integration point on cell and faces, the primal, $\mathbf{U}_e$, and mixed, $\mathbf{Q}_e$, variables are expressed as functions of the hybrid unknown $\widehat{\boldsymbol{U}}$ in a decoupled manner, namely

$$\mathbf{Q}_e = \left[\mathbf{A}_{QQ}^e\right]^{-1} \mathbf{A}_{Q\widehat{U}}^e \widehat{\mathbf{U}} + \left[\mathbf{A}_{QQ}^e\right]^{-1} \mathbf{F}_Q^e, \tag{2.31a}$$

$$\mathbf{U}_e = \left[\mathbf{A}_{UU}^e\right]^{-1} \left(\mathbf{A}_{U\widehat{U}}^e - \mathbf{A}_{UQ}^e \left[\mathbf{A}_{QQ}^e\right]^{-1} \mathbf{A}_{Q\widehat{U}}^e\right) \widehat{\mathbf{U}} + \left[\mathbf{A}_{UU}^e\right]^{-1} \left(\mathbf{F}_U^e - \mathbf{A}_{UQ}^e \left[\mathbf{A}_{QQ}^e\right]^{-1} \mathbf{F}_Q^e\right). \tag{2.31b}$$

It is worth noticing that the computations in equation (2.31) are independent cell-by-cell and only involve the inverses of matrices $\mathbf{A}_{UU}^e$ and $\mathbf{A}_{QQ}^e$. The former is a matrix of dimension $(\mathbf{n_{sd}} + 2) \times (\mathbf{n_{sd}} + 2)$, that is, 4×4 in 2D and 5×5 in 3D. The latter

is the identity matrix of dimension $(\mathtt{m_{sd}} + \mathtt{n_{sd}}) \times (\mathtt{m_{sd}} + \mathtt{n_{sd}})$ (i.e., 5×5 in 2D and 9×9 in 3D) scaled by the volume of the cell Ω_e. Hence, this step requires a reduced computational effort and can be easily performed in parallel.

Similarly, upon linearisation via the Newton-Raphson method, the global problem (2.27) is expressed as

$$\sum_{e=1}^{\mathtt{n_{el}}} \left\{ \mathbf{A}_{\widehat{U}\widehat{U}}^e \widehat{\mathbf{U}} + \begin{bmatrix} \mathbf{A}_{\widehat{U}U}^e & \mathbf{A}_{\widehat{U}Q}^e \end{bmatrix} \begin{Bmatrix} \mathbf{U}_e \\ \mathbf{Q}_e \end{Bmatrix} - \mathbf{F}_{\widehat{U}}^e \right\} = \mathbf{0}. \tag{2.32}$$

By plugging the expressions obtained from equation (2.31) into equation (2.32), the number of unknowns is reduced by eliminating the local unknowns $\mathbf{U}_e$ and $\mathbf{Q}_e$ from the global problem. Hence, at each Newton-Raphson iteration, the linear system

$$\mathbf{K}\widehat{\Delta\mathbf{U}} = \mathbf{F}, \tag{2.33}$$

is solved, where the matrix $\mathbf{K}$ and the vector $\mathbf{F}$ are obtained from the assembly of the contributions from each cell, namely

$$\mathbf{K}^e = \mathbf{A}_{\widehat{U}\widehat{U}}^e + \begin{bmatrix} \mathbf{A}_{\widehat{U}U}^e & \mathbf{A}_{\widehat{U}Q}^e \end{bmatrix} \begin{bmatrix} [\mathbf{A}_{UU}^e]^{-1} \left(\mathbf{A}_{U\widehat{U}}^e - \mathbf{A}_{UQ}^e [\mathbf{A}_{QQ}^e]^{-1} \mathbf{A}_{Q\widehat{U}}^e \right) \\ [\mathbf{A}_{QQ}^e]^{-1} \mathbf{A}_{Q\widehat{U}}^e \end{bmatrix}, \tag{2.34a}$$

$$\mathbf{F}^e = \mathbf{F}_{\widehat{U}}^e - \begin{bmatrix} \mathbf{A}_{\widehat{U}U}^e & \mathbf{A}_{\widehat{U}Q}^e \end{bmatrix} \begin{Bmatrix} [\mathbf{A}_{UU}^e]^{-1} \left(\mathbf{F}_U^e - \mathbf{A}_{UQ}^e [\mathbf{A}_{QQ}^e]^{-1} \mathbf{F}_Q^e \right) \\ [\mathbf{A}_{QQ}^e]^{-1} \mathbf{F}_Q^e \end{Bmatrix}. \tag{2.34b}$$

2.3 Numerical convergence studies

In this section, the optimal convergence of the FCFV method is examined for different compressible flows, namely inviscid and viscous laminar flows. The accuracy of the method is evaluated using different types of meshes, employing both triangular and quadrilateral elements, with special attention to the robustness of the methodology to cell distortion and stretching.

2.3.1 Inviscid Ringleb flow

The convergence properties of the FCFV method in the inviscid limit are examined through the Ringleb flow problem. This 2D example describes a smooth transonic flow, for which there exists an analytical expression of the solution, obtained via the hodograph method as described by Chiocchia (1985).

At a given point (x, y), the solution is obtained as result of the following nonlinear implicit equation

$$\left(x + \frac{J}{2}\right)^2 + y^2 = \frac{1}{4\rho^2 V^4}, \tag{2.35}$$

where c is the speed of sound, whereas density ρ, velocity magnitude V, pressure p and J are determined as

$$\rho = c^{2/(\gamma-1)}, \quad V = \sqrt{\frac{2(1-c^2)}{\gamma - 1}}, \quad p = \frac{1}{\gamma}c^{2\gamma/(\gamma-1)}, \quad J = \frac{1}{c} + \frac{1}{3c^3} + \frac{1}{5c^5} - \frac{1}{2}\log\left(\frac{1+c}{1-c}\right). \tag{2.36}$$

Finally, the velocity vector field is given by

$$\boldsymbol{v} = \left\{\begin{array}{c} -\operatorname{sgn}(y)V\sin\theta \\ V\cos\theta \end{array}\right\} \tag{2.37}$$

being $\operatorname{sgn}(\cdot)$ the *sign* operator, $\sin\theta := \Psi V$ and

$$\Psi := \sqrt{\frac{1}{2V^2} + \rho\left(x + \frac{J}{2}\right)}. \tag{2.38}$$

Remark 2.10 (Domain of the Ringleb solution). Classicaly, the Ringleb flow problem has been solved in a curvilinear domain symbolising a channel around a symmetric blunt obstacle, bounded by two streamlines of the flowfield, as employed by Bassi and Rebay (1997b), Hartmann and Houston (2003), Wang and Liu (2006), Dumbser et al. (2007) or Vymazal et al. (2015). In such domain, the flow is transonic, displaying a large supersonic region near the nose of the blunt body. Alternatively, this problem has also been studied in rectangular domains located at different regions, thus avoiding the introduction of geometric errors in the approximation of the curved boundaries. Numerical tests performed both in regions of subsonic or transonic speeds have been presented in the literature by Nguyen and Peraire (2012) and Komala-Sheshachala et al. (2020), respectively.

In this work, the Ringleb problem is solved in the domain of transonic flow $\Omega = [0, 1]^2$, such as Komala-Sheshachala et al. (2020), with a far-field boundary condition imposed on $\partial\Omega$. Figure 2.1 displays two levels of refinement of the domain using uniform meshes of triangular and quadrilateral cells.

The corresponding approximation of the Mach number distribution on these meshes is reported in figure 2.2.

(a) Mesh M2   (b) Mesh M4   (c) Mesh M2   (d) Mesh M4
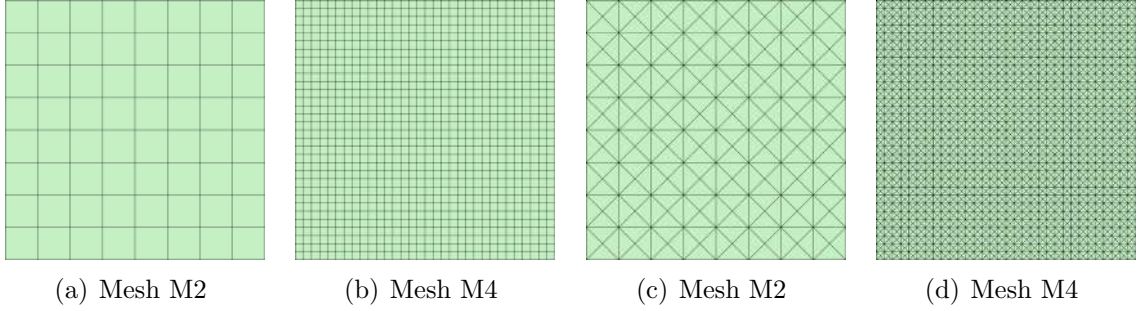
Figure 2.1: Uniform (a-b) quadrilateral and (c-d) triangular meshes of $\Omega = [0,1]^2$.

(a) Quadrilaterals M2   (b) Quadrilaterals M4   (c) Triangles M2   (d) Triangles M4
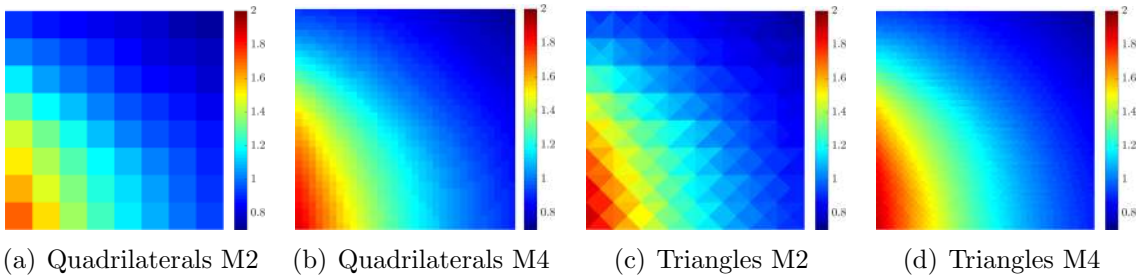
Figure 2.2: Ringleb flow - Mach number distribution using the (a-b) quadrilateral and (c-d) triangular meshes in Figure 2.1 employing the HLL Riemann solver.

The relative error of the numerical approximation, measured in the $\mathcal{L}_2(\Omega)$ norm as function of the characteristic mesh size h, is examined for the the four Riemann solvers discussed in section 2.2.5. The h-convergence study is performed using the sets of meshes introduced above and the results are displayed in figure 2.3.

(a) Density, ρ (b) Momentum, $\rho\boldsymbol{v}$ (c) Energy, ρE
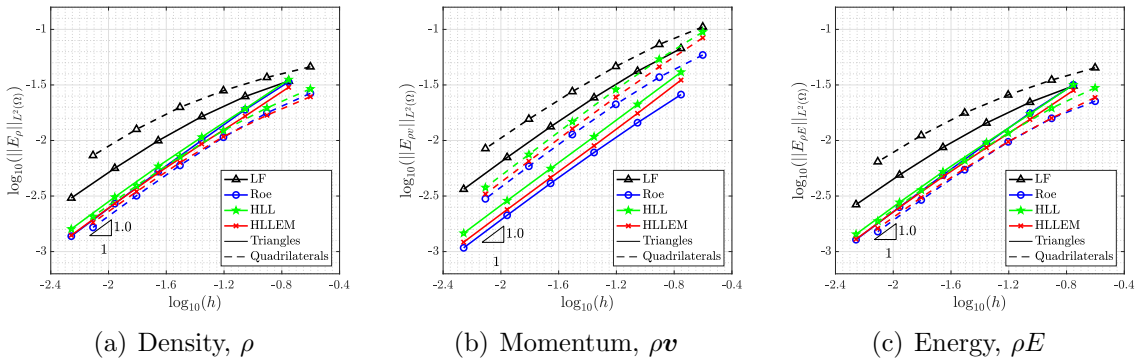
Figure 2.3: Ringleb flow - h-convergence of the error of (a) density, (b) momentum and (c) energy in the $\mathcal{L}_2(\Omega)$ norm, using Lax-Friedrichs (LF), Roe, HLL and HLLEM Riemann solvers and uniform meshes of triangles and quadrilaterals.

Optimal convergence of order 1 is obtained for the approximation of the conservative variables regardless of the Riemann solver utilised, showing the robustness of

the FCFV approach in the inviscid case. The method displays optimal convergence properties using both triangular and quadrilateral cells. Errors of the order of 10^{-3} are achieved, independently of the type of cells, by Roe, HLL and HLLEM Riemann solvers in the approximation of density and energy. Concerning the momentum, similar levels of accuracy are obtained using the three Riemann solvers on triangular meshes, whereas the errors are slightly higher using quadrilateral cells. The Lax-Friedrichs (LF) numerical flux displays the worst performance among the analysed Riemann solvers, showing errors almost half an order of magnitude and almost one order of magnitude higher using triangular and quadrilateral meshes, respectively.

2.3.2   Viscous laminar Couette flow

A Couette flow with source term, introduced by Nguyen and Peraire (2012) or Schütz et al. (2012), is defined in the domain $\Omega = [0, 1]^2$ to examine the convergence properties of the FCFV method in the viscous laminar regime. The analytical expressions of velocity, pressure and temperature, are

$$
\begin{aligned}
\boldsymbol{v} &= \begin{Bmatrix} y \log(1 + y) \\ 0 \end{Bmatrix}, \qquad p = \frac{1}{\gamma M_\infty^2} \\
T &= \frac{1}{(\gamma - 1)M_\infty^2} \left[\alpha_c + y(\beta_c - \alpha_c) + \frac{(\gamma - 1)M_\infty^2 Pr}{2} y(1 - y) \right],
\end{aligned}
\tag{2.39}
$$

where $\alpha_c = 0.8$, $\beta_c = 0.85$ and the free-stream Mach number is set to $M_\infty = 0.15$ Assuming constant viscosity, the source term is determined from the exact solution and is given by

$$
\boldsymbol{S} = \frac{-1}{Re} \left\{ 0, \ \frac{2 + y}{(1 + y)^2}, \ 0, \ \log^2(1 + y) + \frac{y \log(1 + y)}{1 + y} + \frac{y(3 + 2y)\log(1 + y) - 2y - 1}{(1 + y)^2} \right\}^T.
\tag{2.40}
$$

Finally, the boundary conditions are prescribed on $\partial\Omega$ employing the expression of the analytical solution.

The h-convergence study is performed in the meshes of triangular cells in figure 2.1. Figure 2.4 reports the results using different Riemann solvers and for Reynolds number $Re = 1$ and $Re = 100$.

The approximation of the conservative variables displays optimal convergence regardless of the Reynolds number and of the employed Riemann solver. The proposed method is thus able to provide optimal accuracy in the conservative quantities also in

(a) Density, ρ (b) Momentum, $\rho\boldsymbol{v}$ (c) Energy, ρE

(d) Viscous stress, $\boldsymbol{\sigma}^d$ (e) Heat flux, $\boldsymbol{q}$
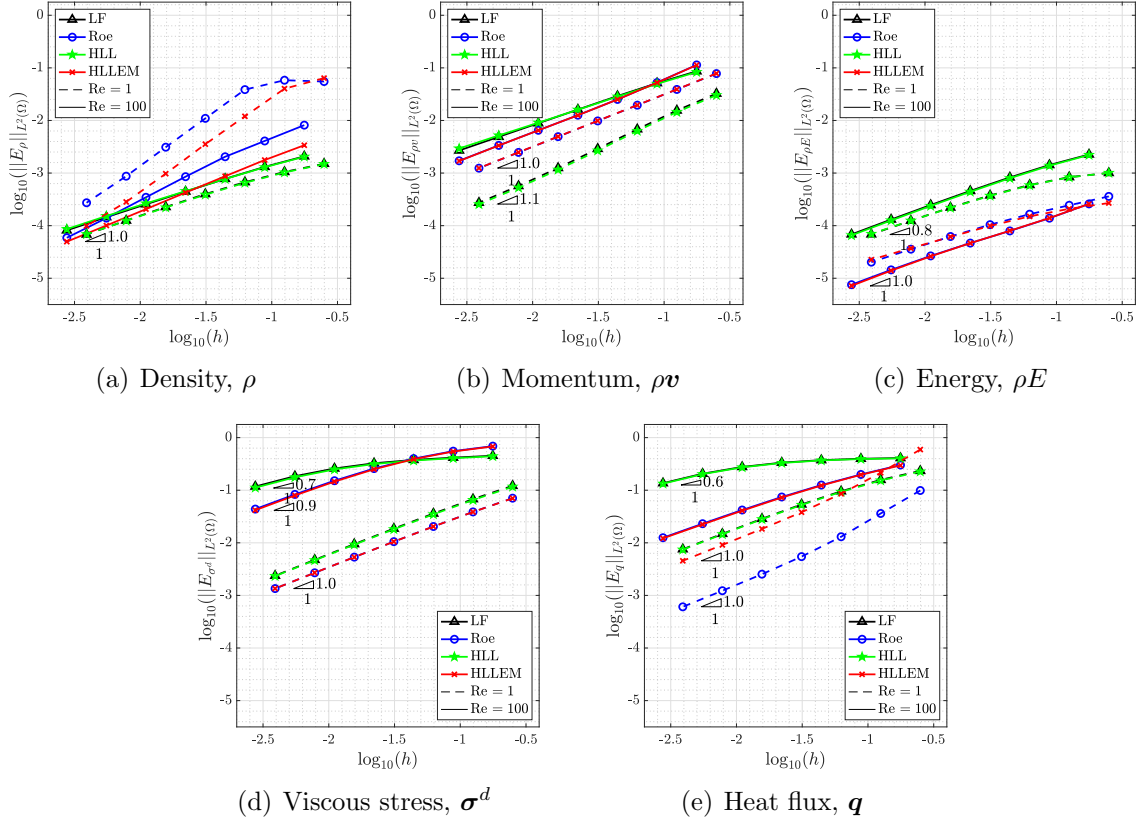
Figure 2.4: Couette flow - h-convergence of the error of (a) density, (b) momentum (c) energy, (d) viscous stress tensor and (e) heat flux in the $\mathcal{L}_2(\Omega)$ norm, using Lax-Friedrichs (LF), Roe, HLL and HLLEM Riemann solvers and Reynolds number $Re = 1$ and $Re = 100$.

case viscous phenomena are considered, with errors between 10^{-3} and 10^{-5}. Regarding the viscous stress tensor and the heat flux, optimal accuracy is achieved using HLLEM and Roe Riemann solvers independently of the Reynolds number, whereas the Lax-Friedrichs and HLL fluxes appear to be more sensitive to increasing values of the Reynolds number.

Finally, it is worth mentioning that the test case under analysis features an incompressible flow ($\nabla \cdot \boldsymbol{v} = 0$, $M_\infty = 0.15$). Despite this additional difficulty, the FCFV method is capable of computing an accurate approximation without the need of introducing specific pressure corrections like the well-known SIMPLE algorithm described by Patankar and Spalding (1972). Thus, an important advantage of the proposed methodology is its robustness in the incompressible limit as further detailed in section 2.4.3.

2.3.3   Influence of cell distortion and stretching

In this section, the sensitivity of the FCFV method to cell distortion and stretching is investigated. For the sake of brevity, this study focuses on the viscous case in order to analyse the effect of mesh regularity on both conservative and mixed variables. To this end, two sets of meshes are generated for the domain $\Omega = [0,1]^2$ by modifying the regular ones employed in the previous examples.

First, a set of highly distorted meshes is generated by introducing a perturbation on the position of the interior nodes of the regular meshes illustrated in figure 4.1.First, a set of highly distorted meshes is generated by introducing a perturbation on the position of the interior nodes of the regular meshes illustrated in figure 4.1.

In particular, for a given node i, its new position is defined as $\tilde{\boldsymbol{x}}_i = \boldsymbol{x}_i + \boldsymbol{r}_i$, $\boldsymbol{r}_i$ being an $\mathtt{n_{sd}}$-dimensional vector whose components are randomly generated within the interval $[-\ell_{\min}/3, \ell_{\min}/3]$, where $\ell_{\min}$ denotes the minimum edge length of the regular mesh. The third and fifth level of refinement of the meshes featuring distorted quadrilateral and triangular cells are illustrated in figure 2.5.
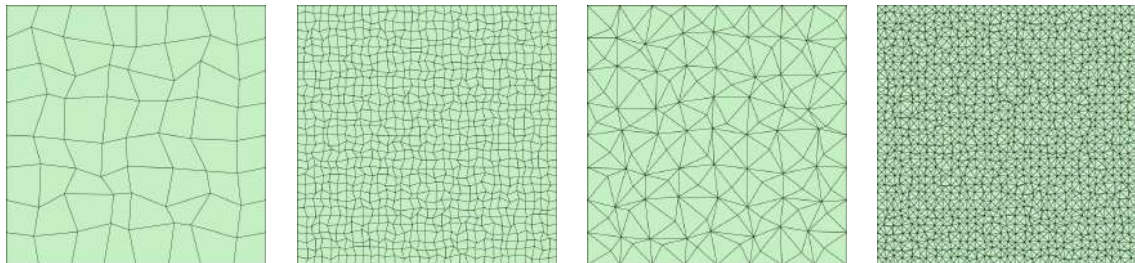
(a)   Distorted   mesh M3D

(b)   Distorted   mesh M5D

(c)   Distorted   mesh M3D

(d)   Distorted   mesh M5D

Figure 2.5: Distorted meshes of $\Omega = [0,1]^2$ featuring (a-b) quadrilateral and (c-d) triangular cells.

The previously introduced Couette flow example for Reynolds number $Re = 100$ is also employed for the current sensitivity study. More precisely, figure 2.6 shows the approximation of the Mach number distribution on the meshes of distorted cells in figure 2.5 employing the HLLEM Riemann solver.

Second, a set of meshes with stretching near the bottom boundary is produced. For its construction in 2D, the vertical coordinate of the first mesh layer is fixed at the desired stretching factor s. Then, the vertical coordinate of the subsequent layers

(a) Quadrilaterals M3D (b) Quadrilaterals M5D (c) Triangles M3D (d) Triangles M5D
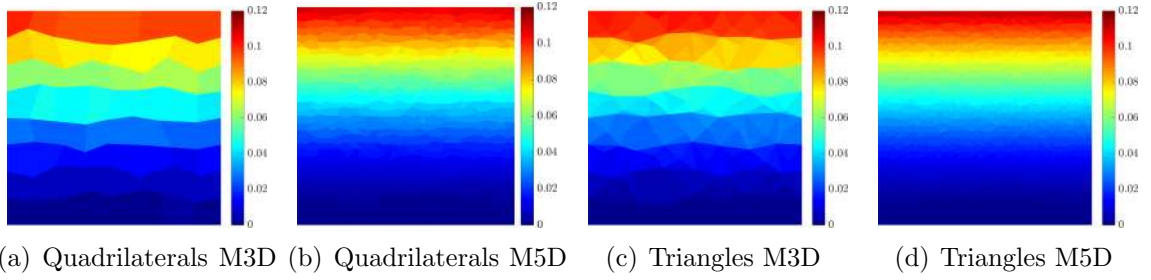
Figure 2.6: Couette flow - Mach number distribution using the distorted (a-b) quadrilateral and (c-d) triangular meshes in Figure 2.5 employing the HLLEM Riemann solver.

is defined as

$$y_k = y_{k-1} + \frac{h}{s}\beta^{k-1}, \qquad \text{for } k = 2, \ldots, N_y + 1 \tag{2.41}$$

where h is the maximum edge length of the corresponding regular mesh, N_y is the number of cells in the vertical direction and the growth rate factor β is computed by imposing that the vertical coordinate of the last layer is one, that is by finding the roots of

$$\frac{h}{s}\beta^{N_y} - \beta + 1 - \frac{h}{s} = 0. \tag{2.42}$$

Figure 2.7 reports the second level of refinement of a set of triangular meshes for different levels of stretching s.

(a) $s = 0$ (b) $s = 10$ (c) $s = 100$ (d) $s = 1,000$
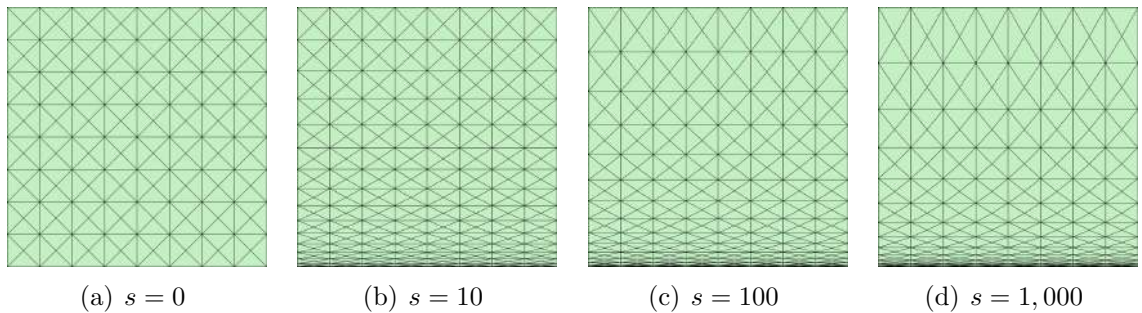
Figure 2.7: Second level of refinement of the stretched meshes of $\Omega = [0,1]^2$ for different values of the stretching factor s.

A quantitative evaluation of the influence of cell distortion and stretching on the accuracy of the FCFV approximation is performed via an h-convergence study of the error, measured in the $\mathcal{L}_2(\Omega)$ norm, using the HLLEM Riemann solver. The results, reported in figures 2.8(a) and 2.8(b), respectively, show that optimal convergence of order 1 is achieved for all the variables, independently of the distortion or of the

stretching factor of its cells. In addition, the precision of the numerical approximation also results unaffected by the loss of orthogonality and loss of isotropy of the mesh. Indeed, by comparing the results of figure 2.8 with the ones in figure 2.4, almost identical levels of accuracy are obtained in the $\mathcal{L}_2(\Omega)$ error of the approximate solutions using meshes with uniform, distorted or stretched cells.

(a) Effect of distortion on mesh convergence   (b) Effect of stretching on mesh convergence
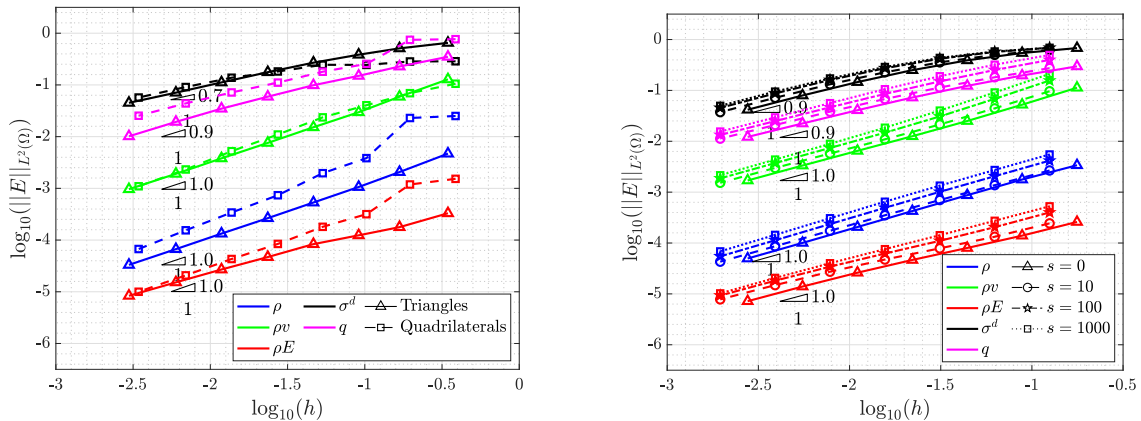
Figure 2.8: Couette flow - h-convergence of the error in the $\mathcal{L}_2(\Omega)$ norm of density, momentum, energy, viscous stress tensor and heat flux in (a) distorted and (b) stretched meshes, using the HLLEM Riemann solver and for Reynolds number $Re = 100$.

2.4   Numerical benchmarks

In this section, a set of numerical examples is presented to show the capabilities of the proposed FCFV method to simulate inviscid and viscous compressible flows at different regimes.

2.4.1   Inviscid transonic flow over a NACA 0012 profile

The first test case considers the inviscid transonic flow over a NACA 0012 aerofoil at free-stream Mach number $M_\infty = 0.8$ and angle of attack $\alpha = 1.25°$. This classical benchmark for inviscid compressible flows, proposed as test case in Kroll (2009) and employed in different studies such as by Sevilla et al. (2013), is proposed to evaluate the ability of the FCFV solver to capture flow solutions involving shock waves. More

precisely, this benchmark is used to demonstrate the importance of the choice of the Riemann solver in the accuracy and stability of the FCFV approximate solution.

Unstructured meshes of triangular cells with non-uniform refinements on the surface of the aerofoil and at the leading and trailing edges are used for the simulation. Figure 2.9 reports the details of a coarse and a fine mesh featuring 89,250 and 712,164 triangular cells, respectively. The far-field boundary is located at 15 chord units away from the profile and the aerofoil surface is defined as an inviscid wall.

(a) Mesh of the computational domain

(b) Coarse mesh
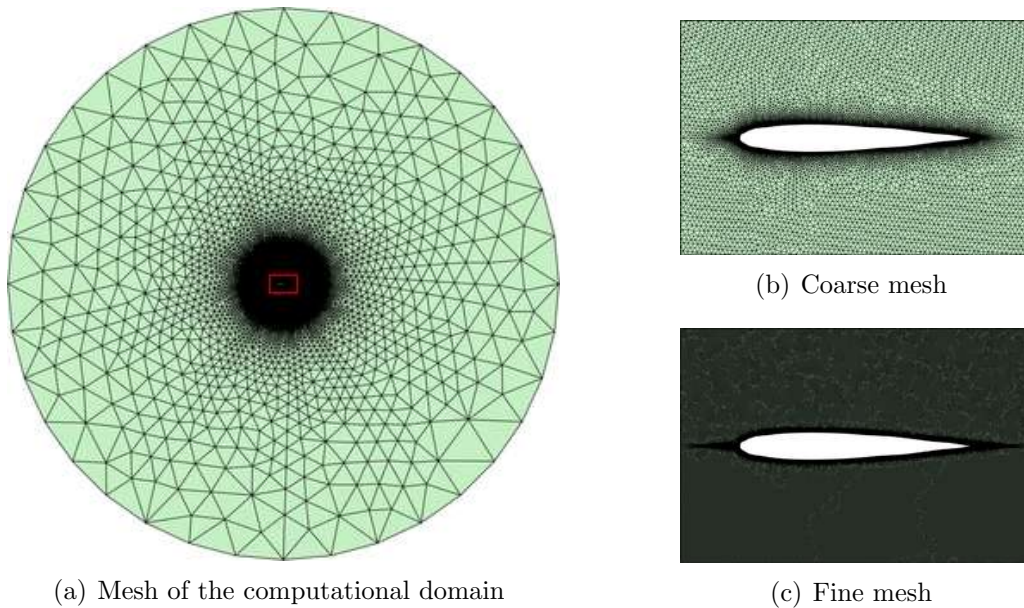
(c) Fine mesh

Figure 2.9: Mesh refinement for the inviscid transonic flow over a NACA 0012 profile.

The Mach number and the pressure distributions computed on the fine mesh using the HLL Riemann solver are displayed in figure 2.10. Both the strong shock wave on the upper surface and the weaker shock in the lower part of the aerofoil are accurately represented. It is worth noticing that the FCFV method provides non-oscillatory solutions in presence of abrupt variations without the need of any shock capturing or limiting mechanism. This property follows form the result on the monotonicity of first-order schemes by Godunov and Bohachevsky (1959). Hence, the FCFV method with the HLL numerical flux ensures the positivity properties of the approximate solution. In addition, the choice of the Riemann solver also controls the amount of numerical diffusion introduced by the FCFV method, influencing the overall accuracy of the computed solution. A qualitative comparison of the different Riemann solvers is performed in figure 2.11 by illustrating the pressure distribution in the fine mesh at different sections along the vertical body axis. The results display that the
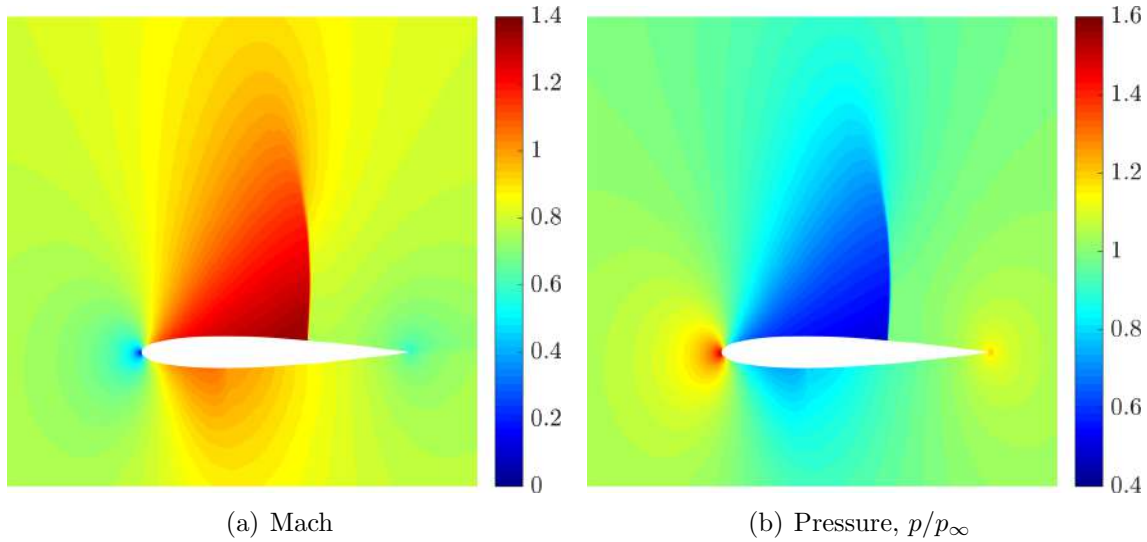
(a) Mach   (b) Pressure, p/p_∞

Figure 2.10: Inviscid transonic flow over a NACA 0012 profile - (a) Mach number and (b) pressure distributions around the aerofoil computed on the fine mesh using the HLL Riemann solver.

Lax-Friedrichs numerical flux provides non-oscillatory solutions. Nonetheless, it introduces excessive numerical dissipation leading to a smeared representation of the shock wave. The Roe Riemann solver is equipped with a Harten-Hyman entropy fix: without this correction, the method fails to converge and nonphysical solutions with localised overshoots appear. On the one hand, using an entropy fix with threshold parameter $\delta = 0.1$, the Roe solver shows insufficient numerical dissipation producing an approximation with oscillations in the vicinity of the shock wave. On the other hand, a threshold value $\delta = 0.15$ for the Roe solver leads to a physically-admissible and accurate solution. It is worth noticing that the parameter δ, which is problem-dependent, needs to be appropriately tuned *a priori* by the user. Finally, HLL-type Riemann solvers exhibit their ability to produce positivity-preserving and accurate solutions in presence of shocks without the need of any user-defined parameter, thus remedying the aforementioned issue of the Roe solver.

To further analyse the accuracy of the Riemann solvers for the FCFV method, the numerical computation of the pressure coefficient over the aerofoil surface is compared with experimental data by Yoshihara and Sacher (1985). Figure 2.12 confirms the overdissipative nature of the Lax-Friedrichs solution which shows a smeared representation of the shock wave. The HLL, HLLEM and the Roe solvers (the latter with an entropy fix parameter $\delta = 0.15$) produce nearly identical solutions with a sharp

(a) $y/c = 0.50$

(b) $y/c = 0.25$

(c) $y/c = 0.10$

(d) $y/c = -0.075$
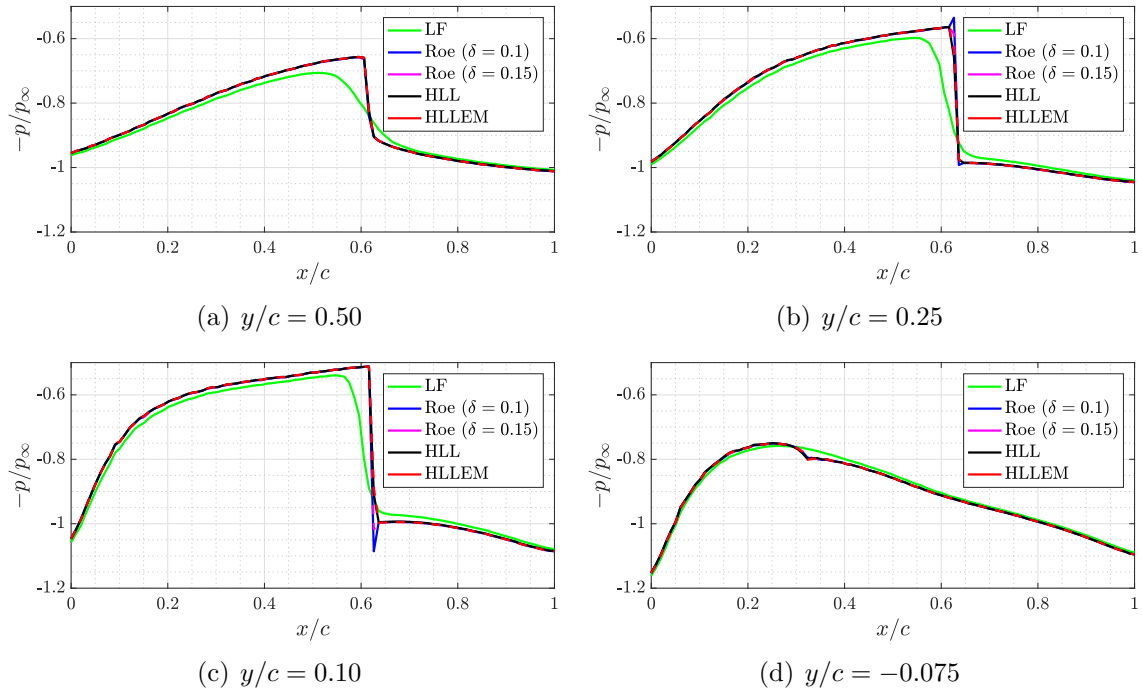
Figure 2.11: Inviscid transonic flow over a NACA 0012 profile - Pressure distribution at different sections parallel to the aerofoil chord using different Riemann solvers.

representation of the shock wave showing excellent agreement with the experimental data.
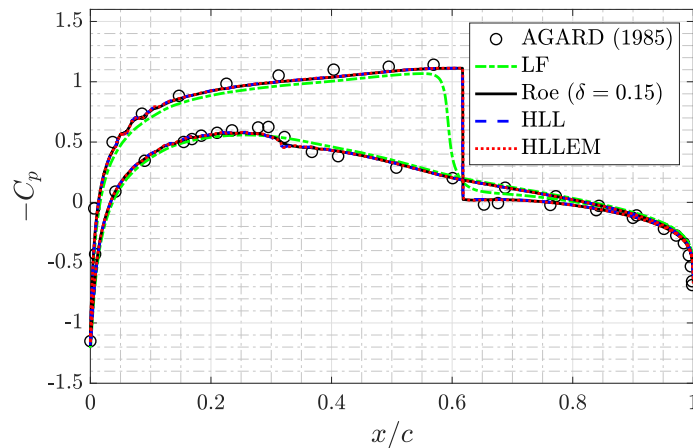
Figure 2.12: Inviscid transonic flow over a NACA 0012 profile - Pressure coefficient around the aerofoil surface computed on the fine mesh using Lax-Friedrichs (LF), Roe, HLL and HLLEM Riemann solvers.

Finally, a quantitative comparison is performed by computing the lift and drag

coefficients, reported in table 2.2. According to experimental data by Thibert et al. (1979), acceptable values lie within the range $[0.342, 0.352]$ for the lift and $[0.0217, 0.0227]$ for the drag coefficient, accounting for a tolerance of 5 lift and drag counts.

Table 2.2: Inviscid transonic flow over a NACA 0012 aerofoil - Lift, C_l, and drag, C_d, coefficients computed on the fine mesh using different Riemann solvers.

	Lax-Friedrichs	Roe ($\delta = 0.15$)	HLL	HLLEM
C_l	0.274	0.312	0.314	0.313
C_d	0.0279	0.0222	0.0236	0.0223

The reported values for the drag coefficient employing the Roe and HLLEM Riemann solvers lie within the specified reference intervals, whereas the value obtained with the HLL solution is at 9 drag counts. Regarding the lift coefficient, the obtained results show an underestimation of this quantity, regardless of the employed Riemann solver. It is worth noticing that the proximity of the far-field boundary has a strong influence on the precision of the computed quantities, as reported by Yano and Darmofal (2012) or Wang et al. (2013). Indeed, the presented results are in quantitative agreement with references employing a similar domain, see e.g. Sevilla et al. (2013) where the far-field boundary is located at 20 chord units from the aerofoil. In the work by Sevilla et al. (2013), the value of the lift coefficient computed using a first-order stabilised finite element approximation is 0.308, differing between 4 and 6 lift counts from the FCFV solution provided by Roe, HLL and HLLEM Riemann solvers.

2.4.2   Viscous laminar transonic flow over a NACA 0012 aerofoil

The next example consists of the viscous laminar transonic flow over a NACA 0012 profile at free-stream Mach number $M_\infty = 0.8$ and angle of attack $\alpha = 10°$. The Reynolds number, based on the chord length of the aerofoil, is $Re = 500$. This benchmark is presented to establish the capability of the FCFV method to concurrently capture abrupt variations due to shock waves and viscous effects in boundary layers and has been presented as test case by Bristeau et al. (1987) and employed by Nogueira et al. (2009) or Sevilla et al. (2013) for verification purposes.

As for the meshes utilised in the previous section, a non-uniform refinement is performed near the aerofoil surface. In addition, exploiting the information on the

angle of attack of the free-stream, *a priori* mesh refinement is introduced in a region surrounding the aerofoil, tilted 10° from its mean chord line, in order to accurately capture the viscous effects of the flow in the wake of the profile. An unstructured mesh of 1,005,199 triangular cells is displayed in figure 2.13(a) and a detail of its refinement on the surface of the aerofoil is reported in figure 2.13(b). The far-field boundary is located at 15 chord units from the profile and the aerofoil surface is considered adiabatic.

(a) Mesh   (b) Refinement on the surface
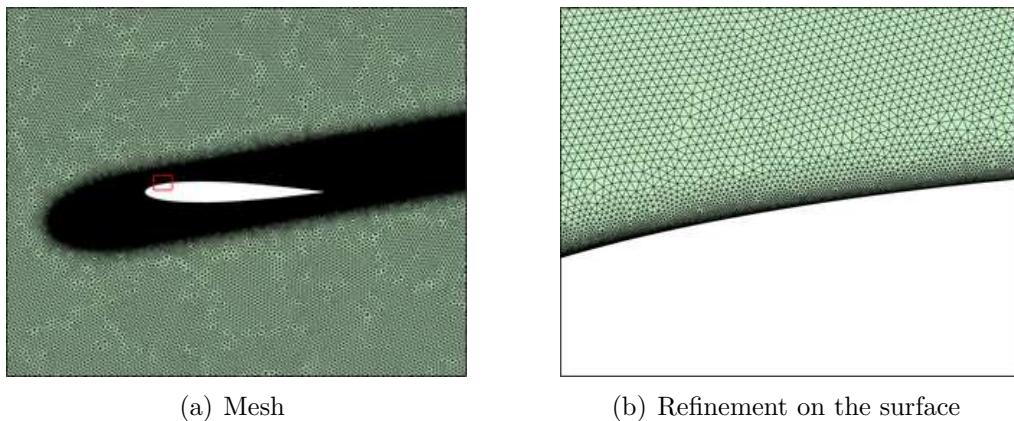
Figure 2.13: Mesh for the viscous laminar transonic flow over a NACA 0012 profile.

The flowfield computed with the HLLEM Riemann solver is depicted in figure 2.14. The Mach number distribution illustrates the capacity of the method to accurately describe the detached sonic region near the leading edge as well as the appearance of a wake behind the profile.

The different Riemann solvers for the FCFV method are compared for this viscous test case in figure 2.15. The results display the pressure and the skin friction coefficients, computed on the aerofoil surface, as well as the numerical results obtained by Kordulla in Bristeau et al. (1987). Similarly to the results observed in the inviscid simulation, the Lax-Friedrichs Riemann solver displays discrepancies with respect to the reference curves for both the pressure and the skin friction coefficient. The Lax-Friedrichs results are matched by the ones provided by the HLL Riemann solver which shows an excessive numerical dissipation in the viscous boundary layer. The overdiffusive nature of the HLL numerical flux, not observed in the inviscid case, is attributed to its misrepresentation of contact and shear waves, as reported by Einfeldt (1988) and Einfeldt et al. (1991). Concerning Roe numerical flux, this Riemann solver strongly depends upon the choice of the value of the entropy fix also in the
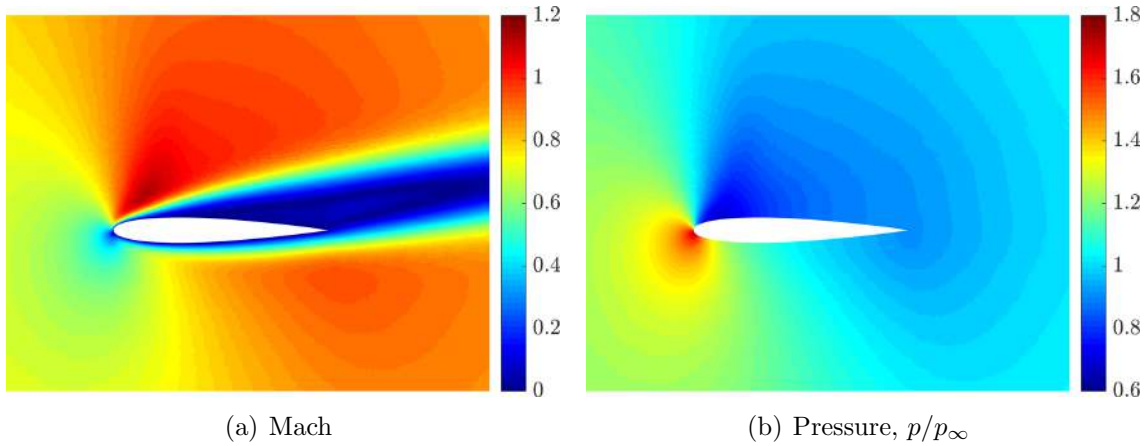
(a) Mach

(b) Pressure, p/p_∞

Figure 2.14: Viscous laminar transonic flow over a NACA 0012 profile - (a) Mach number and (b) pressure distributions around the aerofoil computed using the HLLEM Riemann solver.

(a) Pressure coefficient

(b) Skin friction coefficient
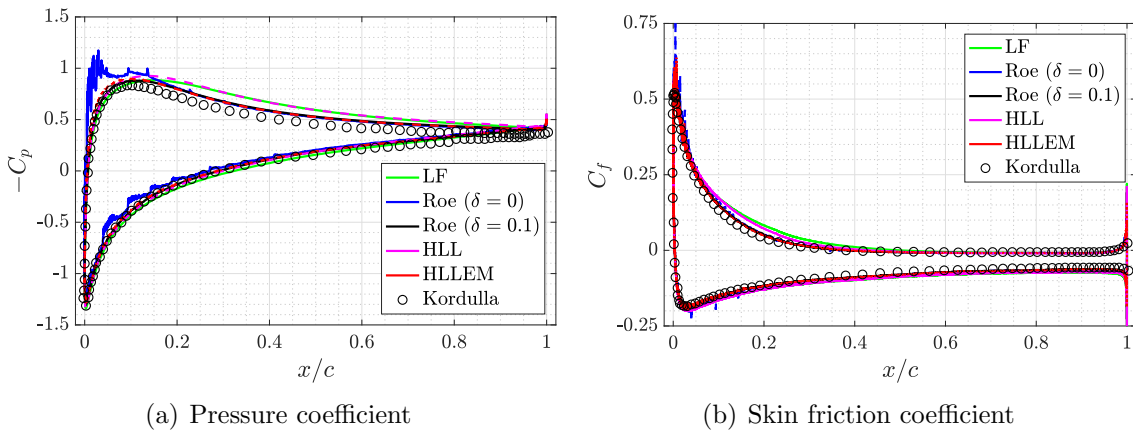
Figure 2.15: Viscous laminar transonic flow over a NACA 0012 profile - (a) Pressure and (b) skin friction coefficient on the aerofoil surface computed using Lax-Friedrichs (LF), Roe, HLL and HLLEM Riemann solvers.

viscous case. Without entropy fix ($\delta = 0$), numerical oscillations of the solution near the leading edge appear and larger values of the threshold parameter δ are required to remedy this issue. For sufficiently large values of the entropy fix, the solution computed using the Roe Riemann solver is in good agreement with the reference one. Such an accurate approximation is also achieved by the FCFV method using the HLLEM numerical flux, without the need of tuning any parameter.

Table 2.3 reports the values of the lift and drag coefficients, computed using different Riemann solvers. Reference data from several numerical studies based on various computational methods were collected by Bristeau et al. (1987), reporting

values of the lift coefficient in the range $[0.415, 0.483]$ and of the drag coefficient in the interval $[0.2430, 0.2868]$.

Table 2.3: Viscous laminar transonic flow over a NACA 0012 profile - Lift, C_l, and drag, C_d, coefficients computed using different Riemann solvers.

	Lax-Friedrichs	Roe ($\delta = 0.1$)	HLL	HLLEM
C_l	0.528	0.468	0.518	0.466
C_d	0.3215	0.2845	0.3135	0.2832

The excessive numerical dissipation introduced by the Lax-Friedrichs and HLL numerical fluxes leads to estimate of the lift and drag coefficients with errors beyond the acceptable accuracy. On the contrary, the FCFV method equipped with the HLLEM and the Roe (with appropriate entropy fix) Riemann solvers provides values of the lift and drag coefficients lying within the ranges of published values for this benchmark, showing acceptable levels of accuracy also for the simulation of viscous laminar flows.

2.4.3 Low Mach number flow over a cylinder

In this section, an incompressible flow over a 2D cylinder at angle of attack $\alpha = 0°$ is considered, both in the inviscid and viscous laminar case. The objective is to show the robustness of the proposed FCFV solver for compressible flows when low Mach number flows are considered, as studied by Wong et al. (2001) and Sevilla et al. (2013).

Unstructured meshes of triangular cells are considered for both the inviscid and the viscous simulations. On the one hand, for the inviscid case, the mesh is isotropically refined in the vicinity of the cylinder, for a total of $359,242$ cells, as displayed in figure 2.16(a). The far-field boundary is located at 50 chord units from the cylinder where inviscid wall boundary conditions are imposed. On the other hand, the refinement of the boundary layer and of the wake of the cylinder in the viscous simulation leads to a mesh of $654,194$ triangular cells, reported in figure 2.16(b). In this case, the far-field boundary is placed at 20 chord lengths from the obstacle and the surface of the cylinder is considered adiabatic.

The isolines of the Mach number distribution computed with the HLLEM Riemann solver for the inviscid flow are reported in figure 2.17 for different values of

(a) Inviscid flow   (b) Viscous flow
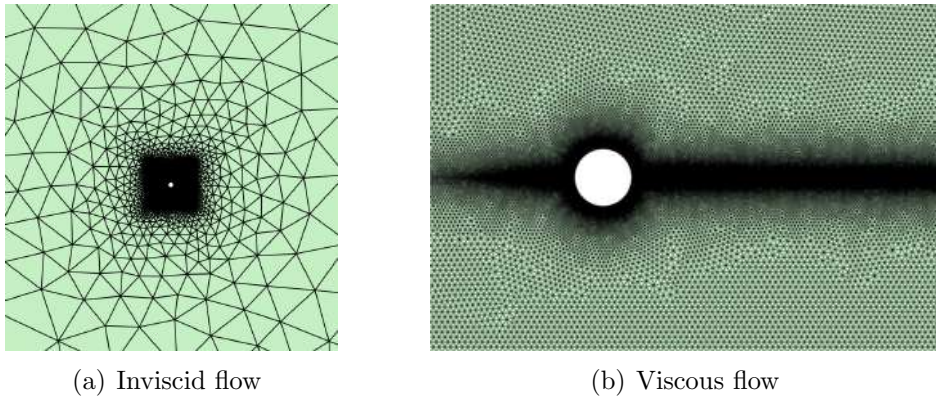
Figure 2.16: Meshes for the low Mach number flows over a cylinder in the inviscid and viscous case.

the far-field condition. The results display the robustness of the FCFV solver for low Mach number simulations, highlighting the capability of the method to devise non-oscillatory solutions even in the incompressible limit. More precisely, the computed solution is not deteriorated by the decrease of the Mach number, even when it approaches zero. Note that the loss of symmetry of the solution is due to the geometric error introduced by the piecewise linear approximation of the surface of the cylinder. This well-known problem, see Bassi and Rebay (1997b), is related to the production of nonphysical entropy by the low-order discretisation of the curved boundary. It is worth recalling that the objective of this test is to show the robustness of the proposed method in the incompressible limit. In order to remedy the above mentioned issue, several approaches proposed in the literature can be employed within the FCFV paradigm. These include high-order approximation of the geometry, by Bassi and Rebay (1997b), appropriate modification of the wall boundary condition, by Krivodonova and Berger (2006) or exact treatment of the geometry via the NURBS-enhanced finite element method, by Sevilla et al. (2008).

The robustness of the FCFV solver in the incompressible limit of the compressible Navier-Stokes equations is studied through a steady-state flow at $Re = 30$. Figure 2.18 displays the isolines of the Mach number distribution for far-field conditions at $M_\infty = 0.1$ and $M_\infty = 0.01$. In this case, the FCFV solver is able to precisely approximate the flow in the wake of the cylinder, with no loss of accuracy when approaching the incompressible limit. It is worth noticing that in both figure 2.17 and figure 2.18, the variation of the far-field boundary condition only affects the scale of the computed Mach number and not its distribution.

(a) $M_\infty = 0.1$ (b) $M_\infty = 0.01$
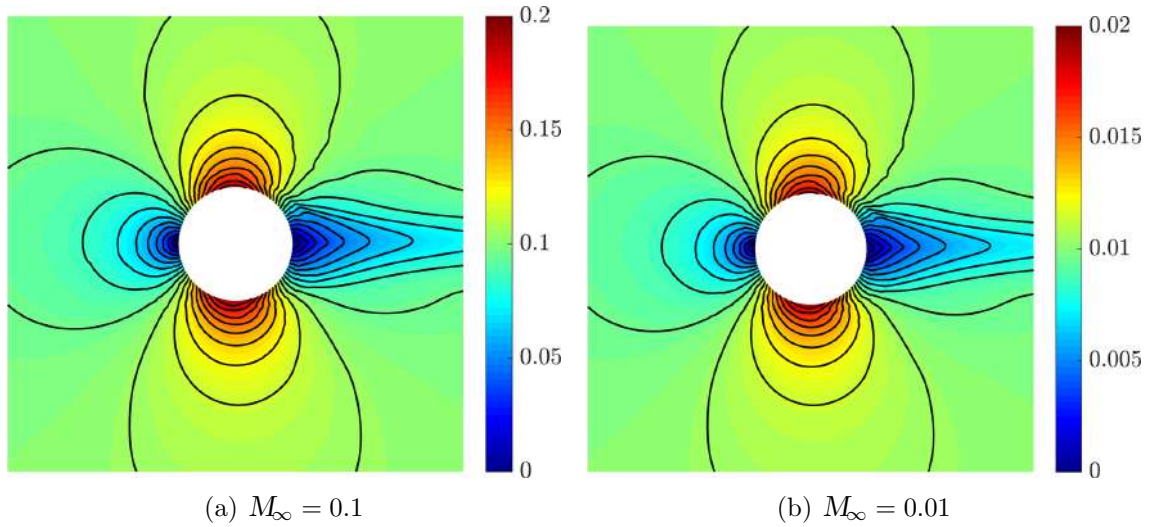
Figure 2.17: Inviscid subsonic flow over a cylinder - Mach number distribution computed using the HLLEM Riemann solver for different values of the far-field condition.

(a) $M_\infty = 0.1$ (b) $M_\infty = 0.01$
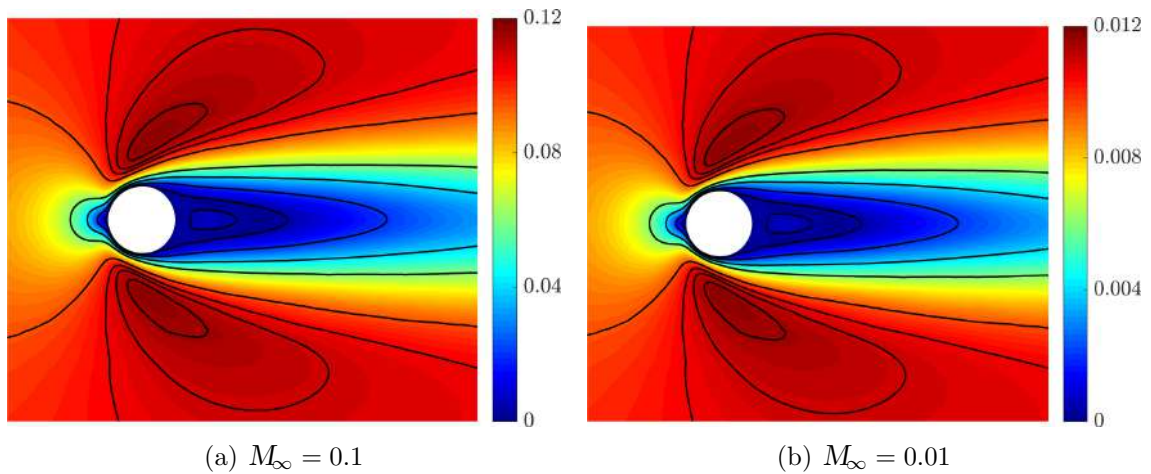
Figure 2.18: Viscous laminar subsonic flow over a cylinder at $Re = 30$ - Mach number distribution computed using the HLLEM Riemann solver for different values of the far-field condition.

The values of the pressure and skin friction coefficients computed using the HLLEM Riemann solver are compared with the results reported by Sevilla et al. (2013) of a stabilised finite element simulation performed with polynomial approximation of degree $k = 3$. Good agreement is displayed in figure 2.19 for both the pressure and the skin friction coefficients, confirming the capability the proposed methodology of accurately simulating viscous laminar flows also in the incompressible limit. In partic-

ular, it is worth noticing that the FCFV results computed using the two values of the far-field condition are almost identical and they are not affected by the value of the Mach number going to zero. Hence, the FCFV method equipped with the HLLEM

(a) Pressure coefficient   (b) Skin friction coefficient
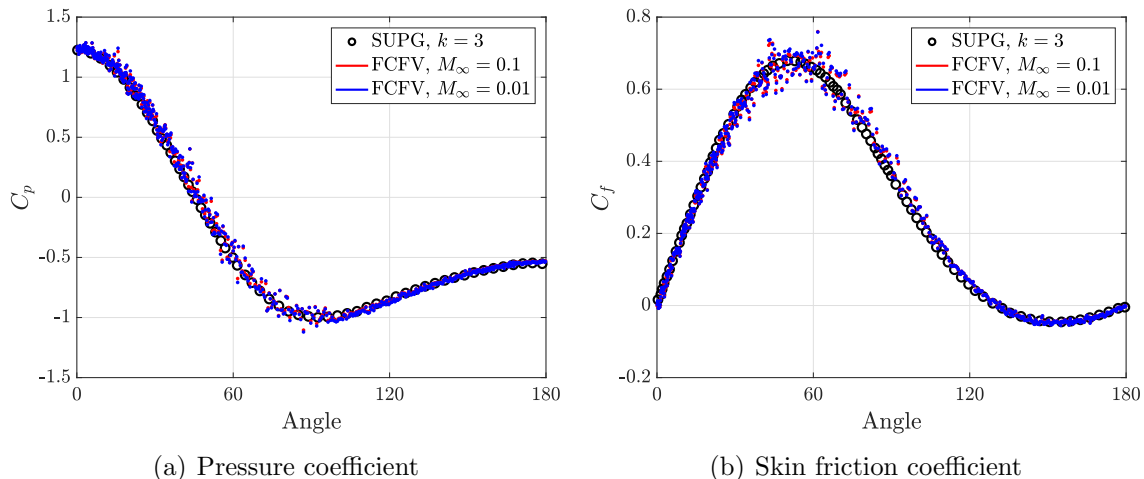
Figure 2.19: Viscous laminar subsonic flow over a cylinder at $Re = 30$ - (a) Pressure and (b) skin friction coefficient on the object surface computed using the HLLEM Riemann solver.

numerical flux provides a robust solver for steady-state compressible flows able to seamlessly handle both inviscid and viscous flows, at high and low Mach numbers.

Finally, it is worth mentioning that the pressure coefficient displayed in figure 2.19 has been computed employing the pressure evaluated at the hybrid state $\widehat{\boldsymbol{U}}$, defined over the boundary. Conversely, the skin friction coefficient is computed from the mixed variable defined inside the cell with constant value. In order to extend the constant values inside the cells to the boundary, a $\mathcal{C}^0$ smoothing based on computing an averaged mean on the mesh nodes based on the cell values can be performed. In this manner, both the pressure and skin friction coefficient can be computed over the cylinder boundary based on the corresponding nodal values obtained from such operation. In figure 2.20, the postprocessing option based on the hybrid and cell values is compared to the one based on the $\mathcal{C}^0$ smoothing. Accordingly, the pressure and skin friction coefficients computed for the case of $M_\infty = 0.1$ using an HLLEM Riemann solver are displayed, with the $k = 3$ results by Sevilla et al. (2013) as reference. The little oscillations displayed in those curves, specially in the skin friction coefficient, are drastically reduced by means of simple postprocess.

(a) Pressure coefficient

(b) Skin friction coefficient
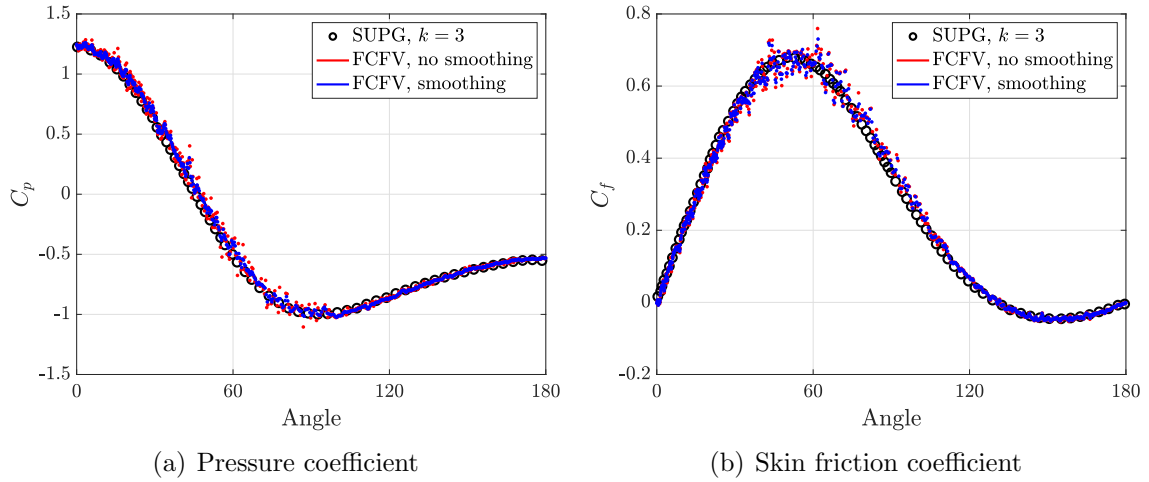
Figure 2.20: Viscous laminar subsonic flow over a cylinder at $Re = 30$ - (a) Pressure and (b) skin friction coefficient on the object surface computed using the HLLEM Riemann solver.

2.4.4 Inviscid transonic flow over an Onera M6 wing

The last example involves the 3D simulation of a steady inviscid transonic flow over an ONERA M6 wing at free-stream Mach number $M_\infty = 0.84$ and angle of attack $\alpha = 3.06°$. This benchmark constitutes a classic CFD validation example for external flows due to its complex flow physics and the availability of experimental results at high Reynolds number by Schmitt and Charpin (1979).

A non-uniform mesh refinement is adopted in the vicinity of the wing surface and towards the leading and trailing edges. Figure 2.21 details two levels of refinement with meshes consisting of 236,682 and 5,061,252 tetrahedral cells, respectively. The far-field boundary is located at approximately 12 chord lengths from the wing and the aerofoil surface is defined as an inviscid wall.

The FCFV simulation is performed using the HLL Riemann solver, based on its capability of producing positivity-conserving solutions and on its robustness in inviscid transonic and supersonic cases. The linear system of equations arising from the FCFV discretisation is solved using a GMRES with restarting parameter 10 and no preconditioner. A detail of the flow computation obtained on the fine mesh is reported in figure 2.22. The Mach number and pressure distributions clearly show that the FCFV method is able of accurately capturing the characteristic *lambda-shock* arising in this test benchmark.

The performance of the FCFV method is evaluated by examining the pressure

(a) Coarse mesh   (b) Fine mesh
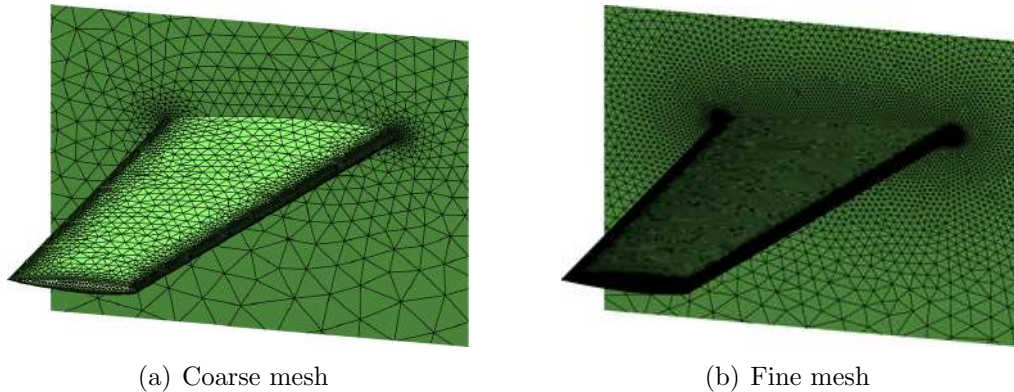
Figure 2.21: Mesh refinement for the inviscid transonic flow over an ONERA M6 wing.
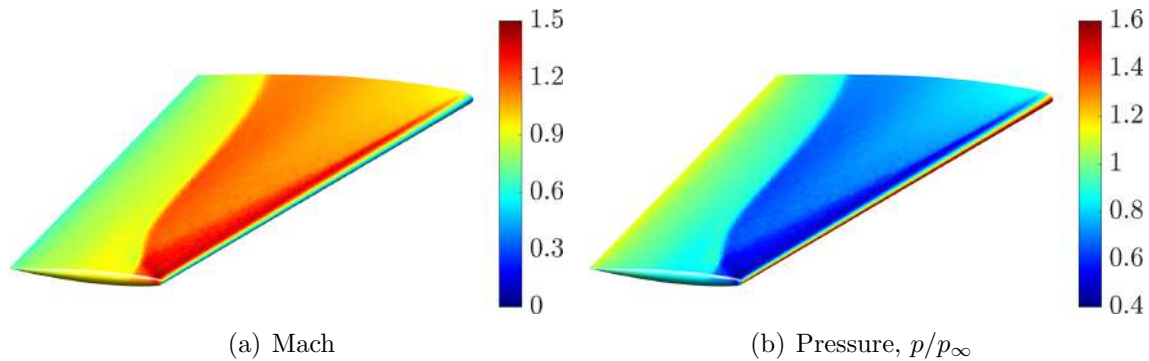
(a) Mach   (b) Pressure, p/p_∞

Figure 2.22: Inviscid transonic flow over an ONERA M6 wing - (a) Mach number and (b) pressure distributions on the wing surface computed on the fine mesh using the HLL Riemann solver.

coefficient, computed on the fine mesh, at different sections along the wing span, see figure 2.23. The obtained results are compared both to experimental data by Schmitt and Charpin (1979) and to computational simulations performed using second-order CCFV and VCFV solvers on the same mesh. More precisely, the commercial CFD software Ansys Fluent by ANSYS Inc. (2017) is employed as CCFV solver, whereas the VCFV results are obtained using the CFD solver FLITE, documented by Sørensen et al. (2003) and Hassan et al. (2008). An upwind scheme is utilised for the treatment of the numerical fluxes in Fluent, whereas a Roe Riemann solver is selected for the FLITE simulation. The numerical results obtained with the FCFV method show excellent agreement both with the experimental data and with the remaining FV schemes. It is worth noticing that both second-order FV schemes produce a small oscillation in the representation of the shock-wave located at the upper mid-chord. On the contrary, the first-order FCFV method based on the positivity-preserving
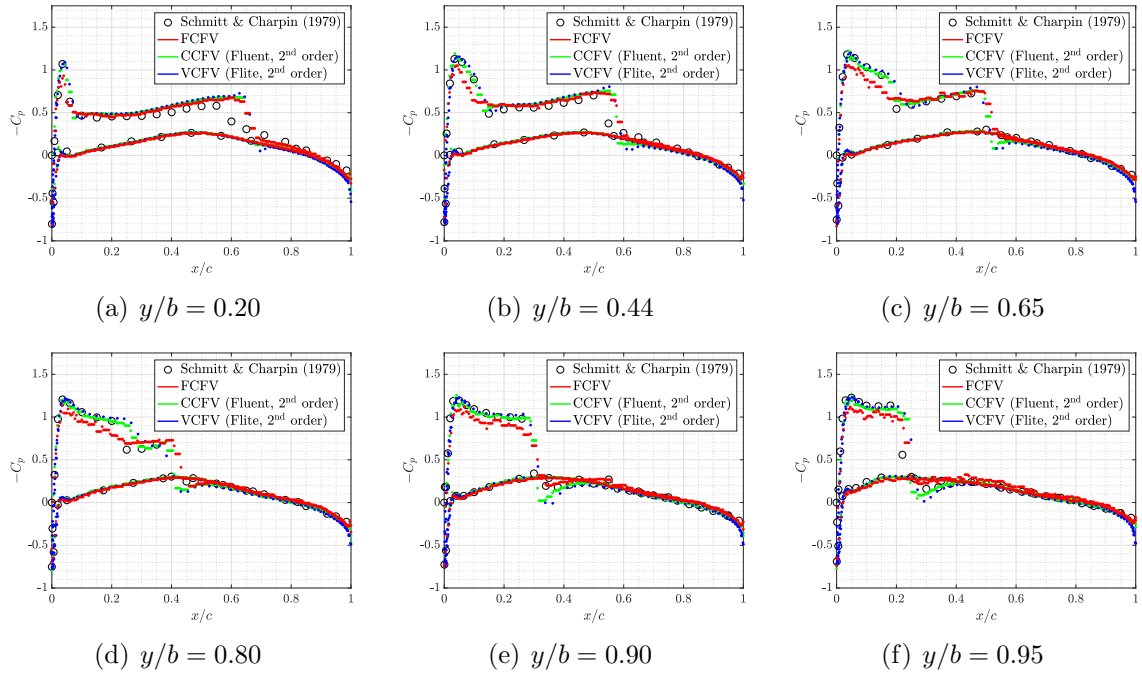
Figure 2.23: Inviscid transonic flow over an ONERA M6 wing - Comparison of the pressure coefficient distribution at different sections along the wing span using different FV solvers.

HLL Riemann solver is capable of computing non-oscillatory solutions, establishing a robust framework for the simulation of 3D problems involving complex flow features.

2.5 Conclusions

The face-centred finite volume (FCFV) paradigm was proposed for the first time for the approximation of nonlinear hyperbolic PDEs modelling compressible flows. The method is based on a mixed formulation and defines the unknowns, that is, the hybrid vector of conservative variables, at the barycentre of the faces. The unknowns in each cell, i.e. density, momentum, energy, deviatoric strain rate tensor and gradient of temperature, are eliminated via a hybridisation procedure to reduce the global number of degrees of freedom of the problem. In addition, traditional Riemann solvers, i.e. Lax-Friedrichs, Roe, HLL and HLLEM, are devised in the context of FCFV discretisations via appropriate definitions of the numerical fluxes.

The presented methodology achieves first-order accuracy of the conservative quantities, the stress tensor and the heat flux without the need to perform a reconstruction

of the gradients. Hence, the FCFV approximation is robust on unstructured meshes and retains optimal accuracy even with highly stretched or distorted cells, avoiding well-known issues of traditional FV schemes.

In addition, the FCFV method is able to construct non-oscillatory solutions of sharp fronts without the need of any shock capturing or limiting technique. The accurate treatment of shocks, expansion fans and shear waves is naturally handled by the Riemann solvers implicitly embedded in the FCFV numerical fluxes.

Finally, the method is robust in the incompressible limit, allowing to seamlessly simulate flows at low Mach number, without the need of introducing specific pressure corrections like the well-known SIMPLE algorithm.

A comprehensive set of two and three-dimensional numerical examples is employed to demonstrate the optimal convergence properties of the method and its capabilities to solve complex flow problems of aerodynamic interest across various regimes, from inviscid to viscous laminar flows, from transonic to subsonic incompressible flows. Moreover, a detailed comparison of the accuracy and robustness of different Riemann solvers is presented. The FCFV method equipped with HLL-type Riemann solvers thus provides a solution strategy suitable for all flow regimes, which outperforms the traditional Lax-Friedrichs numerical flux in terms of accuracy and the Roe solver in terms of robustness.

Chapter 3

Hybridisable discontinuous Galerkin formulation of compressible flows [1]

The high-order HDG formulation of compressible flows, including both the inviscid Euler and the viscous compressible Navier-Stokes equations, is reviewed in this chapter. The presented HDG formulation stems from the reference approach proposed by Peraire et al. (2010) and Nguyen and Peraire (2012) based on the mixed hybrid formulation of the compressible Navier-Stokes equations. The HDG approximation is characterised for the optimal accuracy properties not only of the conservation variables but also of the viscous stress and heat flux, which relies on an accurate choice of the approximation spaces and a proper definition of numerical fluxes.

To this end, this work introduces a novel mixed formulation of the compressible Navier-Stokes equations with strongly enforced symmetry of the viscous stress tensor. Such approach uses the same discrete spaces for the primal and mixed variables and retrieves optimal convergence properties of the stress tensor and the heat flux, with reduced computational cost. Last but foremost, this study proposes a unified framework for the derivation of Riemann solvers in hybridised formulations. The framework includes the existing Lax-Friedrichs and Roe solvers and formulates, for the first time in the context of HDG, the HLL and the HLLEM Riemann solvers. The HLL family

---

[1]This chapter is based on the published article Vila-Pérez et al. (2020)

of Riemann solvers provide a robust framework to compute reliable solutions of transonic and supersonic flows, based on their associated positivity-preserving properties. In addition, the HLLEM Riemann solver also displays shear preservation, providing increased accuracy in the approximation of contact waves or boundary layers.

The remainder of this section is organised as follows. Section 3.1 reviews the mixed formulation of the compressible Navier-stokes equations, which have been detailed in section 2.1. The high-order HDG formulation of the compressible Navier-Stokes equations is then introduced in sections 3.2 and 3.3. Furthermore, section 3.4 presents a unified description of the Riemann solvers in the context of high-order HDG methods. Specifically, the HLL and HLLEM Riemann solvers are proposed for hybrid discretisations. Finaly, in section 3.5, the solution strategy of the HDG solver for the resulting nonlinear problem and the numerical treatment of solutions with discontinuities and sharp gradients is discussed.

3.1   Mixed formulation of the compressible Navier-Stokes equations

One of the main features of the HDG method, as described in section 2.2.1 is the mixed formulation of second-order problems.

In the case of the compressible Navier-Stokes equations, the mixed variables are responsible for the description of the viscous stress tensor $\boldsymbol{\sigma}^d$ and the heat flux $\boldsymbol{q}$ appearing in the viscous fluxes (2.2).

Usual mixed formulations of the compressible Navier-Stokes equations introduce the gradient of the primal variable, $\boldsymbol{\nabla U}$, as mixed variable. This approach, initially employed by Peraire et al. (2010) and Nguyen and Peraire (2012) in HDG, has been well-established and has been adopted later by Woopen et al. (2014) or by Fernández et al. (2017), among others.

The advantage of using $\boldsymbol{\nabla U}$ is its linear expression with respect to the primal variable $\boldsymbol{U}$. Then, the system of equations (2.1) can be rewritten as a system of first-order PDEs with an additional linear equation, that is

$$\begin{cases} \boldsymbol{Q} - \boldsymbol{\nabla U} = \boldsymbol{0}, \\ \dfrac{\partial \boldsymbol{U}}{\partial t} + \boldsymbol{\nabla} \cdot (\boldsymbol{F}(\boldsymbol{U}) - \boldsymbol{G}(\boldsymbol{U}, \boldsymbol{Q})) = \boldsymbol{0}, \end{cases} \tag{3.1}$$

where the viscous stress tensor and the heat flux appearing in $\boldsymbol{G}(\boldsymbol{U}, \boldsymbol{Q})$ (2.2) are given by

$$\boldsymbol{\sigma}^d = \frac{1}{Re}\frac{\mu}{\rho}\left[\boldsymbol{\nabla}^{\mathsf{S}}(\rho\boldsymbol{v}) - \frac{1}{\rho}\left(\rho\boldsymbol{v}\otimes\boldsymbol{\nabla}\rho + \boldsymbol{\nabla}\rho\otimes\rho\boldsymbol{v}\right) - \frac{2}{3}\left(\boldsymbol{\nabla}\cdot(\rho\boldsymbol{v}) - \frac{1}{\rho}\boldsymbol{\nabla}\rho\cdot\rho\boldsymbol{v}\right)\mathbf{I}_{\mathsf{n_{sd}}}\right],$$
(3.2a)

$$\boldsymbol{q} = \frac{\gamma}{RePr}\frac{\mu}{\rho}\left[\boldsymbol{\nabla}(\rho E) - \frac{\rho E}{\rho}\boldsymbol{\nabla}\rho - \frac{1}{\rho}\left(\boldsymbol{\nabla}(\rho\boldsymbol{v})^T - \frac{1}{\rho}\boldsymbol{\nabla}\rho\otimes\rho\boldsymbol{v}\right)\rho\boldsymbol{v}\right].$$
(3.2b)

It is worth noticing that the viscous stresses and the heat flux are linear with respect to the mixed variable. However, their expression presents a number of nonlinearities with respect to the conservation variables.

An alternative formulation, introduced in section 2.2.1 for the FCFV method, inspired by the mechanical description of the problem, employs the deviatoric strain rate tensor

$$\boldsymbol{\varepsilon}^d = 2\boldsymbol{\nabla}^{\mathsf{S}}\boldsymbol{v} - \frac{2}{3}(\boldsymbol{\nabla}\cdot\boldsymbol{v})\mathbf{I}_{\mathsf{n_{sd}}} = \mathcal{D}\boldsymbol{\nabla}^{\mathsf{S}}\boldsymbol{v},$$
(3.3)

and the gradient of temperature $\boldsymbol{\phi} = \boldsymbol{\nabla}T$ as mixed variables for the mixed formulation, being $\mathcal{D}$ the linear operator introduced in remark 2.4. The resulting system of first-order PDEs is given by

$$\begin{cases} \boldsymbol{\varepsilon}^d - \mathcal{D}\boldsymbol{\nabla}^{\mathsf{S}}\boldsymbol{v} = \boldsymbol{0}, \\ \boldsymbol{\phi} - \boldsymbol{\nabla}T = \boldsymbol{0}, \\ \dfrac{\partial\boldsymbol{U}}{\partial t} + \boldsymbol{\nabla}\cdot\left(\boldsymbol{F}(\boldsymbol{U}) - \boldsymbol{G}(\boldsymbol{U}, \boldsymbol{\varepsilon}^d, \boldsymbol{\phi})\right) = \boldsymbol{0}, \end{cases}$$
(3.4)

where the viscous stress tensor and the heat flux in $\boldsymbol{G}(\boldsymbol{U}, \boldsymbol{\varepsilon}^d, \boldsymbol{\phi})$ (2.2) can be expressed in a neat manner as

$$\boldsymbol{\sigma}^d = \frac{\mu}{Re}\boldsymbol{\varepsilon}^d, \qquad \boldsymbol{q} = \frac{\mu}{RePr}\boldsymbol{\phi}.$$
(3.5)

Note that, whereas such mixed variables are nonlinear with respect to the conservation variables, this choice vastly reduces the number of nonlinearities and simplifies the expression of the viscous fluxes, in contrast to (3.2).

Remark 3.1. Such choice for the mixed variables, which resembles the mixed formulation proposed by Williams (2018), involves a reduced number of degrees of freedom, when compared to $\boldsymbol{Q} = \boldsymbol{\nabla}\boldsymbol{U}$, thus decreasing the computational cost of the local problems.

3.2 Strong form of the local and global problems

In the present formulation, the deviatoric strain rate tensor $\boldsymbol{\varepsilon}^d$ and the temperature gradient $\boldsymbol{\phi}$ are adopted as mixed variables, following the same approach described in section 2.2.2 for the FCFV formulation. The strong mixed form of the local and global problems is then recalled.

First, the $\mathtt{n}_{\mathtt{el}}$ local problems, given by

$$
\begin{cases}
\boldsymbol{\varepsilon}_e^d - \mathcal{D}\boldsymbol{\nabla}^{\mathrm{S}}\boldsymbol{v}_e = \mathbf{0} & \text{in } \Omega_e \times (0, \mathrm{T_{end}}], \\
\boldsymbol{\phi}_e - \boldsymbol{\nabla}T_e = \mathbf{0} & \text{in } \Omega_e \times (0, \mathrm{T_{end}}], \\
\dfrac{\partial \boldsymbol{U}_e}{\partial t} + \boldsymbol{\nabla} \cdot \big(\boldsymbol{F}(\boldsymbol{U}_e) - \boldsymbol{G}(\boldsymbol{U}_e, \boldsymbol{\varepsilon}_e^d, \boldsymbol{\phi}_e)\big) = \mathbf{0} & \text{in } \Omega_e \times (0, \mathrm{T_{end}}], \\
\boldsymbol{U}_e = \boldsymbol{U}^0 & \text{in } \Omega_e \times \{0\}, \\
\boldsymbol{U}_e = \widehat{\boldsymbol{U}} & \text{on } \partial\Omega_e \times (0, \mathrm{T_{end}}],
\end{cases}
\tag{3.6}
$$

for $e = 1, \ldots, \mathtt{n}_{\mathtt{el}}$, define the solution $(\boldsymbol{U}_e, \boldsymbol{\varepsilon}_e^d, \boldsymbol{\phi}_e) = (\boldsymbol{U}, \boldsymbol{\varepsilon}^d, \boldsymbol{\phi})$ for all $\boldsymbol{x} \in \Omega_e \subset \Omega$ as a function of an independent variable $\widehat{\boldsymbol{U}}$, representing the trace of the solution on $\Gamma \cup \partial\Omega$.

Then, $\widehat{\boldsymbol{U}}$ is computed as the solution of a global problem imposing boundary conditions on $\partial\Omega$ and enforcing inter-element continuity of the solution and of the normal fluxes on Γ via the so-called *transmission conditions*, namely

$$
\begin{cases}
\widehat{\boldsymbol{B}}(\boldsymbol{U}, \widehat{\boldsymbol{U}}, \boldsymbol{\varepsilon}^d, \boldsymbol{\phi}) = \mathbf{0}, & \text{on } \partial\Omega \times (0, \mathrm{T_{end}}], \\
[\![\boldsymbol{U} \otimes \boldsymbol{n}]\!] = \mathbf{0} & \text{on } \Gamma \times (0, \mathrm{T_{end}}], \\
[\![\big(\boldsymbol{F}(\boldsymbol{U}) - \boldsymbol{G}(\boldsymbol{U}, \boldsymbol{\varepsilon}^d, \boldsymbol{\phi})\big)\boldsymbol{n}]\!] = \mathbf{0} & \text{on } \Gamma \times (0, \mathrm{T_{end}}],
\end{cases}
\tag{3.7}
$$

where $\boldsymbol{n}$ is the outward unit normal vector and $\widehat{\boldsymbol{B}}(\boldsymbol{U}, \widehat{\boldsymbol{U}}, \boldsymbol{\varepsilon}^d, \boldsymbol{\phi})$ is a boundary trace operator imposing the boundary conditions along $\partial\Omega$ exploiting the hybrid variable, as described in section 2.2.3. In particular, the expression of the boundary operator for the most common boundary conditions arising in compressible flows are detailed in table 2.1.

Note that the second equation in (3.7) is automatically satisfied due to the Dirichlet boundary condition $\boldsymbol{U}_e = \widehat{\boldsymbol{U}}$ imposed in the local problems (3.6) and by the fact that the hybrid variable $\widehat{\boldsymbol{U}}$ is unique on each face of the mesh skeleton.

3.3 Weak form of the local and global problems

Following the notation employed by Sevilla and Huerta (2016) and Giacomini et al. (2020), the following discrete functional spaces

$$\mathcal{W}^h(\Omega) := \left\{ w \in \mathcal{L}_2(\Omega) : w|_{\Omega_e} \in \mathcal{P}^k(\Omega_e) \; \forall \Omega_e, \; e = 1, \dots, \mathtt{n_{el}} \right\}, \qquad (3.8a)$$

$$\widehat{\mathcal{W}}^h(S) := \left\{ \widehat{w} \in \mathcal{L}_2(S) : \widehat{w}|_{\Gamma_i} \in \mathcal{P}^k(\Gamma_i) \; \forall \Gamma_i \subset S \subseteq \Gamma \cup \partial\Omega \right\}, \qquad (3.8b)$$

are introduced, where $\mathcal{P}^k(\Omega_e)$ and $\mathcal{P}^k(\Gamma_i)$ denote the spaces of polynomial functions of complete degree at most k in Ω_e and on Γ_i, respectively. Moreover, let

$$\mathcal{W}_t^h(\Omega) := \mathcal{L}_2 \left((0, \mathrm{T_{end}}]; \mathcal{W}^h(\Omega) \right), \qquad (3.9a)$$

$$\widehat{\mathcal{W}}_t^h(S) := \mathcal{L}_2 \left((0, \mathrm{T_{end}}]; \widehat{\mathcal{W}}^h(S) \right), \qquad (3.9b)$$

denote the spaces of square-integrable functions on the time interval $(0, \mathrm{T_{end}}]$ with spatial approximation in $\mathcal{W}^h(\Omega)$ and $\widehat{\mathcal{W}}^h(S)$, respectively.

Henceforth, the classical notation for $\mathcal{L}_2$ inner products of vector and tensor-valued functions on a generic subdomain $D \subset \Omega$ is considered, that is

$$(\boldsymbol{v}, \boldsymbol{w})_D := \int_D \boldsymbol{v} \cdot \boldsymbol{w} \; d\Omega \quad \text{and} \quad (\boldsymbol{V}, \boldsymbol{W})_D := \int_D \boldsymbol{V} : \boldsymbol{W} \; d\Omega. \qquad (3.10)$$

Analogously, the $\mathcal{L}_2$ inner products on a surface $S \subset \Gamma \cup \partial\Omega$ are denoted by $\langle \cdot, \cdot \rangle_S$.

Remark 3.2. It is worth noticing that the mixed variable $\boldsymbol{\varepsilon}^d$ requires the definition of an appropriate functional space. In particular, $\boldsymbol{\varepsilon}^d \in [\mathcal{H}(\mathrm{div}; D); \mathbb{S}]$, $D \subseteq \Omega$, that is, the space of $\mathcal{L}_2(D)$ symmetric tensors $\mathbb{S}$ of order $\mathtt{n_{sd}}$ with $\mathcal{L}_2(D)$ row-wise divergence. Accordingly, its element-by-element approximation $\boldsymbol{\varepsilon}_e^d$ must be defined in an appropriate discrete space for symmetric second-order tensors of dimension $\mathtt{n_{sd}} \times \mathtt{n_{sd}}$. Several approaches have been proposed in the literature, see for instance the studies by Cockburn and Shi (2012), Cockburn and Fu (2017) or Qiu et al. (2017). In this work, Voigt notation, introduced by Fish and Belytschko (2007), is exploited to rearrange the diagonal and off-diagonal components of the tensor into an $\mathtt{m_{sd}}$-dimensional vector, being $\mathtt{m_{sd}} = \mathtt{n_{sd}}(\mathtt{n_{sd}} + 1)/2$ the number of non-redundant terms. This allows a simple construction of a pointwise symmetric mixed variable with reduced computational cost, while retrieving optimal convergence of the approximation, see the

studies by Giacomini et al. (2018) and Sevilla et al. (2018) for Stokes flows and linear elasticity, respectively. For a detailed derivation of such approach, interested readers are referred to the tutorial by Giacomini et al. (2020).

With the introduced notation, the discrete weak form associated to the local problems (3.6) is: for every element Ω_e, $e = 1, \ldots, \mathtt{n_{el}}$, find an approximation $(\boldsymbol{U}_e, \boldsymbol{\varepsilon}_e^d, \boldsymbol{\phi}_e) \in [\mathcal{W}_t^h(\Omega_e)]^{\mathtt{n_{sd}}+2} \times [\mathcal{W}_t^h(\Omega_e)]^{\mathtt{m_{sd}}} \times [\mathcal{W}_t^h(\Omega_e)]^{\mathtt{n_{sd}}}$, given $\widehat{\boldsymbol{U}} \in [\widehat{\mathcal{W}}_t^h(\Gamma \cup \partial\Omega)]^{\mathtt{n_{sd}}+2}$, such that

$$\left(\boldsymbol{\zeta}, \boldsymbol{\varepsilon}_e^d\right)_{\Omega_e} + (\boldsymbol{\nabla} \cdot \mathcal{D}\boldsymbol{\zeta}, \boldsymbol{v}_e)_{\Omega_e} - \left\langle \boldsymbol{\zeta}, \mathcal{D}\widehat{\boldsymbol{v}} \otimes \boldsymbol{n} \right\rangle_{\partial\Omega_e} = 0, \tag{3.11a}$$

$$\left(\boldsymbol{\xi}, \boldsymbol{\phi}_e\right)_{\Omega_e} + (\boldsymbol{\nabla} \cdot \boldsymbol{\xi}, T_e)_{\Omega_e} - \left\langle \boldsymbol{\xi}, \widehat{T}\boldsymbol{n} \right\rangle_{\partial\Omega_e} = 0, \tag{3.11b}$$

$$\left(\boldsymbol{W}, \frac{\partial \boldsymbol{U}_e}{\partial t}\right)_{\Omega_e} - (\boldsymbol{\nabla}\boldsymbol{W}, \boldsymbol{F} - \boldsymbol{G})_{\Omega_e} + \left\langle \boldsymbol{W}, \overline{\left(\boldsymbol{F}(\boldsymbol{U}_e) - \boldsymbol{G}(\boldsymbol{U}_e, \boldsymbol{\varepsilon}_e^d, \boldsymbol{\phi}_e)\right)\boldsymbol{n}} \right\rangle_{\partial\Omega_e} = 0, \tag{3.11c}$$

for all $(\boldsymbol{W}, \boldsymbol{\zeta}, \boldsymbol{\xi}) \in [\mathcal{W}_t^h(\Omega_e)]^{\mathtt{n_{sd}}+2} \times [\mathcal{W}_t^h(\Omega_e)]^{\mathtt{m_{sd}}} \times [\mathcal{W}_t^h(\Omega_e)]^{\mathtt{n_{sd}}}$.

Remark 3.3. Note that, rigorously, equation (3.11a) should be derived under the assumption that $\boldsymbol{\varepsilon}^d$ belongs to the functional space $[\mathcal{H}(\text{div}; D); \mathbb{S}]$. Nonetheless, in an abuse of notation, $\boldsymbol{\varepsilon}^d$ has been substituted by its discrete counterpart $\boldsymbol{\varepsilon}_e^d \in [\mathcal{W}_t^h(\Omega_e)]^{\mathtt{m_{sd}}}$, expressed in Voigt notation. For further details on the functional spaces and the derivation of the discrete forms, interested readers are referred to Giacomini et al. (2020). In addition, technical details about the implementation the corresponding equation are given in appendix A.

Similarly, the discrete weak formulation of the global problem in equation (3.7) is: find $\widehat{\boldsymbol{U}} \in [\widehat{\mathcal{W}}_t^h(\Gamma \cup \partial\Omega)]^{\mathtt{n_{sd}}+2}$ such that

$$\sum_{e=1}^{\mathtt{n_{el}}} \left\{ \left\langle \widehat{\boldsymbol{W}}, \overline{\left(\boldsymbol{F}(\boldsymbol{U}_e) - \boldsymbol{G}(\boldsymbol{U}_e, \boldsymbol{\varepsilon}_e^d, \boldsymbol{\phi}_e)\right)\boldsymbol{n}} \right\rangle_{\partial\Omega_e \cap \Gamma} + \left\langle \widehat{\boldsymbol{W}}, \widehat{\boldsymbol{B}} \right\rangle_{\partial\Omega_e \cap \partial\Omega} \right\} = 0, \tag{3.12}$$

for all $\widehat{\boldsymbol{W}} \in [\widehat{\mathcal{W}}_t^h(\Gamma \cup \partial\Omega)]^{\mathtt{n_{sd}}+2}$.

Equations (3.11c) and (3.12) introduce the traces of the numerical fluxes on the boundary,

$$\overline{\left(\boldsymbol{F}(\boldsymbol{U}_e) - \boldsymbol{G}(\boldsymbol{U}_e, \boldsymbol{\varepsilon}_e^d, \boldsymbol{\phi}_e)\right)\boldsymbol{n}} = \overline{\boldsymbol{F}(\boldsymbol{U}_e)\boldsymbol{n}} - \overline{\boldsymbol{G}(\boldsymbol{U}_e, \boldsymbol{\varepsilon}_e^d, \boldsymbol{\phi}_e)\boldsymbol{n}}, \tag{3.13}$$

where

$$\overline{\boldsymbol{F}(\boldsymbol{U}_e)\boldsymbol{n}} := \boldsymbol{F}(\widehat{\boldsymbol{U}})\boldsymbol{n} + \boldsymbol{\tau}^a(\widehat{\boldsymbol{U}})(\boldsymbol{U}_e - \widehat{\boldsymbol{U}}) \quad \text{and} \tag{3.14a}$$

$$\widehat{\boldsymbol{G}(\boldsymbol{U}_e, \boldsymbol{\varepsilon}_e^d, \boldsymbol{\phi}_e)\boldsymbol{n}} := \boldsymbol{G}(\widehat{\boldsymbol{U}}, \boldsymbol{\varepsilon}_e^d, \boldsymbol{\phi}_e)\boldsymbol{n} - \boldsymbol{\tau}^d(\boldsymbol{U}_e - \widehat{\boldsymbol{U}}) \tag{3.14b}$$

stand for the convective and the diffusive numerical fluxes, respectively, whose approximation is essential for the quality and accuracy of the HDG method.

On the one hand, the diffusive numerical fluxes, $\widehat{\boldsymbol{G}(\boldsymbol{U}_e, \boldsymbol{\varepsilon}_e^d, \boldsymbol{\phi}_e)\boldsymbol{n}}$, involve the diffusive stabilisation term $\boldsymbol{\tau}^d$, selected as the diagonal matrix

$$\boldsymbol{\tau}^d = Re^{-1} \operatorname{diag}\left(0, \mathbf{1}_{\mathtt{n_{sd}}}, \left[(\gamma - 1)M_\infty^2 Pr\right]^{-1}\right), \tag{3.15}$$

being $\mathbf{1}_{\mathtt{n_{sd}}}$ an $\mathtt{n_{sd}}$-dimensional vector of ones. This approach follows the philosophy by Peraire et al. (2011) and Nguyen and Peraire (2012) owing to dimensional consistency but considers different amounts of diffusive stabilisation for each of the three conservation equations, i.e., mass, momentum and energy. In particular, note that the continuity equation, which has a purely convective nature, does not include any diffusive stabilisation.

It is worth noting that the term $\boldsymbol{G}(\widehat{\boldsymbol{U}}, \boldsymbol{\varepsilon}_e^d, \boldsymbol{\phi}_e)\boldsymbol{n}$ containing the physical flux in (3.14b) can be approximated either using the interior state $\boldsymbol{U}_e$ or the trace of the primal variable $\widehat{\boldsymbol{U}}$. In this work, the latter has been chosen, following the classical formulation in hybridised DG methods proposed by Peraire et al. (2010) Peraire et al. (2011) or Nguyen and Peraire (2012), which exploits the presence of an intermediate state, namely the trace of the conservation variables, $\widehat{\boldsymbol{U}}$.

Remark 3.4. Note that in the incompressible limit and using the current choice for mixed variables, both alternatives, $\boldsymbol{G}(\widehat{\boldsymbol{U}}, \boldsymbol{\varepsilon}_e^d, \boldsymbol{\phi}_e)\boldsymbol{n}$ and $\boldsymbol{G}(\boldsymbol{U}_e, \boldsymbol{\varepsilon}^d, \boldsymbol{\phi})\boldsymbol{n}$, lead to the same numerical flux. Indeed, the energy equation for which the tensor $\boldsymbol{G}$ depends on the conserved variables $\boldsymbol{U}$, is decoupled from the system of conservation equations.

On the other hand, the convective numerical fluxes, $\widehat{\boldsymbol{F}(\boldsymbol{U})\boldsymbol{n}}$, are approximated using Riemann solvers, whose utilisation in FV —hence, in DG methods— has been reviewed in detail by Toro (2009). In particular, some of the most relevant approximate Riemann solvers employed in these numerical schemes, specifically the Lax-Friedrichs, Roe, HLL and HLLEM solvers, are described in appendix B.

The corresponding definition of such convective fluxes for hybridised methods is detailed in section 3.4. Indeed, a unified framework for the derivation of Riemann solvers in the context of hybridised methods is presented, including the newly proposed HLL and HLLEM Riemann solvers.

Remark 3.5 (Compressible Euler equations)**.** The associated weak forms for the inviscid Euler equations reduce to:

Local problems: given $\widehat{\boldsymbol{U}} \in [\widehat{\mathcal{W}}_t^h(\Gamma \cup \partial\Omega)]^{\mathtt{n_{sd}}+2}$ and for every element Ω_e, $e = 1, \dots, \mathtt{n_{el}}$, find $\boldsymbol{U}_e \in [\mathcal{W}_t^h(\Omega_e)]^{\mathtt{n_{sd}}+2}$ such that, for all $\boldsymbol{W} \in [\mathcal{W}_t^h(\Omega_e)]^{\mathtt{n_{sd}}+2}$,

$$\left(\boldsymbol{W}, \frac{\partial \boldsymbol{U}_e}{\partial t}\right)_{\Omega_e} - (\boldsymbol{\nabla}\boldsymbol{W}, \boldsymbol{F}(\boldsymbol{U}_e))_{\Omega_e} + \left\langle \boldsymbol{W}, \widehat{\boldsymbol{F}(\boldsymbol{U}_e)\boldsymbol{n}} \right\rangle_{\partial\Omega_e} = 0. \tag{3.16}$$

Global problem: for all $\widehat{\boldsymbol{W}} \in [\widehat{\mathcal{W}}_t^h(\Gamma \cup \partial\Omega)]^{\mathtt{n_{sd}}+2}$, find $\widehat{\boldsymbol{U}} \in [\widehat{\mathcal{W}}_t^h(\Gamma \cup \partial\Omega)]^{\mathtt{n_{sd}}+2}$ such that

$$\sum_{e=1}^{\mathtt{n_{el}}} \left\{ \left\langle \widehat{\boldsymbol{W}}, \widehat{\boldsymbol{F}(\boldsymbol{U}_e)\boldsymbol{n}} \right\rangle_{\partial\Omega_e \cap \Gamma} + \left\langle \widehat{\boldsymbol{W}}, \widehat{\boldsymbol{B}} \right\rangle_{\partial\Omega_e \cap \partial\Omega} \right\} = 0. \tag{3.17}$$

3.4   A unified framework for the derivation of Riemann solvers in hybridised DG methods

As mentioned above, the choice of the convective numerical fluxes $\widehat{\boldsymbol{F}(\boldsymbol{U}_e)\boldsymbol{n}}$ appearing in equations (3.11c) and (3.12) —or in equations (3.16) and (3.17) for the Euler equations— has a critical influence on the accuracy and stability of the numerical solution. More precisely, such numerical fluxes are responsible for encapsulating the information of the convective nature of the flow under analysis. For this reason, the approximation of such interface fluxes has received great attention in the context of discontinuous Galerkin methods, as described in appendix B, and, more recently, of HDG by means of Riemann solvers.

In this section, a unified framework for the formulation of approximate Riemann solvers in the context of the hybridised methods is proposed. The framework includes, for the first time, the formulation of the HLL and HLLEM Riemann solvers within hybridised formulations for compressible flows. This derivation stems from the seminal work in HDG on linear and nonlinear convection-diffusion equations by Nguyen et al. (2009a,b) and on compressible flows by Peraire et al. (2010, 2011) and Nguyen and Peraire (2012). The topic has also been studied by Bui-Thanh (2015).

As described before, the general structure of the trace of the convective numerical flux for a nonlinear problem is given by

$$\widehat{\boldsymbol{F}(\boldsymbol{U}_e)\boldsymbol{n}} = \boldsymbol{F}(\widehat{\boldsymbol{U}})\boldsymbol{n} + \boldsymbol{\tau}^a(\widehat{\boldsymbol{U}})(\boldsymbol{U}_e - \widehat{\boldsymbol{U}}), \tag{3.18}$$

where $\boldsymbol{\tau}^a$ is the convective stabilisation matrix which encapsulates the information of the Riemann solvers. In order to ease readability, the superindex in $\boldsymbol{\tau}^a$ to denote the convective stabilisation term will be dropped in the upcoming derivations along this section.

To this end, consider a pair of neighbouring elements, Ω_e^+ and Ω_e^-, with shared interface $\Gamma_i = \partial\Omega_e^+ \cap \partial\Omega_e^- \subset \Gamma$. The solution at each side of the interface is denoted by $\boldsymbol{U}_e^\pm$, whereas $\boldsymbol{U}^\star(\boldsymbol{U}_e^+, \boldsymbol{U}_e^-)$ represents an intermediate state between $\boldsymbol{U}_e^+$ and $\boldsymbol{U}_e^-$.

It is worth noting that in (3.18) the hybrid variable $\widehat{\boldsymbol{U}}$ defined on the interface Γ_i between two neighboring elements Ω_e^+ and Ω_e^- is utilised as the intermediate state $\boldsymbol{U}^\star$.

In order to derive the formulation of the Riemann solvers in the context of hybridised DG methods, the inter-element continuity of the trace of the numerical fluxes is considered in the convective limit, namely $[\![\widehat{\boldsymbol{F}(\boldsymbol{U}_e)\boldsymbol{n}}]\!] = \boldsymbol{0}$. It follows that the sum of the contributions $\widehat{\boldsymbol{F}(\boldsymbol{U}_e)\boldsymbol{n}}$ from two neighbouring elements is set to zero. Exploiting definition (3.18) and observing that $[\![\boldsymbol{F}(\widehat{\boldsymbol{U}})\boldsymbol{n}]\!] = \boldsymbol{0}$ because of the uniqueness of $\widehat{\boldsymbol{U}}$ on the internal faces, the above transmission condition reduces to

$$(\boldsymbol{\tau}^+ + \boldsymbol{\tau}^-)\widehat{\boldsymbol{U}} = \boldsymbol{\tau}^+\boldsymbol{U}_e^+ + \boldsymbol{\tau}^-\boldsymbol{U}_e^-, \tag{3.19}$$

where $\boldsymbol{\tau}^+$ and $\boldsymbol{\tau}^-$ denote stabilisation matrices seen from element Ω^+ and Ω^-, respectively. Under the assumption of $(\boldsymbol{\tau}^+ + \boldsymbol{\tau}^-)$ being invertible, the intermediate state $\widehat{\boldsymbol{U}}$ is determined as

$$\widehat{\boldsymbol{U}} = (\boldsymbol{\tau}^+ + \boldsymbol{\tau}^-)^{-1}\left[\boldsymbol{\tau}^+\boldsymbol{U}_e^+ + \boldsymbol{\tau}^-\boldsymbol{U}_e^-\right]. \tag{3.20}$$

Hence, the convective numerical flux (3.18) is formulated as an explicit function of the left and right states $\boldsymbol{U}_e^\pm$.

From the framework above, two cases are analysed hereafter. On the one hand, a stabilisation matrix continuous across the interface is obtained by setting $\boldsymbol{\tau}^+ = \boldsymbol{\tau}^-$. On the other hand, a stabilisation matrix, discontinuous across the interface, is considered when $\boldsymbol{\tau}^+ \neq \boldsymbol{\tau}^-$.

3.4.1 Continuous stabilisation across the interface: Lax-Friedrichs and Roe Riemann solvers

Consider a continuous definition of the stabilisation matrix across the interface, that is $\boldsymbol{\tau}^+ = \boldsymbol{\tau}^- = \overline{\boldsymbol{\tau}}$. It follows

$$\widehat{\boldsymbol{U}} = \frac{\boldsymbol{U}_e^+ + \boldsymbol{U}_e^-}{2}, \tag{3.21a}$$

$$\widehat{\boldsymbol{F}(\boldsymbol{U}_e)\boldsymbol{n}^\pm} = \boldsymbol{F}\left(\frac{\boldsymbol{U}_e^+ + \boldsymbol{U}_e^-}{2}\right)\boldsymbol{n}^\pm + \frac{1}{2}\overline{\boldsymbol{\tau}}(\boldsymbol{U}_e^\pm - \boldsymbol{U}_e^\mp). \tag{3.21b}$$

By considering $\widehat{\boldsymbol{U}}$ as an intermediate state between $\boldsymbol{U}^+$ and $\boldsymbol{U}^-$ and under appropriate choices of the stabilisation matrix $\overline{\boldsymbol{\tau}}$, a formulation that mimics Lax-Friedrichs and Roe Riemann solvers for traditional FV and DG methods, see (B.1) and (B.2), is retrieved for hybridised formulations, as proposed by Peraire et al. (2010, 2011) and Nguyen and Peraire (2012).

More precisely, the Lax-Friedrichs numerical flux is retrieved by setting $\overline{\boldsymbol{\tau}} = \widehat{\lambda}_{\mathtt{max}}\mathbf{I}_{\mathtt{n_{sd}}+2}$, with $\widehat{\lambda}_{\mathtt{max}} := |\widehat{\boldsymbol{v}} \cdot \boldsymbol{n}| + \widehat{c}$, namely

$$\widehat{\boldsymbol{F}(\boldsymbol{U}_e)\boldsymbol{n}} = \boldsymbol{F}(\widehat{\boldsymbol{U}})\boldsymbol{n} + \widehat{\lambda}_{\mathtt{max}}(\boldsymbol{U}_e - \widehat{\boldsymbol{U}}). \tag{3.22}$$

Similarly, the stabilisation matrix $\overline{\boldsymbol{\tau}} = |\boldsymbol{A}_n(\widehat{\boldsymbol{U}})| = \mathbf{R}|\boldsymbol{\Lambda}|\mathbf{L}$ evaluated at the intermediate state (3.21a) lead to the formulation of the Roe Riemann solver in the context of HDG methods, that is,

$$\widehat{\boldsymbol{F}(\boldsymbol{U}_e)\boldsymbol{n}} = \boldsymbol{F}(\widehat{\boldsymbol{U}})\boldsymbol{n} + |\boldsymbol{A}_n(\widehat{\boldsymbol{U}})|(\boldsymbol{U}_e - \widehat{\boldsymbol{U}}). \tag{3.23}$$

Finally, the variant of the Roe numerical flux accounting for the entropy fix by Harten and Hyman (1983) is given by $\overline{\boldsymbol{\tau}} = |\boldsymbol{A}_n^\delta(\widehat{\boldsymbol{U}})| = \boldsymbol{R}\boldsymbol{\Phi}\boldsymbol{L}$, according to the correction to matrix $\boldsymbol{A}_n(\widehat{\boldsymbol{U}})$ described in (B.3), that is

$$\widehat{\boldsymbol{F}(\boldsymbol{U}_e)\boldsymbol{n}} = \boldsymbol{F}(\widehat{\boldsymbol{U}})\boldsymbol{n} + |\boldsymbol{A}_n^\delta(\widehat{\boldsymbol{U}})|(\boldsymbol{U}_e - \widehat{\boldsymbol{U}}). \tag{3.24}$$

Again, this definition exploits the spectral decomposition of $\boldsymbol{A}_n(\widehat{\boldsymbol{U}})$, but now employing the diagonal matrix $\boldsymbol{\Phi}$, defined as $\Phi_{ii} = \max(|\lambda_i|, \delta)$, with λ_i being the i-th eigenvalue of $\boldsymbol{A}_n(\widehat{\boldsymbol{U}})$ and $\delta > 0$, a user-defined parameter. In particular, the entropy fix is aimed at recovering the failure of entropy conditions of the Roe solver, which may produce non-physical solutions in transonic and supersonic cases.

Remark 3.6. It is worth noting that the stabilisation matrix introduced in (3.22) for the Lax-Friedrichs Riemann solver is isotropic, whereas for the Roe numerical fluxes in (3.23), different values of the stabilisation term are introduced in the equations of conservation of mass, momentum and energy.

3.4.2 Discontinuous stabilisation across the interface: HLL-type Riemann solvers

Consider a discontinuous stabilisation matrix across the interface, defined as $\boldsymbol{\tau}^{\pm} = s^{\pm}\boldsymbol{\theta}$, with $s^+ \neq s^-$ and $\boldsymbol{\theta}$ a positive-definite square matrix of dimension $\mathbf{n_{sd}} + 2$. It follows

$$\widehat{\boldsymbol{U}} = \frac{s^+\boldsymbol{U}_e^+ + s^-\boldsymbol{U}_e^-}{s^+ + s^-}, \tag{3.25a}$$

$$\widehat{\boldsymbol{F}(\boldsymbol{U}_e)\boldsymbol{n}}^{\pm} = \boldsymbol{F}\left(\frac{s^+\boldsymbol{U}_e^+ + s^-\boldsymbol{U}_e^-}{s^+ + s^-}\right)\boldsymbol{n}^{\pm} + \frac{s^+s^-}{s^+ + s^-}\boldsymbol{\theta}(\boldsymbol{U}_e^{\pm} - \boldsymbol{U}_e^{\mp}). \tag{3.25b}$$

It is worth noting that the intermediate state in (3.25a) is obtained as a weighted average of the states $\boldsymbol{U}^+$ and $\boldsymbol{U}^-$. From this framework, HLL-type numerical fluxes, mimicking the behaviour of HLL (B.4) and HLLEM (B.5) for standard FV approaches, are devised for the first time in the context of hybridised methods. More precisely, the HLL Riemann solver is given by

$$\widehat{\boldsymbol{F}(\boldsymbol{U}_e)\boldsymbol{n}} = \boldsymbol{F}(\widehat{\boldsymbol{U}})\boldsymbol{n} + \left[s^+\mathbf{I}_{\mathbf{n_{sd}}+2}\right](\boldsymbol{U}_e - \widehat{\boldsymbol{U}}), \tag{3.26}$$

where $s^+ := \max(0, \widehat{\boldsymbol{v}} \cdot \boldsymbol{n} + \widehat{c})$.

Remark 3.7. A variant of the HLL Riemann solver in (3.26), the so-called Harten-Lax-van Leer-Einfeldt (HLLE) numerical flux introduced by Einfeldt (1988), can be devised by simply modifying the term s^+ in the stabilisation parameter as

$$s^+ := \max(0, \widehat{\boldsymbol{v}} \cdot \boldsymbol{n} + \widehat{c}, \boldsymbol{v}^+ \cdot \boldsymbol{n} + c^+, \boldsymbol{v}^- \cdot \boldsymbol{n} + c^-), \tag{3.27}$$

being $\odot^+$ and $\odot^-$ the variables associated with the states $\boldsymbol{U}_e^+$ and $\boldsymbol{U}_e^-$, respectively, at each side of the interface under analysis. Numerical experiments have shown that, in the context of high-order discretisations, the practical difference between HLL and HLLE numerical fluxes is not significant since the jumps across the interface are very small. Henceforth, the former choice is considered for simplicity.

Following the same rationale, the HLLEM numerical flux can be devised as

$$\widehat{\boldsymbol{F}(\boldsymbol{U_e})\boldsymbol{n}} = \boldsymbol{F}(\widehat{\boldsymbol{U}})\boldsymbol{n} + \left[s^+ \boldsymbol{\theta}(\widehat{\boldsymbol{U}}) \right] (\boldsymbol{U_e} - \widehat{\boldsymbol{U}}), \tag{3.28}$$

where $s^+ := \max(0, \widehat{\boldsymbol{v}} \cdot \boldsymbol{n} + \widehat{c})$ is the HLL estimate for the largest wave speed and $\boldsymbol{\theta}(\widehat{\boldsymbol{U}}) = \boldsymbol{R\Theta L}$, as defined in (B.5). It is worth noticing that the intermediate state is selected such that $\boldsymbol{U}^\star = \widehat{\boldsymbol{U}}$. Therefore, $\boldsymbol{\Theta}$ employs $\theta^\star = \widehat{\theta} = |\widehat{\boldsymbol{v}} \cdot \boldsymbol{n}|/(|\widehat{\boldsymbol{v}} \cdot \boldsymbol{n}| + \widehat{c})$, where the hat quantities are evaluated using the hybrid variable $\widehat{\boldsymbol{U}}$.

Remark 3.8. Because of the positive definition of the matrix $\boldsymbol{\theta}$ introduced here, the coefficient $\widehat{\theta}$ is not allowed to reach zero. This situation is experienced in flows that are perfectly aligned with the faces of the mesh. From a practical point of view, it may be useful to set a minimum threshold $0 < \theta_0 \ll 1$ to guarantee that $\widehat{\theta} > \theta_0$ and avoid a null stabilisation.

3.5 HDG discretisation

The HDG discretisation is finally obtained by introducing the numerical fluxes (3.14) and boundary conditions (detailed in table 2.1) in the weak forms of the local (3.11) and global (3.12) problems.

Indeed, the corresponding expression of the weak forms of the local and global problems is given by:

Local problems: given $\widehat{\boldsymbol{U}} \in [\widehat{\mathcal{W}}_t^h(\Gamma \cup \partial\Omega)]^{\texttt{n}_{\texttt{sd}}+2}$, find $(\boldsymbol{U_e}, \boldsymbol{\varepsilon}_e^d, \boldsymbol{\phi_e}) \in [\mathcal{W}_t^h(\Omega_e)]^{\texttt{n}_{\texttt{sd}}+2} \times [\mathcal{W}_t^h(\Omega_e)]^{\texttt{m}_{\texttt{sd}}} \times [\mathcal{W}_t^h(\Omega_e)]^{\texttt{n}_{\texttt{sd}}}$ such that

$$\left(\boldsymbol{\zeta}, \boldsymbol{\varepsilon}_e^d \right)_{\Omega_e} + (\boldsymbol{\nabla} \cdot \mathcal{D}\boldsymbol{\zeta}, \boldsymbol{v_e})_{\Omega_e} - \langle \boldsymbol{\zeta}, \mathcal{D}\widehat{\boldsymbol{v}} \otimes \boldsymbol{n} \rangle_{\partial\Omega_e} = 0, \tag{3.29a}$$

$$(\boldsymbol{\xi}, \boldsymbol{\phi_e})_{\Omega_e} + (\boldsymbol{\nabla} \cdot \boldsymbol{\xi}, T_e)_{\Omega_e} - \left\langle \boldsymbol{\xi}, \widehat{T}\boldsymbol{n} \right\rangle_{\partial\Omega_e} = 0, \tag{3.29b}$$

$$\left(\boldsymbol{W}, \frac{\partial \boldsymbol{U_e}}{\partial t} \right)_{\Omega_e} - \left(\boldsymbol{\nabla}\boldsymbol{W}, \boldsymbol{F}(\boldsymbol{U_e}) - \boldsymbol{G}(\boldsymbol{U_e}, \boldsymbol{\varepsilon}_e^d, \boldsymbol{\phi_e}) \right)_{\Omega_e}$$
$$+ \left\langle \boldsymbol{W}, \left(\boldsymbol{F}(\widehat{\boldsymbol{U}}) - \boldsymbol{G}(\widehat{\boldsymbol{U}}, \boldsymbol{\varepsilon}_e^d, \boldsymbol{\phi_e}) \right)\boldsymbol{n} \right\rangle_{\partial\Omega_e} + \left\langle \boldsymbol{W}, \left(\boldsymbol{\tau}^a(\widehat{\boldsymbol{U}}) + \boldsymbol{\tau}^d \right) \left(\boldsymbol{U_e} - \widehat{\boldsymbol{U}} \right) \right\rangle_{\partial\Omega_e} = 0, \tag{3.29c}$$

for all $(\boldsymbol{W}, \boldsymbol{\zeta}, \boldsymbol{\xi}) \in [\mathcal{W}_t^h(\Omega_e)]^{\texttt{n}_{\texttt{sd}}+2} \times [\mathcal{W}_t^h(\Omega_e)]^{\texttt{m}_{\texttt{sd}}} \times [\mathcal{W}_t^h(\Omega_e)]^{\texttt{n}_{\texttt{sd}}}$ in every element Ω_e, $e = 1, \dots, \texttt{n}_{\texttt{el}}$.

Global problem: find $\widehat{\boldsymbol{U}} \in [\widehat{\mathcal{W}}_t^h(\Gamma \cup \partial\Omega)]^{\texttt{n}_{\texttt{sd}}+2}$ satisfying

$$\sum_{e=1}^{\mathtt{n_{el}}} \left\{ \left\langle \widehat{\boldsymbol{W}}, \left(\boldsymbol{F}(\widehat{\boldsymbol{U}}) - \boldsymbol{G}(\widehat{\boldsymbol{U}}, \boldsymbol{\varepsilon}_e^d, \boldsymbol{\phi}_e) \right) \boldsymbol{n} \right\rangle_{\partial\Omega_e \cap \Gamma} + \left\langle \widehat{\boldsymbol{W}}, \left(\boldsymbol{\tau}^a(\widehat{\boldsymbol{U}}) + \boldsymbol{\tau}^d \right) \left(\boldsymbol{U}_e - \widehat{\boldsymbol{U}} \right) \right\rangle_{\partial\Omega_e \cap \Gamma} \right.$$

$$\left. + \left\langle \widehat{\boldsymbol{W}}, \widehat{\boldsymbol{B}}(\widehat{\boldsymbol{U}}, \boldsymbol{U}_e, \boldsymbol{\varepsilon}_e^d, \boldsymbol{\phi}_e) \right\rangle_{\partial\Omega_e \cap \partial\Omega} \right\} = 0, \quad (3.30)$$

for all $\widehat{\boldsymbol{W}} \in [\widehat{\mathcal{W}}_t^h(\Gamma \cup \partial\Omega)]^{\mathtt{n_{sd}}+2}$.

3.5.1   Solution strategy

The HDG solution can be then obtained in a process featuring two stages, owing to hybridisation. First, the local problems are devised.

To this end, denote by $\boldsymbol{Z}_e = (\boldsymbol{U}_e, \boldsymbol{\varepsilon}_e^d, \boldsymbol{\phi}_e) \in [\mathcal{W}_t^h(\Omega_e)]^{\mathtt{n_{sd}}+2} \times [\mathcal{W}_t^h(\Omega_e)]^{\mathtt{m_{sd}}} \times [\mathcal{W}_t^h(\Omega_e)]^{\mathtt{n_{sd}}}$ the vector of local unknowns, which includes the primal and mixed variables. By considering an isoparametric approximation in space for the local, $\boldsymbol{Z}$, and hybrid, $\widehat{\boldsymbol{U}}$, variables, the semi-discrete system of differential-algebraic equations resulting from the local problem at element $\Omega_e,\ e = 1, \ldots, \mathtt{n_{el}}$ reads

$$\mathbf{M}_e \frac{d\mathbf{Z}_e}{dt} + \mathbf{R}_e(\mathbf{Z}_e, \widehat{\mathbf{U}}) = \mathbf{0}. \qquad (3.31)$$

where $\mathbf{Z}_e$ and $\widehat{\mathbf{U}}$ denote the vectors of nodal values of the local and hybrid variables, respectively, and $\mathbf{M}_e$ and $\mathbf{R}_e$ are the mass matrix and nonlinear residual vector obtained from the spatial discretisation of the integral terms of the local problem (3.11) in element Ω_e.

In a similar fashion, from the global problem (3.12) it follows

$$\sum_{e=1}^{\mathtt{n_{el}}} \widehat{\mathbf{R}}_e(\widehat{\mathbf{U}}, \mathbf{Z}_e) = \mathbf{0}, \qquad (3.32)$$

where $\widehat{\mathbf{R}}_e$ denotes the nonlinear residual vector involving the degrees of freedom associated with element Ω_e.

Finally, upon temporal discretisation, the resulting nonlinear system is solved using a Newton-Raphson iterative method at each time step. In particular, the linear system of equations arising at each time step and Newton-Raphson iteration for the local problems reads

$$\mathbf{A}_{ZZ}^e \mathbf{Z}_e + \mathbf{A}_{Z\widehat{U}}^e \widehat{\mathbf{U}} = \mathbf{F}_Z^e \qquad (3.33)$$

for $e = 1, \ldots, \mathtt{n_{el}}$, where vectors $\mathbf{F}_\diamond^e$ and matrices $\mathbf{A}_{\diamond\diamond}^e$ are obtained from Newton-Raphson linearisation of the system of equations (3.31). Similarly, the linear system

corresponding to the global problem (3.32) upon Newton-Raphson linearisation can be expressed as

$$\sum_{e=1}^{\mathtt{n_{el}}} \left\{ \mathbf{A}_{\widehat{U}\widehat{U}}^{e} \widehat{\mathbf{U}} + \mathbf{A}_{\widehat{U}Z}^{e} \mathbf{Z}_e - \mathbf{F}_{\widehat{U}}^{e} \right\} = \mathbf{0}. \tag{3.34}$$

Note that, owing to the hybridisation procedure, the elemental degrees of freedom of $\mathbf{Z}_e$ can be rewritten in terms of the globally coupled degrees of freedom of $\widehat{\mathbf{U}}$ via (3.33), namely

$$\mathbf{Z}_e = [\mathbf{A}_{ZZ}^{e}]^{-1} \mathbf{F}_Z^{e} - [\mathbf{A}_{ZZ}^{e}]^{-1} \mathbf{A}_{Z\widehat{U}}^{e} \widehat{\mathbf{U}}, \tag{3.35}$$

which just involves the inverse of matrix $\mathbf{A}_{ZZ}^{e}$, of dimension $((\mathtt{n_{sd}} + 2 + \mathtt{m_{sd}} + \mathtt{n_{sd}})\mathtt{n_{en}})$, for each element of the mesh, being $\mathtt{n_{en}}$ the number of element nodes of Ω_e. This computation can be effectively parallelised and only involves the solution of small systems with limited computing effort. Dimension of such local systems is displayed in table 3.1 for different degrees of approximation k on simplexes and parallelepipeds in 2D and 3D.

Table 3.1: Dimension of the local problem.

Degree of approximation, k	1	2	3	4	5	6
Simplexes						
2D	27	54	90	135	189	252
3D	56	140	280	490	784	1,176
Parallelepipeds						
2D	36	81	144	225	324	441
3D	112	378	896	1,750	3,024	4,802

The hybridisation procedure (3.35) permits to eliminate $\mathbf{Z}_e$ in equation (3.34), giving rise to a linear system with a reduced number of degrees of freedom, as described by Cockburn (2016), similarly as the static condensation introduced by Guyan (1965). This global system is the one to be solved at each Newton-Raphson iteration and reads as

$$\mathbf{K}\widehat{\mathbf{U}} = \mathbf{F}, \tag{3.36}$$

where the global matrix $\mathbf{K}$ and the right-hand side vector $\mathbf{F}$ are obtained by assembling the elemental contributions

$$\mathbf{K}^e = \mathbf{A}_{\widehat{U}\widehat{U}}^{e} - \mathbf{A}_{\widehat{U}Z}^{e} [\mathbf{A}_{ZZ}^{e}]^{-1} \mathbf{A}_{Z\widehat{U}}^{e}, \tag{3.37a}$$

$$\mathbf{F}^e = \mathbf{F}_{\widehat{U}}^{e} - \mathbf{A}_{\widehat{U}Z}^{e} [\mathbf{A}_{ZZ}^{e}]^{-1} \mathbf{F}_Z^{e}. \tag{3.37b}$$

As the main purpose of this work is the evaluation of the HDG formulation of compressible flows in terms of positivity and shear preservation when employing the different Riemann solvers introduced in 3.4, only steady-state problems are considered. In this context, the temporal discretisation in equation (3.31) is used as a relaxation method to improve the convergence process in complex numerical examples, e.g. in presence of shocks. To this effect, the backward Euler method is considered in the simulations. However, the proposed methodology is applicable to other time discretisations, such as high-order time integrators like backward difference formulas (BDF) or diagonally implicit Runge-Kutta (DIRK) methods, especially suited for transient problems, as described by Nguyen and Peraire (2012), Jaust and Schütz (2014) and Jaust et al. (2015).

3.5.2 Shock-capturing method

It is well-known that high-order methods experience an oscillatory behaviour in the vicinity of shocks and regions with sharp gradients, as described by Godunov and Bohachevsky (1959) and detailed in Donea and Huerta (2003). In those cases, appropriate shock-capturing techniques are required, such as the introduction of an artificial viscosity term, added to regularise the numerical approximation of the problem in those regions.

Different approaches can be adopted to introduce artificial dissipation. In this thesis, two different alternatives are presented. First, a physics-based shock capturing method proposed by Fernández et al. (2017) which introduces the artificial viscosity within the viscous flux $\boldsymbol{G}$ is detailed. Additionally, a Laplacian-based approach, formulated in a discrete version to avoid the introduction of mixed variables, such as the one employed by Jaust et al. (2015), is considered for the Euler equations.

3.5.2.1 Physics-based shock capturing

In this approach, shock waves are stabilised by correcting the diffusive flux in equation (2.2) using the physics-based approach proposed by Fernández et al. (2018). This methodology, stemming from the work of Von Neumann and Richtmyer (1950) and later considered by Cook and Cabot (2005), Kawai and Lele (2008) and Kawai et al. (2010), among others, relies on defining the diffusive flux as a combination of the physical flux $\boldsymbol{G}$ with an additional numerical contribution $\boldsymbol{G}^*$. The latter is thus

65

based on an artificial bulk viscosity β^*, namely

$$\boldsymbol{G}^* = \beta^* \begin{bmatrix} \mathbf{0} \\ (\boldsymbol{\nabla} \cdot \boldsymbol{v})\mathbf{I}_{\mathrm{n_{sd}}} \\ \left[(\boldsymbol{\nabla} \cdot \boldsymbol{v})\boldsymbol{v} + Pr_\beta^{-1}\boldsymbol{\phi} \right]^T \end{bmatrix}, \tag{3.38}$$

where Pr_β is an artificial Prandtl number.

First, a dilatation-based shock sensor proposed by Moro et al. (2016) and later employed by Fernández et al. (2018), which identifies the regions of high compression, is defined as

$$s_\beta = -\frac{h}{k}\frac{\boldsymbol{\nabla} \cdot \boldsymbol{v}}{\tilde{c}}, \tag{3.39}$$

where h is the element size, k is the degree of polynomial approximation and $\tilde{c}$ is a reference speed of sound for non-dimensionalisation. Common choices for $\tilde{c}$ are the critical speed of sound $c^\star$, the speed of sound at the actual point c, or simply the reference free-stream value c_∞. In the simulations presented in section 4, the latter option is employed.

The shock sensor s_β is thus utilised to define the artificial bulk viscosity β^* as

$$\beta^* = \Psi \left(\varepsilon_0 \left[\rho_\infty \frac{h}{k}(v_\infty^2 + c_\infty^2)^{1/2} \right] f_\beta(s_\beta) \right), \tag{3.40}$$

where Ψ denotes a smoothing operator consisting of a $\mathcal{C}^0$ reconstruction, as defined by Persson (2013), ε_0 is a user-defined positive constant and

$$f_\beta(s_\beta) = \min \left\{ s_{\max}, \max\{s_{\min}, s_\beta - s_0\} \right\}. \tag{3.41}$$

Following Fernández et al. (2018) the values $\varepsilon_0 = 1.5$, $s_0 = 0.01$, $s_{\min} = 0$ and $s_{\max} = 2/\sqrt{\gamma^2 - 1}$ and the artificial Prandtl number $Pr_\beta = 0.9$ are employed in the numerical simulations of this chapter.

3.5.2.2 Laplacian-based shock capturing

The second alternative for the shock capturing detailed in this section consists of a discretised Laplace operator, applied in HDG discretisations by Jaust et al. (2015, 2014) following standard approaches in the context of DG and SUPG methods, such as in Bassi and Rebay (1995), Cockburn (2001), Casoni et al. (2012) or Sevilla et al. (2013). Given the artificial viscosity ε, it relies on adding the term

$$(\boldsymbol{\nabla}\boldsymbol{W}, \varepsilon\boldsymbol{\nabla}\boldsymbol{U})_{\Omega_e} \tag{3.42}$$

to the left-hand side of the local equation (3.11c), or (3.16) for the Euler case. This approach is especially suited for the inviscid case, where the second-order term $\boldsymbol{G}$ vanishes and the mixed variables in (3.11a) and (3.11b) are neglected.

The shock capturing technique is equipped with a discontinuity sensor S_e, introduced by Persson and Peraire (2006) and expressed in terms of the density field according to Persson (2013), namely

$$S_e := \frac{(\rho_e - \widetilde{\rho}_e, \rho_e - \widetilde{\rho}_e)_{\Omega_e}}{(\rho_e, \rho_e)_{\Omega_e}}. \tag{3.43}$$

The smoothness indicator S_e is utilised to detect the regions with discontinuities. In (3.43), ρ_e denotes the density in the element Ω_e, computed using a polynomial approximation of degree k, and $\widetilde{\rho}_e$ is its truncation of order $k-1$. The sensor measures the regularity of the approximate solution based on the rate of decay of its Fourier coefficients. More precisely, if $S_e > k^{-4}$, such approximation is expected to be at most $\mathcal{C}^0$, whereas smooth functions are expected to decay more rapidly, as detailed by Casoni et al. (2012).

Following Sevilla et al. (2008) and Huerta et al. (2011), the sensor (3.43) is implemented using nodal basis functions. It follows that

$$S_e = \frac{\boldsymbol{\rho}_e^T \mathbf{V}^{-T} \mathbf{P} \mathbf{V}^{-1} \boldsymbol{\rho}_e}{\boldsymbol{\rho}_e^T \mathbf{V}^{-T} \mathbf{V}^{-1} \boldsymbol{\rho}_e}, \tag{3.44}$$

where $\boldsymbol{\rho}_e$ is the vector containing the nodal values of the density field in the element Ω_e, $\mathbf{V}$ is the Vandermonde matrix whose inverse maps the Lagrange basis onto the orthonormal one and $\mathbf{P}$ is the orthogonal projection matrix onto the space of monomials of degree k, namely

$$\mathbf{P} := \text{diag}(\overbrace{0, \ldots, 0}^{\mathtt{n_L}}, \overbrace{1, \ldots, 1}^{\mathtt{n_H}}), \tag{3.45}$$

being $\mathtt{n_L}$ and $\mathtt{n_H}$ the number of degrees of freedom for monomials of degree $k-1$ and k, respectively. In two dimensions, it holds $\mathtt{n_L} := k+1$ and $\mathtt{n_H} := k(k+1)/2$.

The amount of artificial viscosity introduced in each element is determined according to

$$\varepsilon_e = \begin{cases} 0, & \text{if } s_e < s_0 - \xi, \\ \dfrac{\varepsilon_0}{2}\left(1 + \sin\left(\dfrac{\pi(s_e - s_0)}{2\xi}\right)\right), & \text{if } s_0 - \xi < s_e < s_0 + \xi, \\ \varepsilon_0, & \text{if } s_e > s_0 + \xi, \end{cases} \tag{3.46}$$

where $s_e := \log_{10} S_e$ and $\varepsilon_0 \sim h/k$. In these expressions, s_0 and ξ are selected such that $s_0 + \xi = -4 \log_{10} k$ and $s_0 - \xi$ is sufficiently large to detect the regions in which mild shock waves are present, according to Huerta et al. (2011). In particular, a value $s_0 - \xi = -11 \log_{10} k$ is considered in upcoming numerical studies. Finally, the smoothing operator Ψ is employed to perform a $\mathcal{C}^0$ reconstruction of the elemental artificial viscosity obtained in (3.46), that is $\varepsilon = \Psi(\varepsilon_e)$.

Chapter 4

Benchmarking for high-order compressible flows [1]

A comprehensive set of computational benchmarks, spanning from subsonic flows to supersonic inviscid and viscous cases with shocks, is presented in this chapter to examine the capabilities of the high-order HDG solver presented in chapter 3. In particular, the corresponding numerical examples are employed to evaluate the performance of the HDG formulation equipped with the proposed Riemann solvers, i.e. Lax-Friedrichs, Roe, HLL and HLLEM. This section is also aimed at providing a useful extensive list of compressible flow examples of practical interest to be employed for numerical validation.

It is worth mentioning that, in this work, the main interest has been focused on the HDG formulation for compressible flows and the presentation of a unified framework for the Riemann solvers in HDG. To this end, the examples considered involve steady-state flows.

The organisation of this chapter is the following. Section 4.1 examines the optimal accuracy properties of the proposed HDG formulation in a pair of convergence studies for inviscid and viscous flows. Then, a set of numerical benchmarks for a variety of flow conditions is presented in section 4.2 to test the performance and robustness of the HDG solver. Finally, section 4.3 summarises the main results of this study.

---

[1]This chapter is based on the published article Vila-Pérez et al. (2020)

4.1   Validation and convergence studies

The optimal convergence properties of the HDG method are tested both in inviscid and viscous cases. The accuracy of the approximation is examined using the four Riemann solvers presented in section 3.4 for different degrees of polynomial approximation.

4.1.1   Convergence analysis for inviscid flows: Ringleb flow

The Ringleb flow problem is considered to verify the optimal convergence of the HDG method for inviscid flows. As described in section 2.3.1, where it has been employed, the Ringleb problem, presented by Chiocchia (1985), consists of a smooth transonic 2D solution of the Euler equations with analytical expression obtained via the hodograph method. For any given spatial coordinates (x, y), the solution of the Ringleb flow can be computed by solving the following nonlinear implicit equation in terms of the speed of sound c,

$$\left(x + \frac{J}{2}\right)^2 + y^2 = \frac{1}{4\rho^2 V^4}, \tag{4.1}$$

where the following relationships for density ρ, radial velocity V and J hold

$$\rho = c^{2/(\gamma - 1)}, \quad V = \sqrt{\frac{2(1 - c^2)}{\gamma - 1}}, \quad J = \frac{1}{c} + \frac{1}{3c^3} + \frac{1}{5c^5} - \frac{1}{2}\log\left(\frac{1 + c}{1 - c}\right). \tag{4.2}$$

The exact velocity and pressure fields are

$$\boldsymbol{v} = \left\{\begin{array}{c} -\text{sgn}\,(y)V\sin\theta \\ V\cos\theta \end{array}\right\} \quad \text{and} \quad p = \frac{1}{\gamma}c^{2\gamma/(\gamma - 1)}, \tag{4.3}$$

where $\text{sgn}\,(\cdot)$ is the *sign* operator, $\sin\theta := \Psi V$ and

$$\Psi := \sqrt{\frac{1}{2V^2} + \rho\left(x + \frac{J}{2}\right)}. \tag{4.4}$$

Remark 4.1 (Computation of the Ringleb solution). It is worth noting that the nonlinear equation driving the analytical solution of the Ringleb problem (4.1) needs to be solved iteratively upon a certain tolerance, thus introducing an approximation error in the estimated analytical solution. Further operations in order to compute the rest of variables of the problem may be responsible for the propagation of such

error, which may become critical in high-order convergence tests. In these cases, the error introduced in the exact solution may be of similar level or even higher than the error of the approximate solution. Then, the computed approximation error is no longer reliable, showing a stagnation in the levels of accuracy.

Such numerical issues were circumvented in this study by avoiding the computation of Ψ directly as in (4.4) but using trigonometric identities and algebraic manipulation of (4.1) to compute the direction of the flow, namely

$$\sin(2\theta) = 2\sin\theta\cos\theta = 2\Psi V\sqrt{1 - \Psi^2 V^2} = 2\sqrt{\frac{1}{4} - \rho^2 V^4\left(x + J/2\right)^2} = 2\rho V^2 y. \quad (4.5)$$

It is worth mentioning that these numerical issues may be more evident in those regions of the domain where the solution displays greater variations, namely those including supersonic speeds.

In this study, the Ringleb problem is solved in the domain $\Omega = [0,1]^2$, with far-field boundary conditions on $\partial\Omega$. The computational domain is discretised using uniform meshes of triangular elements. Figure 4.1 displays the first three levels of refinement employed.

(a) Mesh 1   (b) Mesh 2   (c) Mesh 3
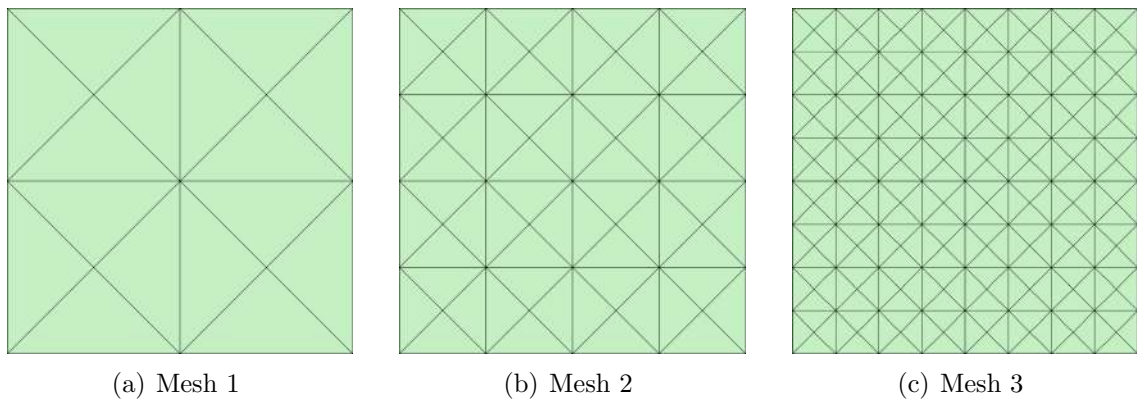
Figure 4.1: Ringleb flow - Triangular meshes of $\Omega = [0,1]^2$ for the h-convergence analysis.

The approximate solution of the Mach number distribution computed on the mesh in figure 4.1(a) using polynomial degree $k = 1, \ldots, 3$ is depicted in figure 4.2. The results clearly display the gain in accuracy obtained increasing the degree of the polynomial approximation, even in presence of extremely coarse meshes, motivating the interest in high-order discretisations.

An h-convergence study is performed using a degree of approximation ranging from $k = 1$ up to $k = 4$ and for the four Riemann solvers presented in section 3.4.

(a) $k = 1$ (b) $k = 2$ (c) $k = 3$
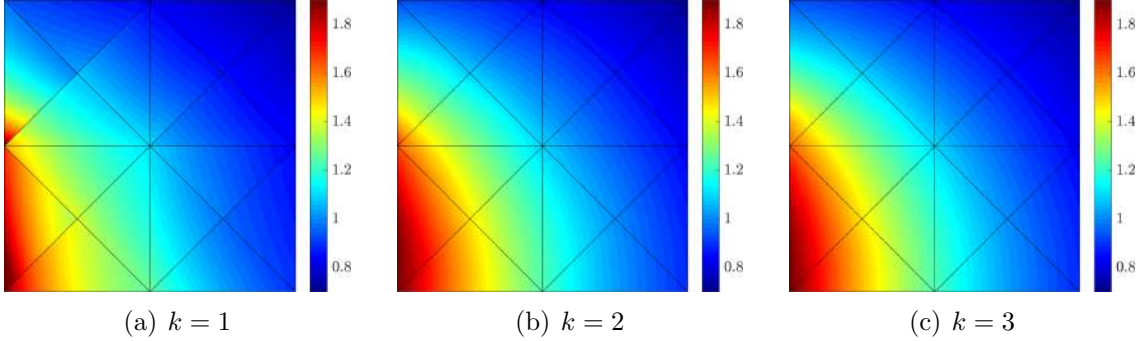
Figure 4.2: Ringleb flow - Mach number distribution computed using the HLL Riemann solver on the first level of mesh refinement with polynomial degree $k = 1, \ldots, 3$.

Figure 4.3 displays the error for the conserved variables, i.e. ρ, $\rho\boldsymbol{v}$ and ρE, measured in the $\mathcal{L}_2(\Omega)$ norm, as a function of the characteristic mesh size h. It can be observed that the different Riemann solvers lead to an optimal rate of convergence h^{k+1} and a comparable accuracy in all cases.

(a) Density, ρ (b) Momentum, $\rho\boldsymbol{v}$ (c) Energy, ρE
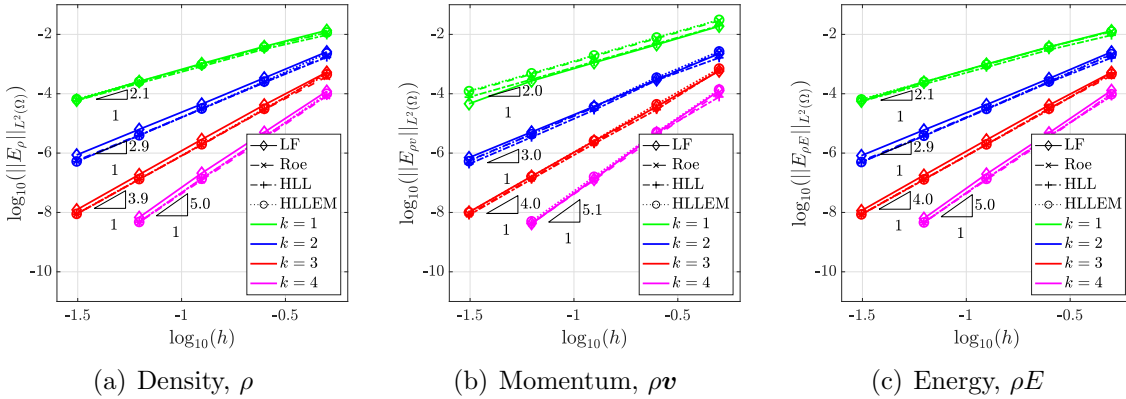
Figure 4.3: Ringleb flow - Mesh convergence of the $\mathcal{L}_2$ error of (a) density, (b) momentum and (c) energy, using Lax-Friedrichs (LF), Roe, HLL and HLLEM Riemann solvers and polynomial degree of approximation $k = 1, \ldots, 4$.

It is worth mentioning that the level of accuracy obtained in mesh 5 with a linear approximation $k = 1$ (49,664 DOFs) is comparable to the one achieved on the coarsest mesh with polynomial degree of approximation $k = 4$ (560 DOFs). Hence, the results show the superiority of high-order discretisations, which allow to highly reduce the size of the HDG problem for a given level of accuracy.

4.1.2 Convergence analysis for viscous flows: Couette flow

The compressible Couette flow with a source term example presented in section 2.3.2 is considered to numerically verify the accuracy and convergence properties of the high-order HDG method for the compressible Navier-Stokes equations using the different Riemann solvers presented in section 3.4.

The analytical expression of the solution, defined on the square domain $\Omega = [0, 1]^2$, is

$$\boldsymbol{v} = \begin{Bmatrix} y \log(1 + y) \\ 0 \end{Bmatrix}, \qquad p = \frac{1}{\gamma M_\infty^2}$$

$$T = \frac{1}{(\gamma - 1)M_\infty^2} \left[\alpha_c + y(\beta_c - \alpha_c) + \frac{(\gamma - 1)M_\infty^2 Pr}{2} y(1 - y) \right], \tag{4.6}$$

where $\alpha_c = 0.8$ and $\beta_c = 0.85$ are positive constants. The viscosity is assumed constant and the source term, which is determined from the exact solution, is given by

$$\boldsymbol{S} = \frac{-1}{Re} \left\{ 0, \; \frac{2 + y}{(1 + y)^2}, \; 0, \; \log^2(1 + y) + \frac{y \log(1 + y)}{1 + y} + \frac{y(3 + 2y) \log(1 + y) - 2y - 1}{(1 + y)^2} \right\}^T . \tag{4.7}$$

The exact solution is utilised to impose the boundary conditions on $\partial\Omega$ and the nondimensional quantities are set to $M_\infty = 0.15$ and $Re = 1$ in order to replicate the case presented by Nguyen and Peraire (2012) and Schütz et al. (2012), taking a characteristic length $L = 1$.

The computational domain is discretised using the uniform meshes of triangular elements employed in the Ringleb example of section 4.1.1. Figure 4.4 displays the approximate solution of the density field on the first mesh refinement for polynomial degrees $k = 1, \ldots, 3$.

The evolution of the error of the primal (conserved) and mixed variables measured in the $\mathcal{L}_2(\Omega)$ norm is displayed in figure 4.5, as a function of the characteristic element size h. The h-convergence study compares the results of the Lax-Friedrichs, Roe, HLL and HLLEM Riemann solvers, using polynomial degrees of approximation from $k = 1$ to $k = 4$. Optimal rates of convergence and comparable levels of accuracy are obtained for the approximation of the primal and mixed variables using the different Riemann solvers.

Finally, the rates of convergence of the mixed variables in the last mesh refinement, $r_\diamond$, are examined with respect to the Reynolds number. In particular, whereas

(a) $k = 1$ (b) $k = 2$ (c) $k = 3$
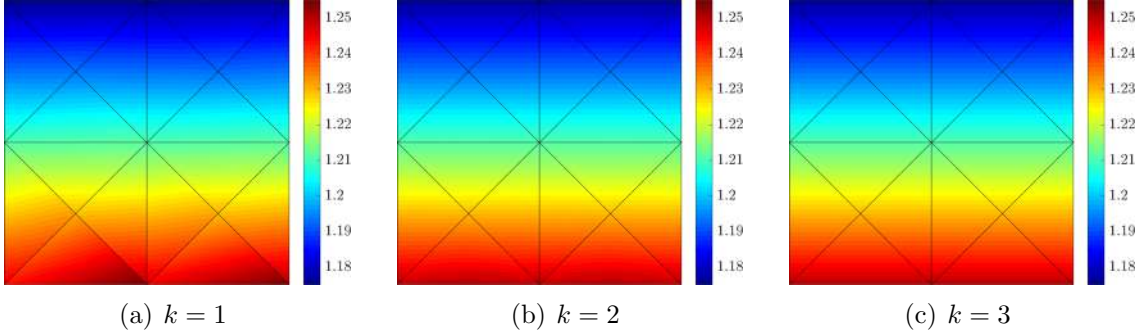
Figure 4.4: Couette flow - Density distribution computed using the HLLEM Riemann solver on the first level of mesh refinement with polynomial degree $k = 1, \dots, 3$.

(a) Density, ρ (b) Momentum, $\rho\boldsymbol{v}$ (c) Energy, ρE

(d) Stress tensor, $\boldsymbol{\sigma}^d$ (e) Heat flux, $\boldsymbol{q}$
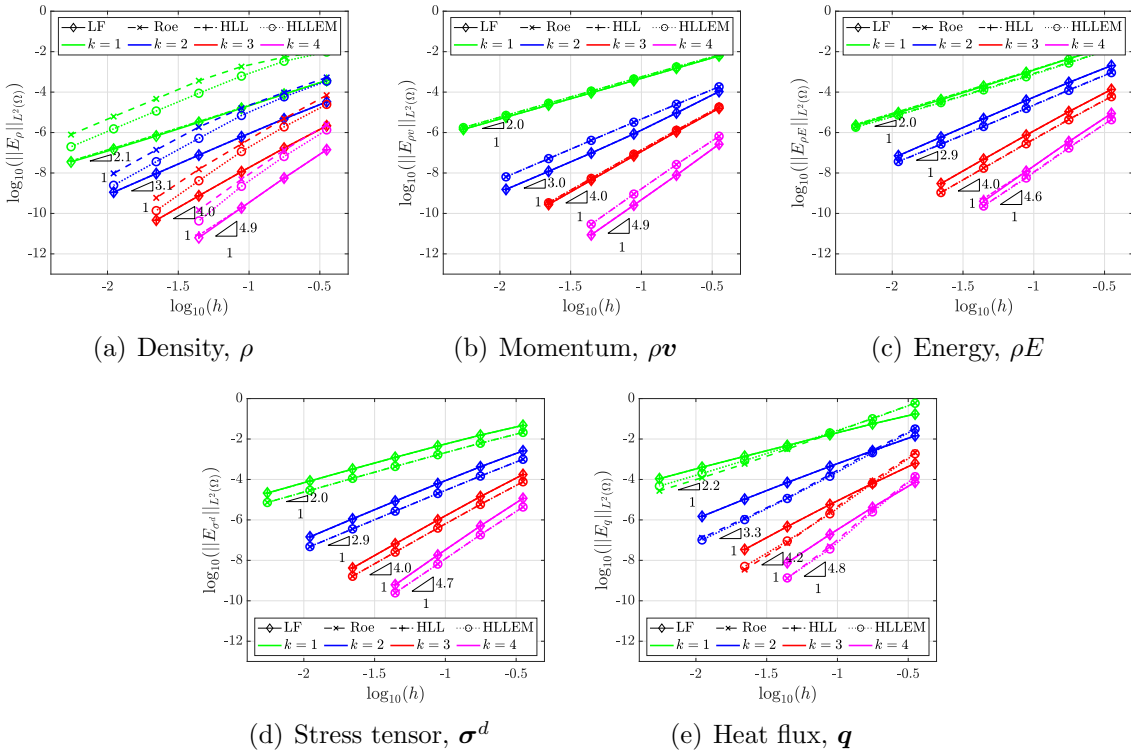
Figure 4.5: Couette flow - Mesh convergence of the $\mathcal{L}_2$ error of the (a–c) primal variables –density, momentum and energy–, (d) stress tensor and (e) heat flux, using Lax-Friedrichs (LF), Roe, HLL and HLLEM Riemann solvers and polynomial degree of approximation $k = 1, \dots, 4$.

for $Re = 1$ the four Riemann solvers show similar rates of convergence of $k + 1$, as displayed in figure 4.5, figure 4.6 illustrates the decreasing tendency of such convergence rates as the problem turns convection-dominated. HLLEM and Roe Riemann solvers display an increased accuracy with respect to Lax-Friedrichs and HLL, keeping optimal rates of convergence even for $Re = 1000$. On the contrary, Lax-Friedrichs and HLL exhibit a steeper drop in accuracy, experiencing a suboptimal behaviour as the Reynolds number increases.

(a) Viscous stress tensor, $\boldsymbol{\sigma}^d$ (b) Heat flux, $\boldsymbol{q}$
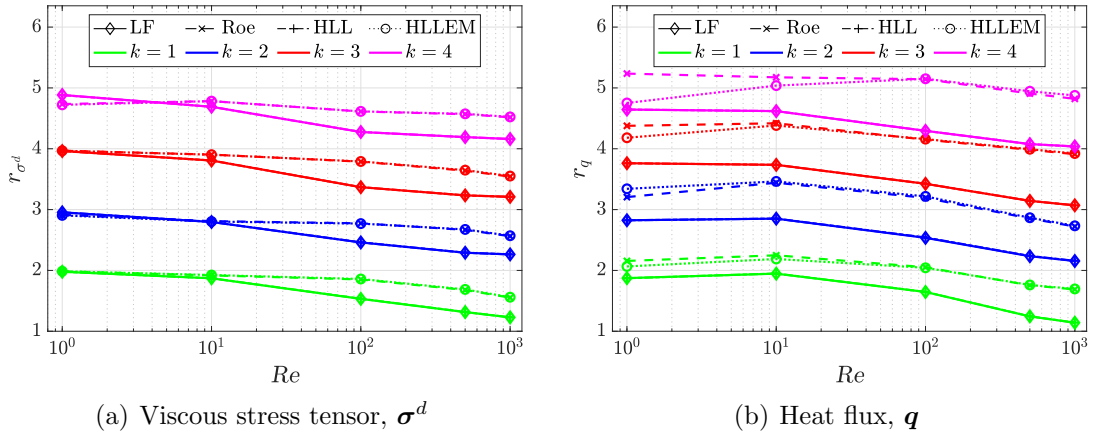
Figure 4.6: Couette flow - Rate of convergence of the viscous stress and the heat flux for variable Reynolds, using Lax-Friedrichs (LF), Roe, HLL and HLLEM Riemann solvers and polynomial degree of approximation $k = 1, \ldots, 4$.

4.2   Numerical benchmarks

A set of numerical examples is presented in this section to evaluate the performance and accuracy of the different Riemann solvers for inviscid and viscous compressible flows in the context of the high-order HDG method. Different cases, listed in table 4.1, are considered, ranging from viscous laminar to inviscid flows, both in subsonic, transonic and supersonic regimes.

4.2.1   Entropy production due to geometrical error: subsonic flow past a circular cylinder

The subsonic flow around a circular cylinder at free-stream Mach number $M_\infty = 0.3$ is considered to assess the numerical dissipation introduced by the different Riemann solvers in the context of HDG methods.

Table 4.1: List of examples.

Inviscid examples	
4.2.1	Subsonic flow past a circular cylinder
4.2.3	Transonic flow over a NACA 0012 aerofoil
4.2.4	Supersonic flow over a NACA 0012 aerofoil

Viscous examples	
4.2.2	Subsonic laminar flow over a flat plate
4.2.5	Shock wave/boundary layer interaction
4.2.6	Supersonic flow over a compression corner

In particular, it is known that the geometrical error introduced by low-order descriptions of curved boundaries is responsible for a substantial nonphysical entropy production, as studied in detail by Bassi and Rebay (1997b). Possible solutions involve the modification of the wall boundary condition, proposed by Krivodonova and Berger (2006), or the incorporation of the exact boundary representation, described by Sevilla et al. (2008). As mentioned earlier, isoparametric approximations are considered in this work. Therefore, only approximations of degree at least $k = 2$ are reported, preventing the geometrical error from dominating over the dissipative behaviour of the Riemann solvers under analysis.

Two meshes are considered for this example. The coarsest mesh consists of $1,104$ triangles with 32 elements to discretise the circle, whereas the finest mesh has $4,635$ elements and 64 subdivisions on the circle. A detailed view of the corresponding meshes near the cylinder is depicted in figure 4.7. The far-field boundary is placed at 15 diameters from the circle and inviscid wall conditions are set on the cylinder boundary.

For isentropic subsonic flows, the entropy production is a measure of the numerical dissipation introduced by the spatial discretisation. The nonphysical entropy production is computed via the so-called *entropy error*, namely

$$\varepsilon_{\text{ent}} = \frac{p}{p_\infty} \left(\frac{\rho_\infty}{\rho} \right)^\gamma - 1, \tag{4.8}$$

measuring the relative error of the total pressure with respect to the undisturbed flow in an isentropic process.

Figure 4.8 (top) shows the Mach number distribution and isolines of the numerical solution computed on the first mesh with $k = 2, \dots, 4$, using the HLL Riemann

(a) Mesh 1   (b) Mesh 2
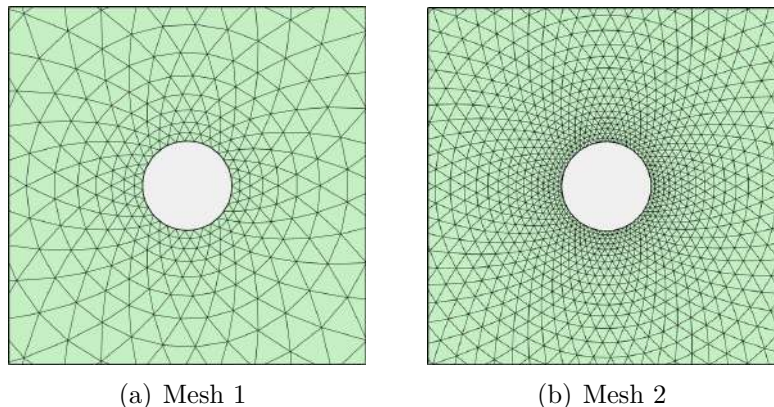
Figure 4.7: Subsonic flow around a cylinder - Detail of the meshes near the 2D cylinder, featuring (a) 32 and (b) 64 subdivisions on the circular boundary.

solver. Although the computed distribution of the Mach number is comparable in the three settings, the superiority of high-order approximations becomes evident when the corresponding entropy errors are compared (figure 4.8, bottom). The results clearly display that, increasing the polynomial degree of discretisation, the numerical dissipation introduced by the method is localised in the vicinity of the cylinder and its overall amount is reduced.

To quantify the differences between the four Riemann solvers, the nonphysical entropy production is compared through the $\mathcal{L}_2$ norm of the entropy error, measured on the surface of the cylinder. Figure 4.9 displays the quantity (4.8) as a function of the number of degrees of freedom of the global problem, for the two meshes under analysis and an increasing value of the polynomial degree used to approximate the solution. The results show that the entropy production of the HLL Riemann solver is almost identical when compared to the Lax-Friedrichs Riemann solver, whereas HLLEM matches the entropy production by the Roe numerical flux. Moreover, as expected for a subsonic flow, the entropy production is slightly lower for the HLLEM and Roe Riemann solvers.

It is worth noting that the differences among the Riemann solvers are less important as the polynomial degree of the approximation increases. This confirms the observation above on the reduced amount of numerical dissipation introduced by the method as the degree of the discretisation increases and the consequent extra accuracy provided by high-order approximations.

(a) $k = 2$, Mach

(b) $k = 3$, Mach

(c) $k = 4$, Mach

(d) $k = 2$, entropy error

(e) $k = 3$, entropy error
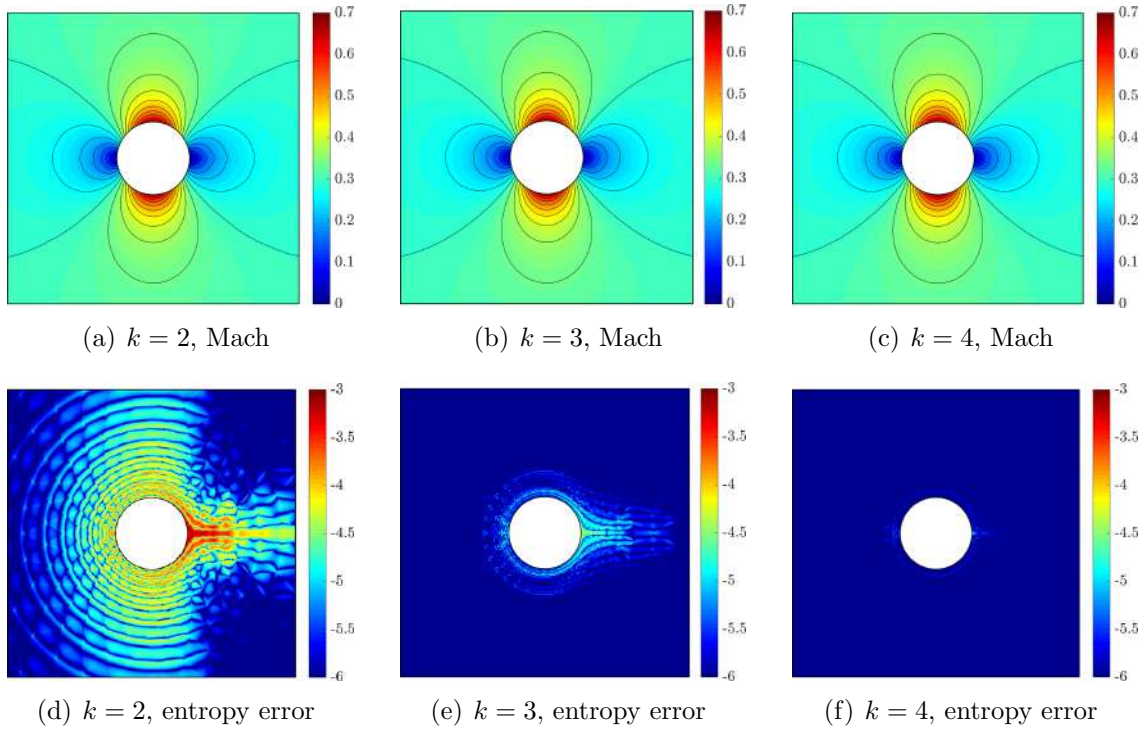
(f) $k = 4$, entropy error

Figure 4.8: Subsonic flow around a cylinder - Mach number distribution and isolines (top) and entropy error in logarithmic scale (bottom) computed on the first mesh using the HLL Riemann solver with $k = 2$ (left), $k = 3$ (middle) and $k = 4$ (right).
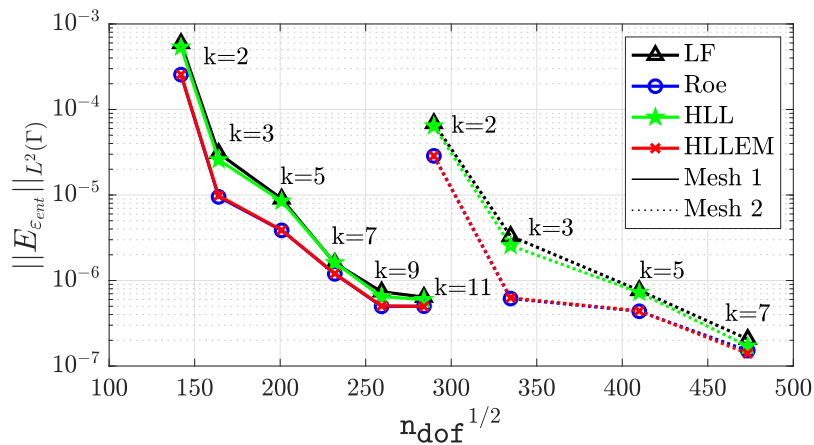
Figure 4.9: Subsonic flow around a cylinder - Entropy error on the cylinder surface for different meshes and different degrees of polynomial approximation.

4.2.2 Boundary layer resolution: subsonic viscous laminar flow over a flat plate

The next example consists of the subsonic laminar flow over a flat plate at zero angle of attack. This classical benchmark follows from the analytical study of boundary layers by Blasius (1908) for incompressible flows and has been commonly used to test laminar flow solvers in resolving boundary layers, such as described by Schlichting and Gersten (2016).

This problem is used to evaluate the numerical diffusion introduced by the different Riemann solvers in the approximation of shear layers and its effect over the boundary layer description.

The example considers a nearly incompressible flow ($M_\infty = 0.1$) at a high Reynolds number ($Re = 10^5$) while preserving a laminar behaviour of the solution along the flat plate.

The computational domain consists of a flat plate of length $5L$, being L the characteristic length of the problem, embedded in a rectangular domain, as shown in figure 4.10. Adiabatic wall conditions are imposed along the plate, whereas symmetry wall conditions are imposed upstream of the leading edge. Subsonic inflow and outflow conditions are imposed at the outer boundaries. The pressure at the outflow is set to p_∞, forcing a zero pressure drop.
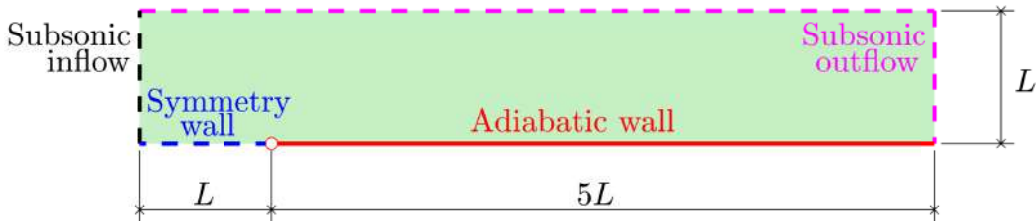
Figure 4.10: Laminar flow over a flat plate - Sketch of the geometry and boundary conditions.

Uniform mesh refinement of the boundary layer is performed in order to analyse the convergence of the solution. Details of the refinement are reported in table 4.2. In particular, for each level of refinement, the number of layers of elements in the boundary layer, $\mathtt{n_{lay}}$, and the number of subdivisions along the flat plate, $\mathtt{n_{div}}$, are doubled and the height h_0 of the first layer is halved. Additionally, h_0 is chosen according to the relation $h_0/k \sim Re^{-0.75}L$. Finally, the geometric growth rate of the

boundary layer, r, is determined in order for the height of the boundary layer mesh
to be $h/L = 0.1$.

Table 4.2: Laminar flow over a flat plate - Mesh refinement details for the convergence
study.

Refinement	n_{lay}	n_{div}	h_0/L	r	n_{el}
1	4	10	$8 \cdot 10^{-4}$	4	501
2	8	20	$4 \cdot 10^{-4}$	2	1,154
3	16	40	$2 \cdot 10^{-4}$	1.4	3,512

The three mesh refinements used for this study are displayed in figure 4.11. Be-
cause of the explicit embedding of the flat plate on the lower boundary of the domain,
a singularity is introduced at the leading edge, as described by Tuck (1991). To alle-
viate its numerical effects, the mesh is further refined at this location.
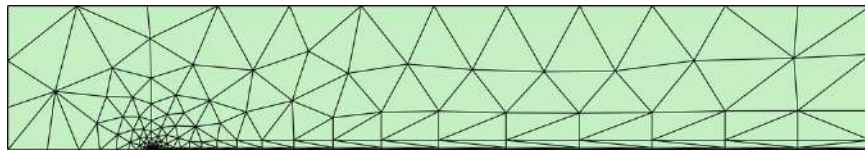
(a) Mesh 1.
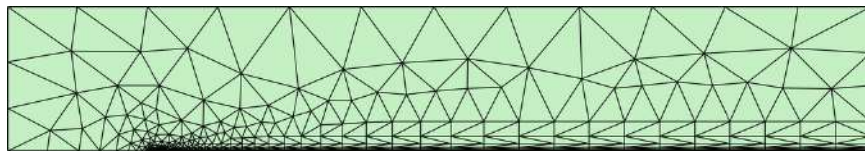
(b) Mesh 2.
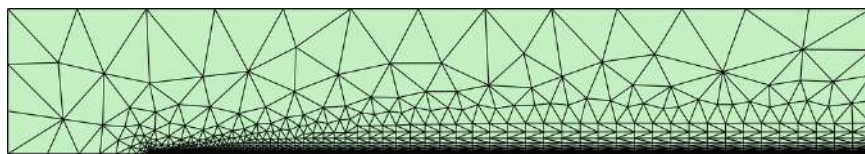
(c) Mesh 3.

Figure 4.11: Laminar flow over a flat plate - Meshes used for the convergence study.

The skin friction coefficient computed in the first level of refinement using degree
of approximation $k = 1$ and $k = 3$ is depicted in figure 4.12 for the different Rie-
mann solvers. The superiority of Roe and HLLEM Riemann solvers with respect to
classical Lax-Friedrichs and HLL is clearly displayed in figure 4.12(a): for low-order
approximations, HLLEM and Roe achieve a better accuracy due to their ability to
capture contact wave-type phenomena and consequently, boundary layer effects by

introducing a lower amount of numerical dissipation. Of course, such difference is reduced when high-order approximations are considered, as the numerical dissipation of the method decreases, see figure 4.12(b).

(a) Mesh 1, $k = 1$ (b) Mesh 1, $k = 3$
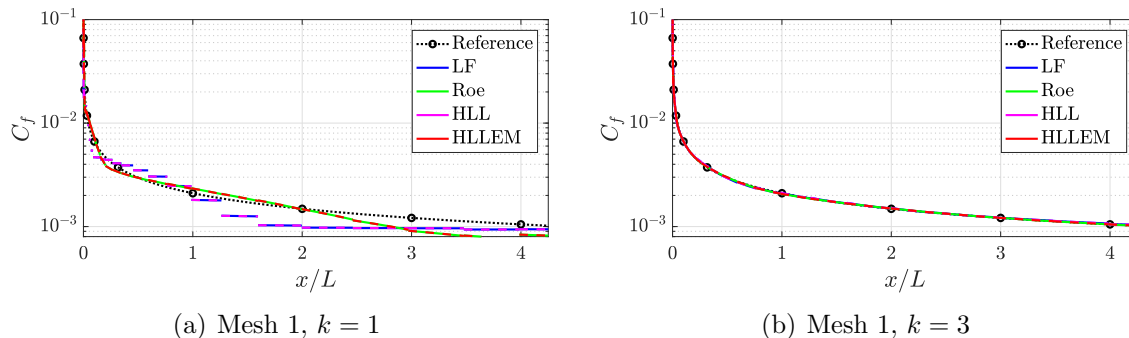
Figure 4.12: Laminar flow over a flat plate - Friction coefficient along the flat plate for different polynomial degrees of approximation in the coarsest mesh, using the Lax-Friedrichs (LF), Roe, HLL and HLLEM Riemann solvers. The reference solution is obtained using the HLLEM Riemann solver on the third mesh, with $k = 4$.

In a similar fashion, velocity profiles along the flat plate and detail of the boundary layer thickness are sketched in figure 4.13 for different degrees of approximation in the different mesh refinements, computed with the HLLEM Riemann solver. The solution is noticeably improved with mesh refinement (figure 4.13, top). It is worth noting that accurate approximations are achieved on the coarsest mesh using high-order polynomial approximation (figure 4.13, bottom).

In order to quantify the effect of the numerical dissipation introduced by the Riemann solver in the quality of the approximate solution, the $\mathcal{L}_2$ error of the boundary layer thickness and of the friction coefficient is measured along the flat plate. The convergence study, shown in figure 4.14, reports the evolution of the error as a function of the number of degrees of freedom, obtained for each mesh by increasing the polynomial degree of approximation from $k = 1$ up to $k = 4$.

The HLLEM solution on mesh 3 using fourth-order polynomials is taken as reference solution for comparison. The results display that Lax-Friedrichs and HLL solutions introduce higher levels of error than HLLEM and Roe. These differences are more remarkable in low order approximations, being the choice of Riemann solver a critical issue for the accuracy of the computation. Furthermore, it is worth noticing that high-order approximations on coarse meshes provide higher accuracy than lower-

(a) Mesh 1, $k = 1$ (b) Mesh 2, $k = 1$ (c) Mesh 3, $k = 1$

(d) Mesh 1, $k = 2$ (e) Mesh 1, $k = 3$ (f) Mesh 1, $k = 4$
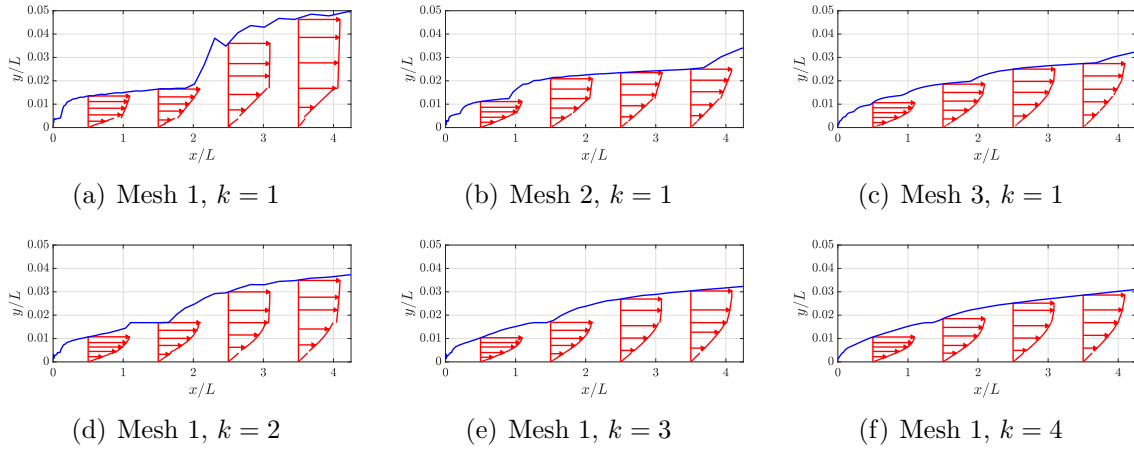
Figure 4.13: Laminar flow over a flat plate - Velocity profiles along the flat plate and boundary layer thickness for the different meshes and polynomial degrees of approximation, using an HLLEM Riemann solver.

(a) Boundary layer thickness, δ (b) Friction coefficient, C_f
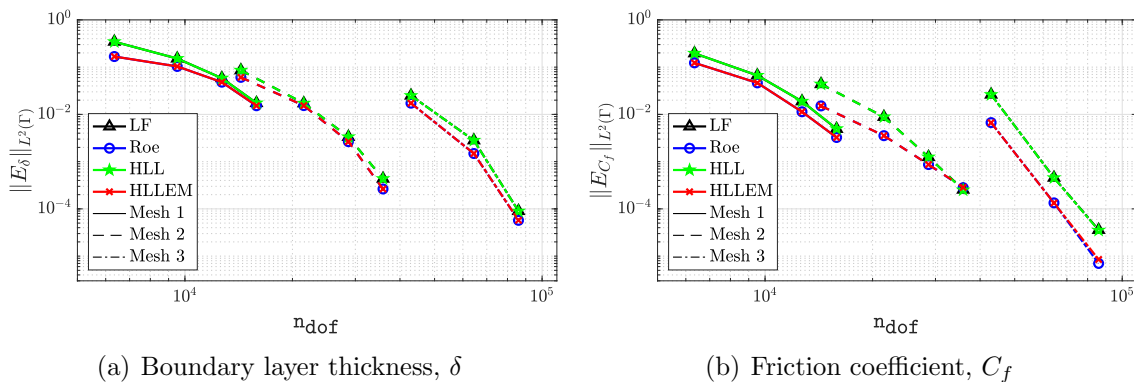
Figure 4.14: Laminar flow over a flat plate - Convergence of the relative $\mathcal{L}_2$ error of the (a) boundary layer thickness and (b) friction coefficient, using Lax-Friedrichs (LF), Roe, HLL and HLLEM Riemann solvers under k-refinement ($k = 1, \ldots, 4$) using three different meshes.

order solutions with similar number of degrees of freedom, emphasising the interest for increasing the polynomial degree of approximation.

Similarly, the convergence of the drag coefficient is reported in figure 4.15. It is confirmed that HLLEM and Roe Riemann solvers display an increased accuracy with respect to Lax-Friedrichs and HLL, which is especially evident for $k = 1$. In this case, even in the coarsest mesh, the drag coefficient computed with HLLEM and Roe solutions lies within the admissible error of five drag counts, contrary to HLL and Lax-Friedrichs. As the degree of approximation increases, differences among Riemann solvers are notably reduced, due to the lower numerical dissipation introduced by

HDG.
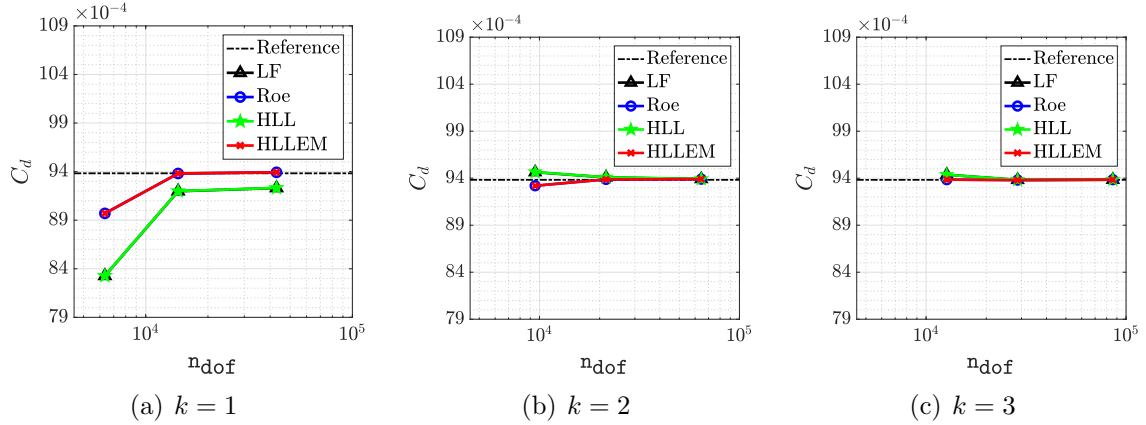
Figure 4.15: Laminar flow over a flat plate - Convergence of the drag coefficient, C_d, using Lax-Friedrichs (LF), Roe, HLL and HLLEM Riemann solvers under h-refinement using three different polynomial degrees of approximation.

Hence, Roe and HLLEM Riemann solvers have proved to be able to resolve the flow solutions in thin boundary layers exhibiting an increased accuracy when low-order approximations are constructed. More precisely, the numerical diffusion introduced by Riemann solvers misrepresenting middle waves (i.e. Lax-Friedrichs and HLL) results critical for an accurate approximation of the solution in the boundary layer and its derived quantities. As the resolution increases, either by mesh refinement or by increasing the polynomial order of approximation, such numerical diffusion is reduced and the differences among Riemann solvers become negligible.

Henceforth, and in order to fully exploit the advantages of the presented HDG solver with the different Riemann solvers, as proved in the previous examples, only high-order approximations are considered.

4.2.3 Shock treatment in inviscid flows: transonic inviscid flow over a NACA 0012 aerofoil

The transonic inviscid flow over a NACA 0012 aerofoil, at free-stream conditions $M_\infty = 0.8$ and angle of attack $\alpha = 1.25°$, is presented to assess the performance of the shock capturing method for inviscid flows. This example is a classical benchmark used to verify numerical inviscid codes and implementations of shock capturing techniques, see for instance Sevilla et al. (2013) or the test case MTC2 in Kroll (2009).
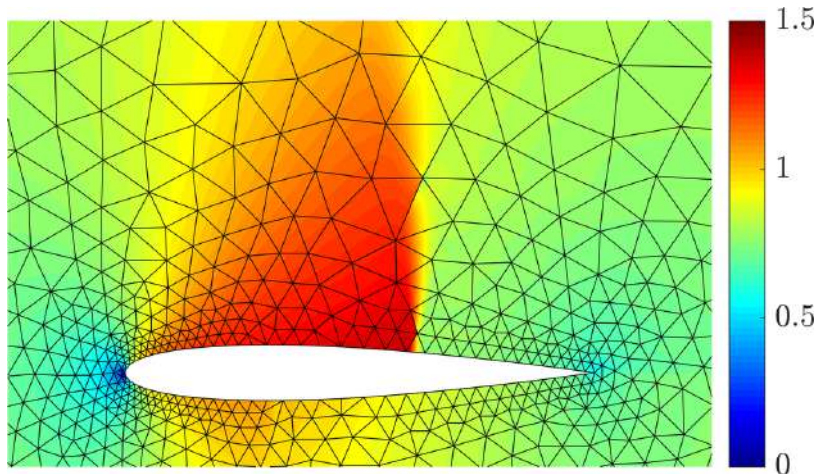
Figure 4.16: Transonic flow over a NACA 0012 aerofoil - Mach number distribution computed using HLL Riemann solver with polynomial degree of approximation $k = 4$.

The steady-state problem is solved via a relaxation approach with a time step $\Delta t = 10^{-1}$ such that the Courant number is $C = 22$. Convergence to the steady-state is achieved when the residual of the steady terms of the continuity equation reaches 10^{-6} or is decreased by three orders of magnitude from its maximum value.

All Riemann solvers are equipped with the Laplacian-based shock capturing technique described in section 3.5.2.2 and the value $\varepsilon_0 = 0.4$ is selected. In the case under analysis, no entropy fix is required by the Roe flux since the artificial viscosity introduced by the shock capturing strategy allows the Riemann solver to fulfill the entropy conditions. Nonetheless, it is worth remarking that the need of an entropy fix is not known *a priori* and the value of the corresponding parameter δ depends upon the problem and requires to be appropriately tuned by the user. More details will be provided in section 4.2.4 for the case of a supersonic flow over the NACA 0012 aerofoil.

A mesh with $1,877$ triangular elements, without any specific refinement in the shock region, is used and an approximation degree $k = 4$ is considered. The far-field boundary is placed 10 chord units away from the aerofoil.

Figure 4.16 displays the Mach number distribution computed using the HLL Riemann solver. An accurate description of the flow around the aerofoil is obtained and the shock is precisely captured with a coarse mesh, owing to the high-order polynomial approximation constructed using the HDG framework and the shock capturing term introduced. The resolution of the shock is clearly related to the local mesh

size and sharper representations may be obtained by performing local mesh refinement in the shock region, as described by Nguyen and Peraire (2011). Comparable results, not reported here for brevity, were obtained by the proposed HDG method with Lax-Friedrichs, Roe and HLLEM Riemann solvers.

The accuracy of the different numerical fluxes is thus evaluated comparing the pressure coefficient, given by

$$C_p = \frac{p - p_\infty}{0.5\rho_\infty v_\infty^2}, \tag{4.9}$$

over the aerofoil profile.
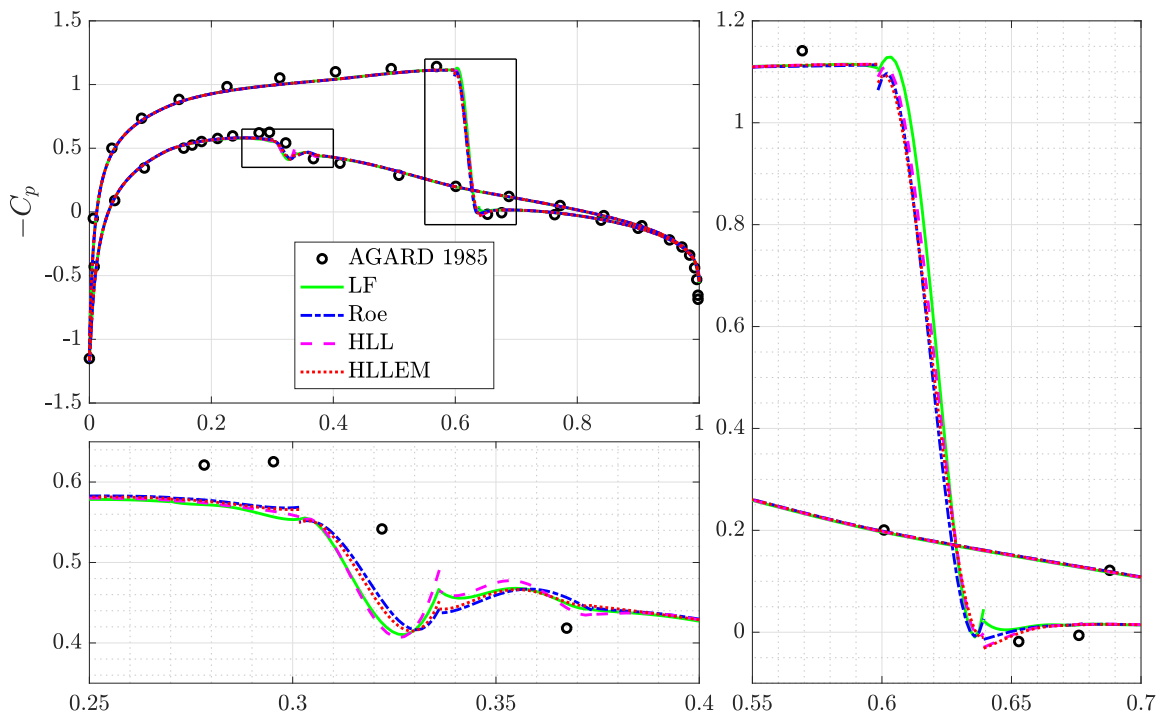
Figure 4.17: Transonic flow over a NACA 0012 aerofoil - Pressure coefficient around the aerofoil surface computed using different Riemann solvers with polynomial degree of approximation $k = 4$ and detailed views of the lower (left) and upper (right) shocks.

A well resolved solution, in agreement with the experimental data by Yoshihara and Sacher (1985), is obtained using all Riemann solvers. The results in figure 4.17 display that HLL and HLLEM Riemann solvers provide an approximation without oscillations and with accuracy similar to the one of the Roe numerical flux near the upper, stronger shock. It is worth noting that the jumps appearing at the extrema of the shock region are due to the discontinuous nature of the HDG approximation.

The lower, weaker shock, is reproduced less precisely by the four Riemann solvers. In this case, HLL presents a behaviour closer to the Lax-Friedrichs solution, whereas HLLEM and Roe produce a similar approximation.

Accordingly, the lift and drag coefficients reported in table 4.3 allow to quantify very little differences among Riemann solvers.

Table 4.3: Transonic inviscid flow over a NACA 0012 aerofoil - Lift and drag coefficients for different Riemann solvers using a polynomial degree of approximation $k = 4$.

	Lax-Friedrichs	Roe	HLL	HLLEM
C_l	0.320	0.314	0.317	0.315
C_d	0.0193	0.0190	0.0192	0.0191

The obtained values lie between 25 and 35 lift and drag counts with respect to typical reference values provided by Thibert et al. (1979). Note that the precision of the aerodynamic coefficients is strongly dependent on the location of the far-field boundary, as reported by Yano and Darmofal (2012) or Wang et al. (2013). In particular, for such kind of comparisons, far-field boundaries are tipically located at distances from 50 up to 10^4 chord lengths from the aerofoil, as concluded by Woopen et al. (2014), Balan et al. (2015) or Ekelschot et al. (2017).

Finally, the entropy production is considered for this non-isentropic case. In this context, such quantity allows to estimate the numerical dissipation introduced in the upstream region before the shock and the entropy produced by the artificial viscosity.

On the one hand, the results in figure 4.18 show that the regions of activation of the sensor are almost identical for the four Riemann solvers. On the other hand, the different amount of numerical dissipation introduced by the numerical fluxes is responsible for the production of entropy. As observed in figure 4.17, HLL, HLLEM and Roe Riemann solvers present a similar behaviour in the vicinity of the upper, stronger shock, where comparable approximations are achieved. On the contrary, the Lax-Friedrichs numerical flux introduces the largest amount of numerical dissipation in this region, as shown in figure 4.18(f). In the vicinity of the weaker shock on the lower part of the aerofoil, the four Riemann solvers show a similar entropy production. Finally, Roe and HLLEM solvers provide the most accurate results in the region near the trailing edge, where the HLL and the Lax-Friedrichs numerical fluxes introduce extra dissipation.

(a) HLL, sensor activation

(b) HLL, entropy production

(c) HLLEM, sensor activation

(d) HLLEM, entropy production

(e) LF, sensor activation

(f) LF, entropy production

(g) Roe, sensor activation

(h) Roe, entropy production
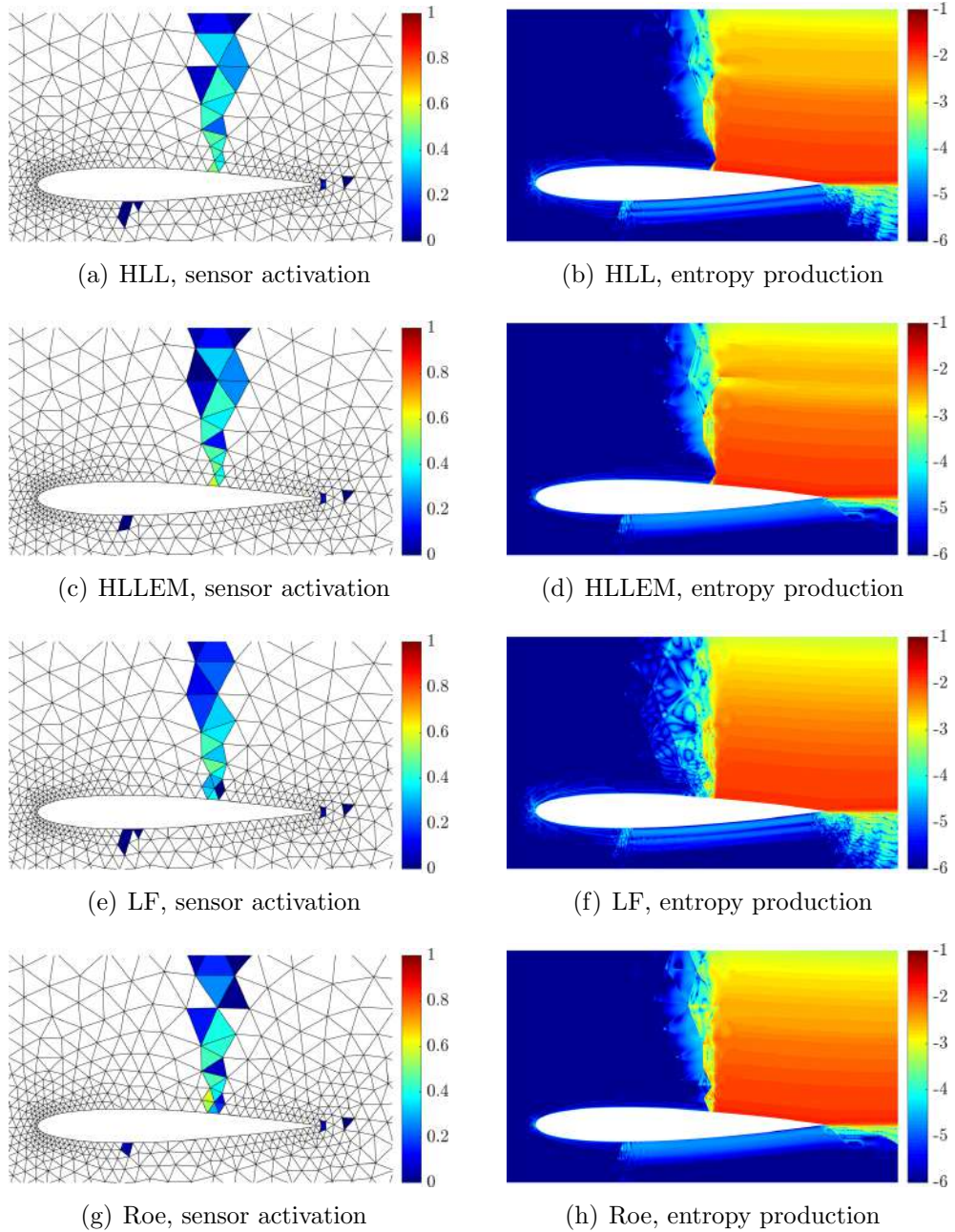
Figure 4.18: Transonic flow over a NACA 0012 aerofoil - Regions of activation of the shock sensor (left) and entropy production in logarithmic scale (right) for HLL (a-b), HLLEM(c-d), Lax-Friedrichs (LF, e-f) and Roe (g-h) Riemann solvers using a polynomial degree of approximation $k = 4$.

This example demonstrates an overall good performance of the Laplacian-based shock capturing method for inviscid compressible flows. Furthermore, no significant differences are observed among the Riemann solvers using a high-order approximation of order $k = 4$. In particular, the four numerical fluxes lead to similar approximate solutions, as reported with the aerodynamic measures of lift, drag and pressure coefficients, while displaying an accurate and positively conservative treatment of the shock waves.

4.2.4 Positivity-preserving properties in presence of shocks: supersonic inviscid flow over a NACA 0012 aerofoil

The second example of inviscid flow around a NACA 0012 aerofoil consists of a supersonic flow at a free-stream Mach number $M_\infty = 1.5$ and zero angle of attack, also studied by Persson and Peraire (2006) or Balan et al. (2015).

This supersonic test case challenges the performance of the proposed Riemann solvers in HDG in capturing solutions involving shocks and sharp gradients while ensuring positivity-preserving properties using high-order approximations. It is worth noticing that, in such case, Riemann solvers may fail to provide physically admissible solutions, leading to a violation of the positiveness of the approximate density and pressure fields, according to Peery and Imlay (1988), Quirk (1994) or Fleischmann et al. (2019).

The computational mesh described in the previous case 4.2.3, consisting of 1,877 triangular elements and a far-field boundary placed at 10 chord units away from the aerofoil, is employed for the simulation. A time step $\Delta t = 8 \times 10^{-2}$ is considered to advance in time and the corresponding Courant number is $C = 20$. Convergence to the steady-state is achieved when the residual of the steady terms of the continuity equation reaches 10^{-6} or is decreased by three orders of magnitude from its maximum value. The shock treatment is handled by means of the Laplacian-based technique discussed in section 3.5.2.2, with a maximum value of artificial viscosity $\varepsilon_0 = 1$.

The Mach number distribution computed using the HLL Riemann solver with a polynomial degree of approximation $k = 4$ is presented in figure 4.19. The method is able to accurately capture the physics of the problem, even on a coarse mesh, owing to the high-order functional discretisation introduced by the HDG scheme.

This supersonic problem is especially challenging since it features an abrupt shock in front of the aerofoil and allows to test the positivity properties of the approximate
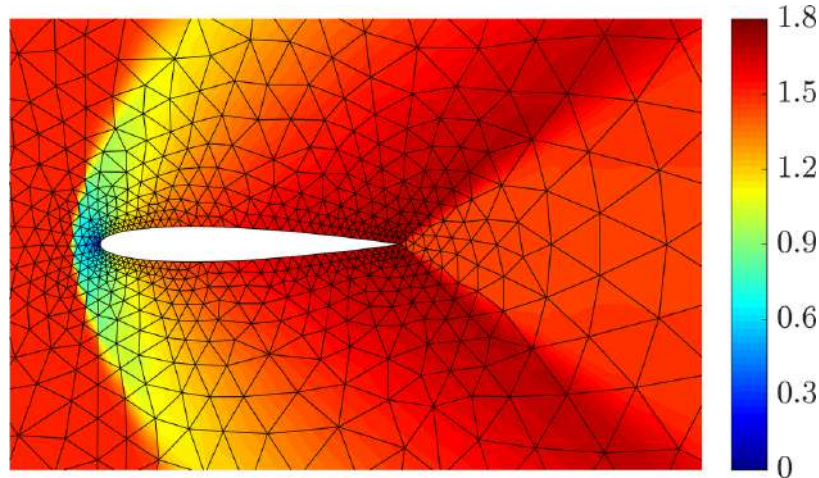
Figure 4.19: Supersonic flow over a NACA 0012 aerofoil - Mach number distribution computed using an HLL Riemann solver with polynomial degree of approximation $k = 4$.

solution. For this purpose, the performance of the Roe Riemann solver is compared with those of the HLL family. Figure 4.20 shows the minimum nodal value of the pressure computed using the Roe numerical flux with different values of the HH entropy fix as well as with HLL and HLLEM.
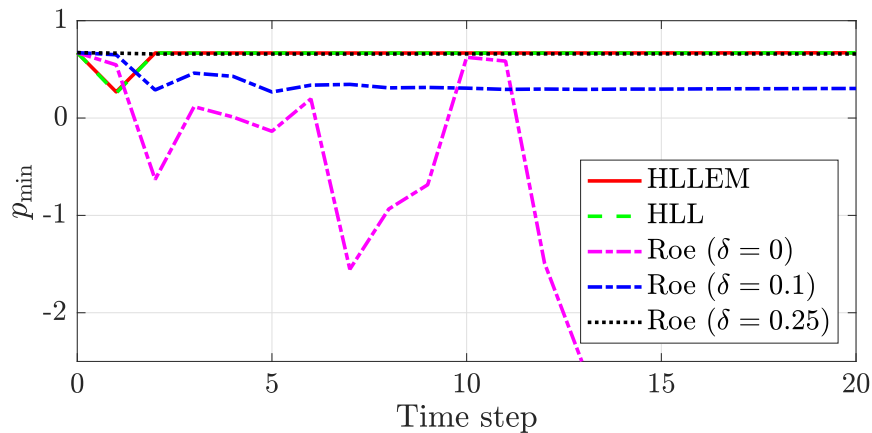
Figure 4.20: Supersonic flow over a NACA 0012 aerofoil - Minimum nodal value of the pressure computed using the different Riemann solvers with polynomial degree of approximation $k = 4$.

In the case with no entropy fix ($\delta = 0$), the Roe solver displays an insufficient numerical dissipation. After few iterations, negative values of the pressure are computed, leading to a nonphysical solution. This error is amplified from one time step to the following ones and rapidly leads to the divergence of the Newton-Raphson algorithm employed to solve the nonlinear problem. To remedy this issue, inherent

to the Roe Riemann solver, an HH entropy fix with an empirically tuned value of the threshold parameter δ is considered. It is worth emphasising that the tuning of such parameter is problem-dependent. With a setting of $\delta = 0.1$, the HDG method with Roe Riemann solver converges to a steady-state solution including some nonphysical undershoots in the pressure and density fields, giving rise to overshoots in the Mach distribution.

(a) HLL, Mach

(b) HLL, artificial viscosity

(c) Roe HH-EF $\delta = 0.1$, Mach

(d) Roe HH-EF $\delta = 0.1$, artificial viscosity
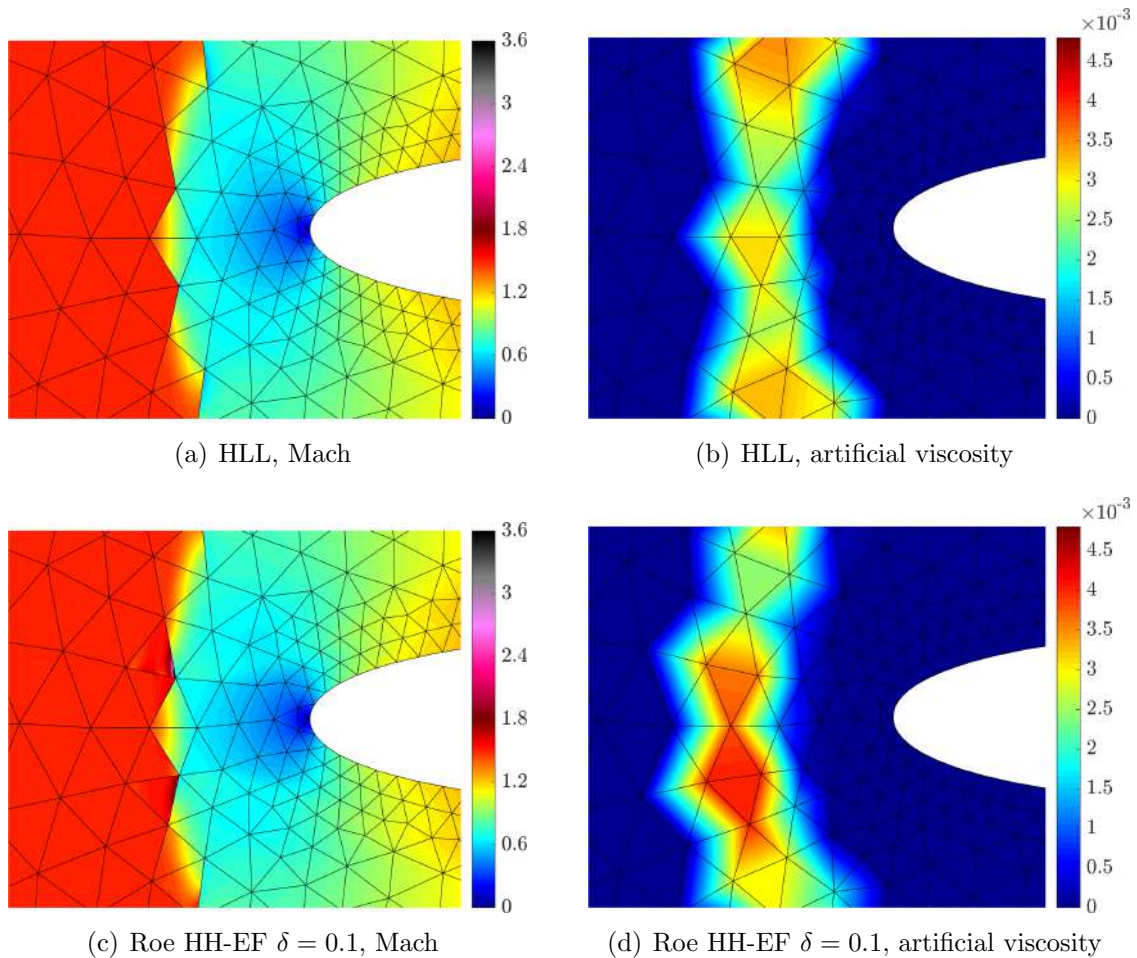
Figure 4.21: Supersonic flow over a NACA 0012 aerofoil - Detail of the Mach number distribution (left) and corresponding artificial viscosity (right) in the front shock near the leading edge computed using HLL (top) and Roe Riemann solver with HH entropy fix with threshold parameter $\delta = 0.1$ (bottom) with polynomial degree of approximation $k = 4$.

Precisely, the corresponding Mach number distribution computed using the Roe numerical flux with entropy fix parameter $\delta = 0.1$ is reported in figure 4.21 to illustrate such spurious oscillations appearing in the region in front of the shock

(Fig. 4.21(c)). Such oscillations appear despite the artificial viscosity introduced in the corresponding elements, as displayed in figure 4.21(d). Hence, this value of the HH entropy fix parameter leads to insufficient stabilisation and a higher threshold needs to be introduced.

Remark 4.2. It is worth noting that the colour scale of figure 4.21 keeps the same gradation of colours of figure 4.19 for the interval $M \in [0, 1.8]$ but extends up to $M = 3.6$ to visualise the peak values achieved by the overshoots in the Roe solution.

Such numerical issues are fixed by increasing the threshold value δ of the HH entropy fix. Numerical results showed that a value $\delta = 0.25$ or larger allows the high-order HDG solver to achieve a physically admissible solution with no overshoots, as reported in figure 4.20. Nonetheless, in case of exceeding the threshold value of the entropy fix, the associated numerical dissipation of the Roe Riemann solver is increased, turning the solver overdiffusive. In the limit, $\delta \to \lambda_{\mathtt{max}}$, the Lax-Friedrichs Riemann solver is obtained. On the contrary, HLL and HLLEM numerical fluxes provide a robust approximation with no oscillations without the need of any user-defined entropy fix.

The entropy production is then examined for this non-isentropic case. In this context, such quantity allows to estimate the numerical dissipation introduced in the upstream region before the shock and the entropy produced by the artificial viscosity. The map of the entropy production is reported in figure 4.22 for the HLL, HLLEM and Lax-Friedrichs numerical fluxes. The results display that HLL-type Riemann solvers introduce a limited amount of numerical dissipation in the vicinity of the front shock. On the contrary, the Lax-Friedrichs solver is responsible for a large entropy production in the shock region, confirming its over-diffusive nature also in supersonic problems. Figure 4.22 also confirms that the shock-capturing sensor is activated in the same regions independently on the Riemann solver considered.

Finally, the accuracy of the approximate solutions corresponding to the different Riemann solvers is quantitatively evaluated with respect to the error in the lift coefficient. It is well-known that a symmetric aerofoil subject to a flow at zero angle of attack produces no lift force. Table 4.4 gathers the lift coefficient computed with the different Riemann solvers. The HLL-type numerical fluxes, i.e., HLL and HLLEM, are the most accurate in such computation, with a lift coefficient laying at 5 and 6 lift counts from the reference value, respectively. Both the lift coefficient computed by

(a) HLL, sensor activation   (b) HLLEM, sensor activation   (c) LF, sensor activation

(d) HLL, entropy production   (e) HLLEM, entropy produc-   (f) LF, entropy production
                                     tion
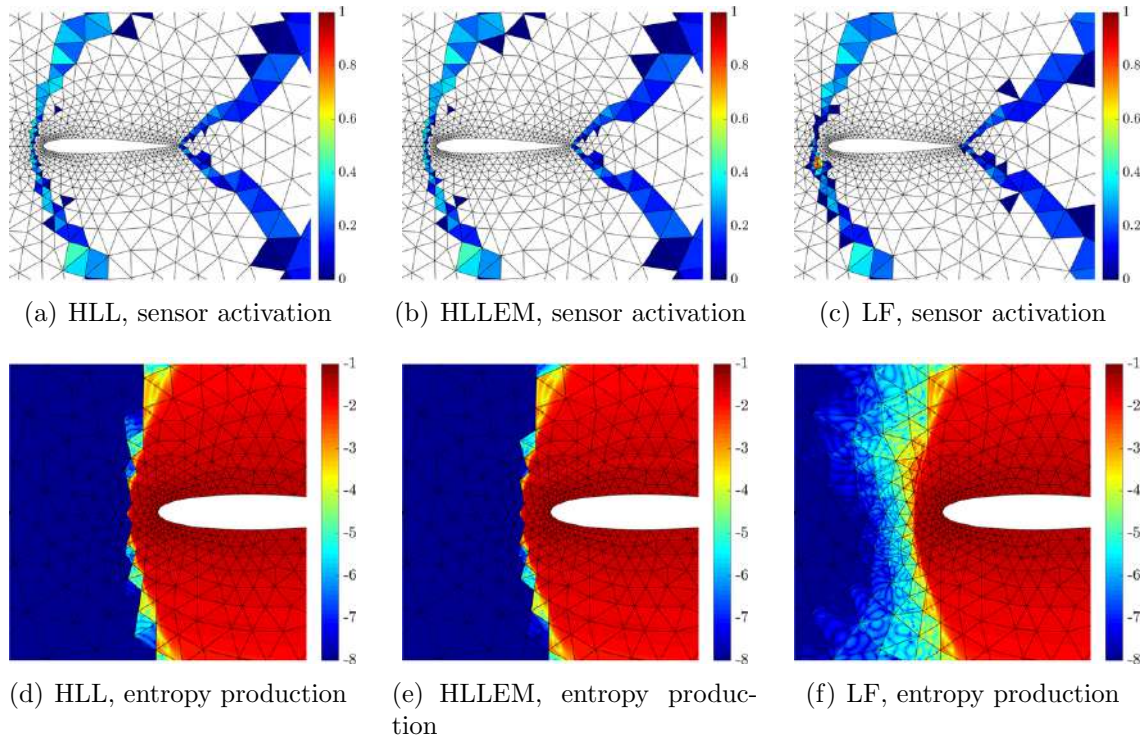
Figure 4.22: Supersonic flow over a NACA 0012 aerofoil - Regions of activation of the shock sensor (top) and entropy production in logarithmic scale (bottom) for HLL (left), HLLEM (middle) and Lax-Friedrichs (LF, right) Riemann solvers using polynomial degree of approximation $k = 4$.

Roe with an entropy fix $\delta = 0.25$ and by Lax-Friedrichs (LF) feature a higher error of 8 lift counts with respect to the reference value.

Table 4.4: Supersonic inviscid flow over a NACA 0012 aerofoil - Lift coefficient for different Riemann solvers using a polynomial degree of approximation $k = 4$.

	Reference	Lax-Friedrichs	Roe ($\delta = 0.25$)	HLL	HLLEM
C_l	0	-0.008	-0.008	-0.005	-0.006

This example involving a strong shock wave illustrates the ability of HLL-type Riemann solvers, such as HLL and HLLEM, of guaranteeing positivity and thus producing physically admissible solutions in a robust and parameter-free strategy, in contrast with Roe Riemann solver.

4.2.5 Shock wave/boundary layer interaction

The first example of this type considers the strong interaction between a shock wave and a laminar boundary layer. Such interaction is a basic phenomenon of viscous-inviscid interaction that happens when a shock impinges on the boundary layer producing separation in it. In such a case, the shock, instead of reflecting off the wall, turns into a combination of an expansion fan at the edge of the boundary layer plus two compression waves around the separation and reattachment points, as described by Hakkinen et al. (1959) and Katzer (1989).

The setup of this test case replicates the one introduced by Degrez et al. (1987) and later reproduced by Moro et al. (2017) using a high-order HDG discretisation with $k = 3$. It consists of a flat plate and a shock generator mounted inside a stream at $M_\infty = 2.15$ and $Re = 10^5$. A sketch of the geometry for a characteristic length of $L = 1$ and the corresponding boundary conditions are detailed in figure 4.23. It is worth noticing that a fillet is introduced at the leading edge in order to avoid the singularity at this location.
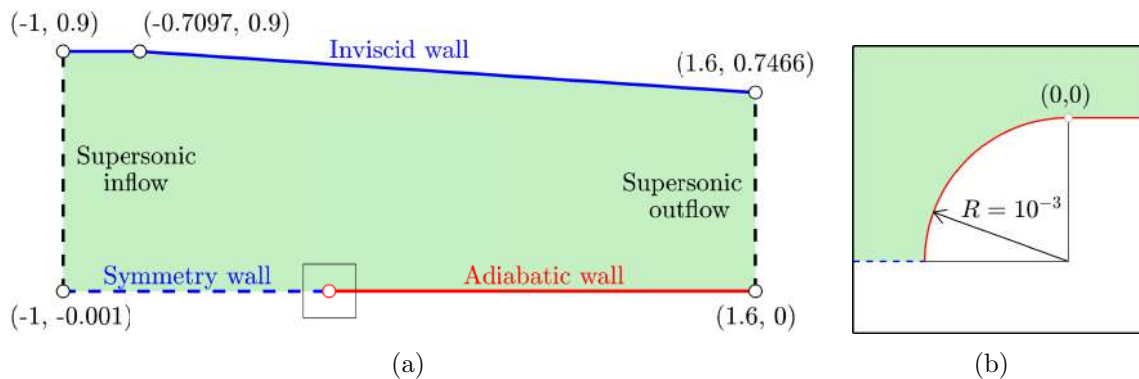
Figure 4.23: Shock wave/boundary layer interaction - (a) Geometry and boundary conditions and (b) detail of the fillet at the leading edge.

The computational mesh, depicted in figure 4.24, is composed of 3,379 triangular elements of degree $k = 3$. The boundary layer mesh consists of $\mathtt{n_{lay}} = 12$ layers of elements with a growing rate $r = 1.4$ and the first layer located at a height of $h_0/L = 2.5 \cdot 10^{-4}$. In addition, the mesh is refined at the leading edge and $\mathtt{n_{div}} = 80$ divisions are defined along the plate.

The simulation is performed using the HLLEM Riemann solver due to its positivity-preserving properties in presence of shocks, contrary to Roe, and its superiority with respect to HLL or Lax-Friedrichs in resolving boundary layers. The physics-based
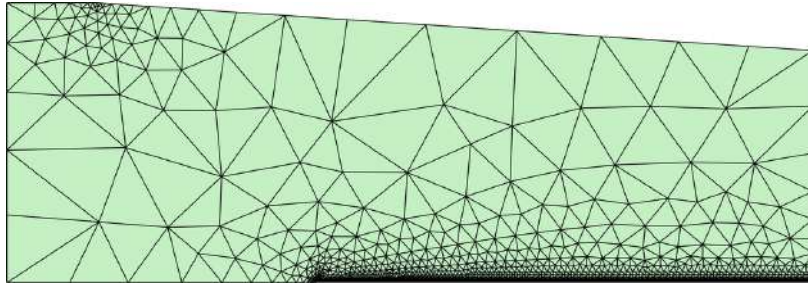
Figure 4.24: Shock wave/boundary layer interaction - Computational mesh.

shock treatment involving an artificial bulk viscosity described in section 3.5.2.1 is employed. The resulting flowfield is depicted in figure 4.25. The presence of shocks generated at different locations as well as the effect of the strong shock wave/boundary layer interaction can be observed.
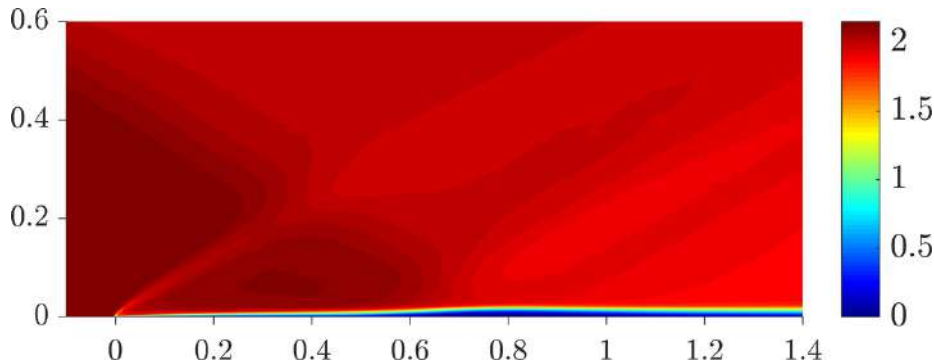
Figure 4.25: Shock wave/boundary layer interaction - Mach number distribution obtained with the HLLEM Riemann solver and polynomial degree of approximation $k = 3$.

Detail of the impingement region showing the separation bubble induced by the interaction between the reflecting shock wave and the boundary layer is illustrated in figure 4.26.

Finally, figure 4.27 displays a comparison of the pressure coefficient and the skin friction coefficient computed using the HLLEM Riemann solver with benchmark results by Degrez et al. (1987) and Moro et al. (2017).

The computed pressure and skin friction coefficients show excellent agreement with both the experimental curve by Degrez et al. (1987) and the numerical solution by Moro et al. (2017), whereas the numerical curve by Degrez et al. (1987) deviates from the rest of results, especially downstream of the separation bubble. The HLLEM computed solution lies on top of the reference results except for the region of shock impingement, where the highly anisotropic adapted meshes by Moro et al. (2017)
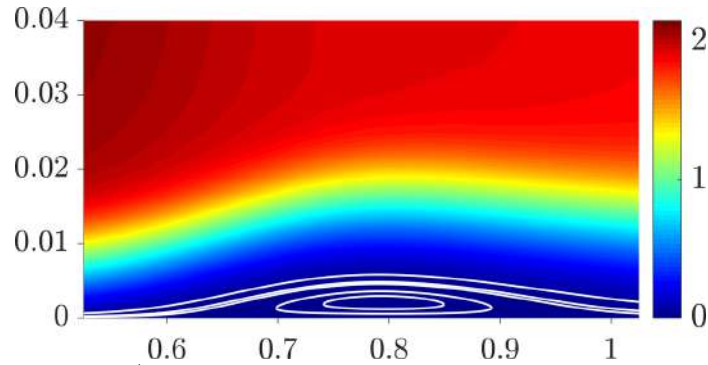
Figure 4.26: Shock wave/boundary layer interaction - Detail of the shock-induced sepa-
ration bubble in the Mach flowfield depicted in figure 4.25. Isolines of the
Mach are drawn in white.

(a) Pressure coefficient

(b) Friction coefficient
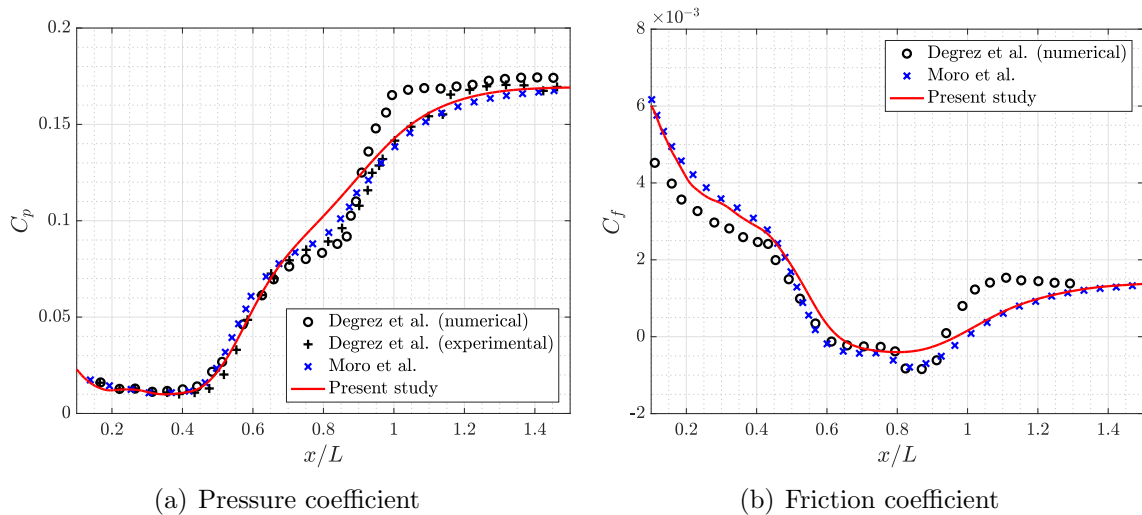
Figure 4.27: Shock wave/boundary layer interaction - Pressure (a) and friction (b) coef-
ficients along the flat plate using the HLLEM Riemann solver and order of
polynomial approximation $k = 3$.

outperform the presented results. It is worth recalling that the HLLEM simulation in
this study is performed on a mesh with no a priori refinement except for the boundary
layer regions and the leading edge point.

This test case demonstrates a good behaviour of the HLLEM Riemann solver not
only in the resolution of the boundary layer or in the treatment of shock waves in high-
order but also in the strong interaction of these two flow features which challenges
the performance of Riemann solvers.

4.2.6   Supersonic flow over a compression corner

The last case presented in this study considers the $M_\infty = 3$ supersonic flow over a 10° compression corner. This example represents a classical benchmark for viscous laminar compressible flow, first introduced by Carter (1972) and later reproduced by several authors, such as Hung and MacCormack (1976), Shakib et al. (1991), Aliabadi et al. (1993), Mittal and Yadav (2001) Qamar et al. (2006), or Kotteda and Mittal (2014).

The setup of this problem consists of a laminar flow at $Re = 16,800$ over an isothermal flat plate of length L (the characteristic length of the problem) ended with a 10° wedge. The isothermal surface is kept at the free-stream stagnation temperature, namely

$$T_w = T_{\infty,0} = \frac{1}{(\gamma - 1)M_\infty^2} \left(1 + \frac{\gamma - 1}{2} M_\infty^2 \right). \tag{4.10}$$

A sketch of the geometry and detail of the corresponding boundary conditions is depicted in figure 4.28.
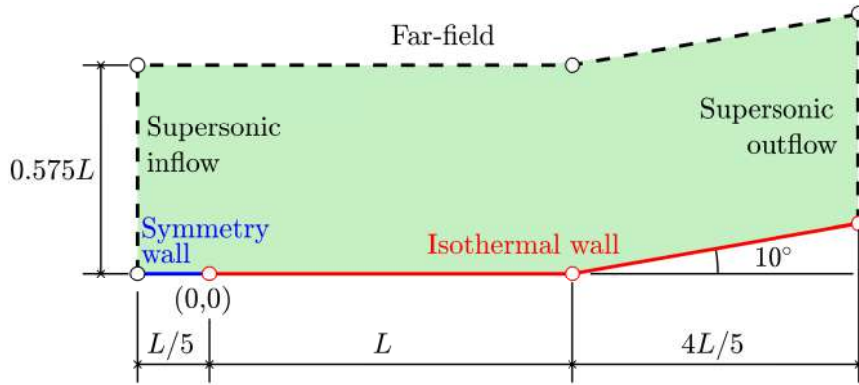
Figure 4.28: Supersonic flow over a compression corner - Sketch of the geometry and boundary conditions.

The computational domain is discretised with 2,773 triangular elements of degree $k = 3$, as illustrated in 4.29. In contrast to the shock wave/boundary layer interaction example, the leading edge of the flat plate is not rounded by means of a fillet, thus introducing a singularity. Such singular behaviour is alleviated by means of further refinement and by reducing the order of polynomial approximation to $k = 2$ in the elements surrounding the singularity, as depicted in red in 4.29(b).

The boundary layer mesh consists of $n_{lay} = 12$ layers of elements with the first layer located at a height of $h_0/L = 5 \cdot 10^{-4}$ and a growing rate of $r = 1.4$. The isothermal wall is divided into $n_{div} = 72$ elements.

(a)

(b)
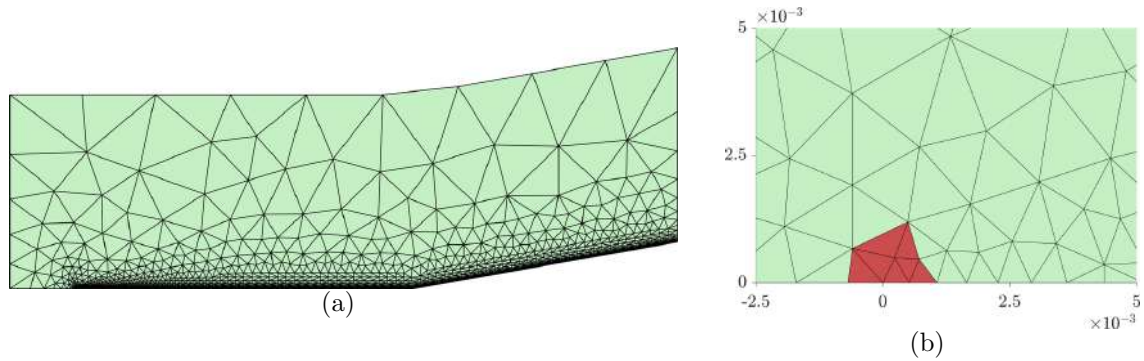
Figure 4.29: Supersonic flow over a compression corner - (a) Computational mesh and (b) detail of the leading edge, showing in red the elements employing a lower degree of approximation, $k = 2$.

The physics-based shock capturing based on artificial bulk viscosity described in 3.5.2.1 is employed for the simulation. The resulting flowfield obtained with the HLLEM Riemann solver is presented in figure 4.30. The density field in figure 4.30 illustrates the regions of high compression, namely the shock wave generated at the leading edge and the compression fan induced by the wedge.

Good resolution of the flow solution can be observed in figure 4.31, where the separation bubble induced by the corner is depicted.

A qualitative comparison of the obtained results is carried out through the wall pressure and the skin friction coefficient. Figure 4.32 compares such quantities with respect to the reference results by Carter (1972) and Hung and MacCormack (1976), showing an excellent agreement. Additional numerical results available in the literature such as those by Shakib et al. (1991), Aliabadi et al. (1993), Mittal and Yadav (2001), Qamar et al. (2006) and Kotteda and Mittal (2014) are not included in the comparison for the sake of readability because of the similarity among them.

Finally, the position of the separation, x_s, and reattachment, x_r, points, gathered in table 4.5, allows a quantitative assessment of the computed solution.

The obtained results show a strong consistency with respect to those available in the literature, proving the good performance of the high-order HDG solver.

(a) Density

(b) Mach
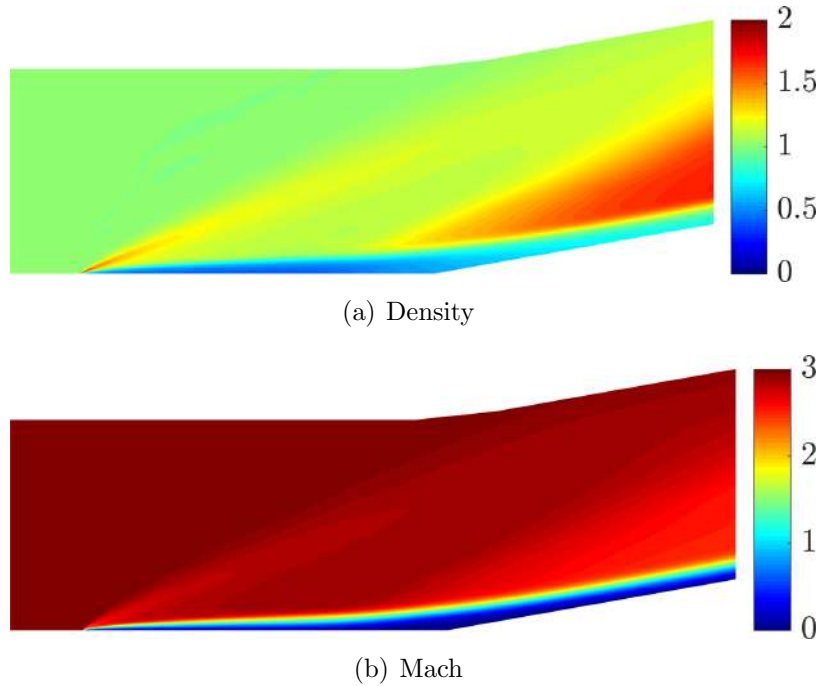
Figure 4.30: Supersonic flow over a compression corner - Density (a) and Mach number (b) distributions using the HLLEM Riemann solver with a combined polynomial degree of approximation $k = 2$ and $k = 3$.
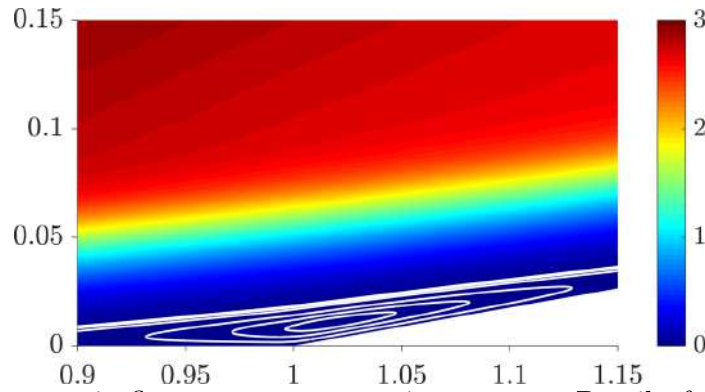
Figure 4.31: Supersonic flow over a compression corner - Detail of the Mach number distribution around around the corner, using the HLLEM Riemann solver with a combined polynomial degree of approximation $k = 2$ and $k = 3$. Isolines of the Mach are drawn in white.

4.3 Conclusions

Optimal convergence properties of the HDG discretisation have been verified using Lax-Friedrichs, Roe, HLL and HLLEM Riemann solvers both for inviscid and viscous cases and for a wide range of the Reynolds number. HDG demonstrates its ability to

(a) Pressure

(b) Friction coefficient
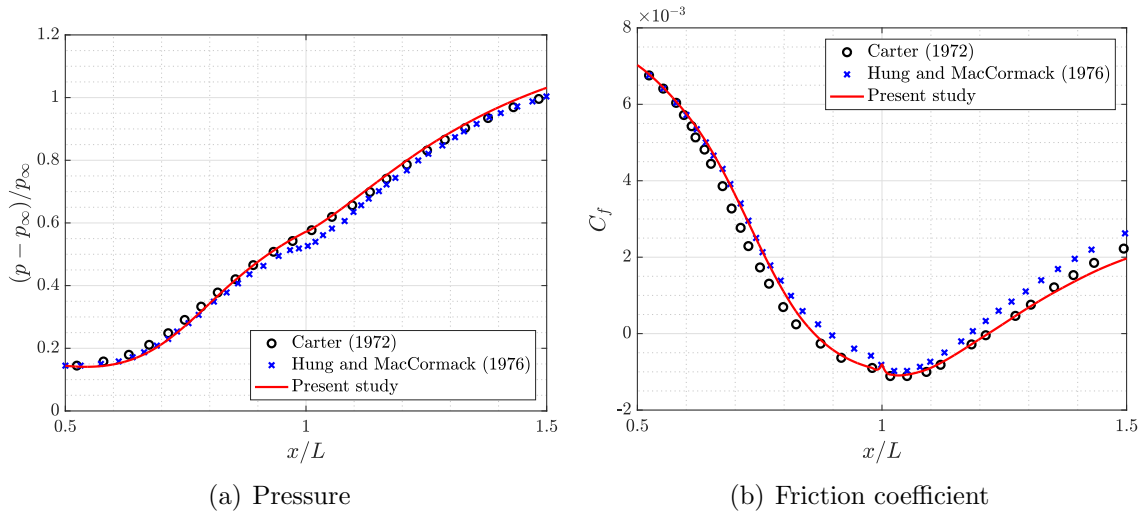
Figure 4.32: Supersonic flow over a compression corner - Pressure (a) and friction coefficient (b) along the flat plate using the HLLEM Riemann solver with a combined polynomial degree of approximation $k = 2$ and $k = 3$.

Table 4.5: Supersonic flow over a compression corner - Position of the separation, x_s, and reattachment, x_r, points around the wall.

Reference	x_s/x_c	x_r/x_c
Present study	0.86	1.20
Carter (1972)	0.84	1.22
Hung and MacCormack (1976)	0.89	1.18
Shakib et al. (1991)	0.88	1.17
Mittal and Yadav (2001)	0.89	1.13
Kotteda and Mittal (2014)	0.88	1.17

approximate the conserved quantities as well as the viscous stress and the heat flux with optimal order of convergence, $k + 1$.

Whereas the role of the Riemann solver shows little effect in the precision of the approximate primal variables, significant differences are noticed in the precision of the approximated mixed variables. In particular, HLLEM and Roe Riemann solvers yield a gain in accuracy in the approximation of the heat flux and viscous stress, specially as the Reynolds number increases.

Then, a set of 2D numerical benchmarks has been presented to show the advantages of high-order approximations for compressible flow problems and the capabilities of the novel HLL and HLLEM Riemann solvers in different flow regimes, from subsonic to supersonic, with special attention to its comparison with well-established

Lax-Friedrichs and Roe Riemann solvers in the context of HDG.

In particular, HLL-type Riemann solvers exhibit a superior performance in supersonic cases, illustrating their positivity preserving properties. This allows a robust and parameter-free strategy in the solution of supersonic flows involving shock waves, contrary to Roe Riemann solver, which may fail to produce physically admissible solutions because of a lack of dissipation. Furthermore, HLLEM Riemann solver demonstrates its ability to preserve contact or shear layers, likewise Roe, producing results that introduce less numerical dissipation than HLL and Lax-Friedrichs, and displaying a major advantage in the approximation of boundary layers.

Finally, a couple of benchmarks involving the interaction of boundary layers and shock waves demonstrate the overall good performance of the high-order HDG method, equipped with a shock-capturing technique based on artificial viscosity and an HLLEM Riemann solver, in the resolution of problems with such combination of viscous and inviscid-type phenomena.

Chapter 5

Summary and future developments

This thesis has presented a series of developments in the context of hybridised numerical methods, with the aim of devising a robust and efficient framework for the high-fidelity simulation of compressible flows. Based on the current duality within CFD between low-order and high-order discretisation methods, the scope of this work has been set up in both of these levels. To this end, on the one hand, a novel low-order strategy consisting of the introduction of a mixed hybrid finite volume method for the simulation of steady-state compressible flows has been presented. On the other, in the line of enhancing the robustness of current high-order approaches, a suitable framework for the derivation of Riemann solvers for the HDG method has been introduced, allowing the formulation of the HLL and HLLEM numerical fluxes.

This chapter outlines the principal contributions stemming from this thesis and describes some open topics that could configure future research lines.

5.1 Summary and contributions

The main contributions of this thesis are summarised as follows.

1. **Formulation of the HDG method for compressible flows with symmetry enforcement of the stress tensor.**
   This thesis presents a review of the formulation of inviscid and viscous com-

pressible flows, i.e. the Euler and the compressible Navier-Stokes equations, in the context of high-order hybridised discontinuous Galerkin methods. The high-order method is equipped with two different shock capturing strategies based on artificial viscosity for the handling of sharp fronts of the flow. On the one hand, a physics-based shock capturing method is employed for viscous flows whereas a smoothness indicator combined with a Laplacian-based strategy that does not require the introduction of mixed variables is considered for inviscid cases.

The present formulation of the compressible Navier-Stokes equations introduces a new choice for the mixed variables employed to describe the viscous flux tensor. Indeed, contrary to common approaches that introduce the gradient of the conservation variables, the deviatoric strain rate tensor and the temperature gradient are considered in this work. Such election for the mixed variables allows to impose pointwise the symmetry of the stress tensor with reduced computational cost while retrieving optimal accuracy.

2. **Presentation of HLL-type Riemann solvers for hybridised formulations, derived under the unified framework for the expression of numerical fluxes in HDG.**
The treatment of convective numerical fluxes in HDG has been thoroughly studied in this thesis. Indeed, a unified framework for the derivation of Riemann solvers in the context of hybridised methods has been presented. To this effect, different approximate Riemann solvers popularly employed in DG formulations have been extended to the hybrid setting. According to the HDG rationale, the information of the Riemann solver is encapsulated within the HDG stabilisation term, whereas the hybrid variable of the formulation is exploited acting as intermediate state.

Such framework includes the traditional Lax-Friedrichs and Roe solvers, already formulated in HDG, and proposes for the first time in hybridised formulations the HLL and HLLEM numerical fluxes. HLL-type Riemann solvers demonstrate their superior performance in transonic and supersonic cases with respect to the Roe flux, which may fail to satisfy entropy conditions, leading to a non-physical approximation of the solution. In this context, the positivity preserving properties of HLL-type numerical fluxes allow for a robust and parameter-free

approach. Additionally, the shear preservation of the HLLEM numerical flux is also exhibited, demonstrating a superior performance in the approximation of boundary layers than HLL or Lax Friedrichs, and similar to Roe. Indeed, HLLEM and Roe solvers introduce a reduced amount of numerical dissipation in the approximation of contact or shear layers.

3. **Formulation of the face-centred finite volume method for compressible flows.**

The FCFV method has been proposed for the first time for the formulation of the inviscid Euler and the viscous compressible Navier-Stokes equations. Differently from traditional CCFV or VCFV schemes, the FCFV scheme defines the unknowns of the problem at the mesh faces and describes the conservation variables, stress tensor and heat flux inside each cell by means of an inexpensive computation.

Optimal first-order accuracy of the conservative quantities, stress tensor and heat flux is obtained without need of reconstruction of the gradients. For this reason, the precision of the FCFV method is not compromised by a high stretching or distortion of the mesh cells.

The proposed methodology displays an inherent non-oscillatory behaviour in front of discontinuities, owing to the guarantee of monotonicity of first-order approximations. Hence, wave-like phenomena, such as shear layers, expansions and shock waves, are handled by means of Riemann solvers. Indeed, the traditional approximate Riemann solvers of Lax-Friedrichs, Roe, HLL and HLLEM have been described for the FCFV formulation via a suitable definition of the numerical fluxes. Finally, the method demonstrates its robustness in the incompressible limit, producing stable low Mach solutions without need of specific pressure corrections.

4. **Benchmarking of compressible flows for low and high-order comparison.**

A comprehensive set of numerical benchmarks has been presented for the evaluation of the low and high-order strategies introduced in this thesis. On the one hand, numerical convergence tests of inviscid and viscous flows consisting of the well-known Ringleb and Couette flow problems, respectively, have been introduced for the verification of the optimal accuracy properties of the ap-

proximation. On the other, an extensive set of numerical examples of subsonic, transonic and supersonic external flows has been employed to demonstrate the capabilities of the proposed solvers.

By means of these test cases, an exhaustive evaluation of the robustness and accuracy of the introduced Riemann solvers has been performed both in low and high-order. In particular, the positivity properties of HLL-type Riemann solvers have been demonstrated, whereas the HLLEM flux has displayed an increased resolution of boundary layers. It is worth mentioning that the importance of the numerical fluxes is specially critical in lower-order approximations, based on the larger jumps between elemental and hybrid states. Conversely, the numerical dissipation introduced by numerical fluxes in higher-order approaches tends to vanish and little differences are observed.

The advantages of high-order approximations, supported by the reduced numerical dissipation of the method and the little geometric error in the representation of curved boundaries, have been demonstrated by means of an extensive set of numerical examples. Different transonic and supersonic examples involving shock-waves have also demonstrated the good performance of the shock-capturing techniques presented in this work, including two problems involving strong inviscid-viscous interactions between shock waves and boundary layers.

On the other hand, the FCFV paradigm has demonstrated its great capabilities, offering a robust framework for constructing non-oscillatory solutions based on the inherent monotonicity preservation of the method. The numerical scheme has been employed for the solution of two and three-dimensional compressible flow examples in realistic scenarios, demonstrating the potential of the method to efficiently handle large-scale simulations of steady-state flows.

5.2 Future developments

The work presented in this thesis opens the way to future research lines in order to improve the capabilities of the proposed solvers and to exploit the full potential of the described methodologies. To this end, the following research items are proposed:

1. **Adapt the high-order HDG solver with suitable high-order time-integration schemes for the simulation of transient flows.**

The importance of high-order discretisation methods has been related to the simulation of unsteady problems. Because of the reduced diffusion and dispersion errors of these schemes when compared to low-order, these methods provide a suitable framework to deliver high accuracy in transient phenomena.

In this work, the main focus has been based on the spatial HDG formulation of compressible flows in order to derive the expression of Riemann solvers in hybridised formulations. To this end, the examples considered have just involved steady-state flows. However, a natural next step for the high-fidelity HDG solver would consist of the introduction of high-order time-integrators.

To this end, different time-marching algorithms can be considered. In particular, BDF or DIRK methods have been already proposed in HDG, offering a well-suited environment for the simulation of unsteady problems.

2. **Employ the high-order setting for the simulation of turbulent flows by means of LES or coupled multiphysics phenomena such as aeroacoustics.**

    As previously described, the laminar regime of viscous flows is restricted to a limited range of Reynolds numbers. Many flow applications of industrial interest include the appearance of unsteady turbulent phenomena, for which high-order solvers coupled with advanced methods for turbulence modelling are required. In this case, turbulent predictions based on LES approaches, already proposed within HDG by Fernández et al. (2017), are expected to provide an accurate and efficient framework for the simulation of transition and separation phenomena.

    Moreover, the improvement of discretisation methods and the development of high-order space-time formulations opens the way to a great progress of multiphysics simulations in fields such as aeroacoustics. In this case, high-order approximations are essential for a good resolution of waves, which are in turn driven by unsteady vortices of the flow, both of laminar and turbulent nature.

3. **Improve the capabilities of the current solvers to efficiently perform large-scale simulations in HPC environments.**

    Finally, it is worth mentioning that the proposed approaches have been devised in an academic environment and have been mostly focused in the development of the methodology itself, rather than centred in building a competitive frame-

work for simulation. For this reason, the described implementations have been performed in a high level programming environment such as Matlab.

In order to improve the capabilities of the described solvers and to exploit the potential of HPC resources, different strategies could be incorporated. Among others, the use of lower level programming languages suitable for scientific computing, such as Fortran or C++, and the introduction of more efficient solving strategies, such as the employment of multigrid methods, parallel iterative solvers for large systems of equations and suitable preconditioners. Additionally, it is worth considering the implementation of *hp*-adaptivity techniques allowing to address the inherent complexity of mesh generation, specially in presence of complex or multiscale flow phenomena.

4. **Extend the FCFV method to the formulation of the RANS equations for steady-state turbulent flows.**
   The FCFV formulation of the inviscid Euler equations and the compressible Navier-Stokes equations has been described and studied in detail in this thesis. Nevertheless, multiple scenarios in viscous flows involve the presence of turbulent effects, being the laminar regime constrained to a very limited range of Reynolds numbers. For this reason, the RANS equations, coupled with simple one or two-equations turbulence models, are commonly employed within FV CFD solvers to provide reasonable predictions of steady-state turbulent flows.

   In this context, the FCFV formulation of the RANS equations, integrated with the Spalart-Allmaras turbulence model, has been briefly detailed in appendix C. Indeed, the accuracy properties of the method have been tested by means of a simple problem with analytical solution. However, the limited accuracy on the approximation of the derivatives of different quantities of the flowfield that drive the turbulence model, e.g. the vorticity of the fluid, in such convection-dominated cases entails a tough difficulty for the accurate resolution of this kind of problems. Therefore, the turbulent solver has not been successfully applied to problems of academic or industrial interest yet and further progress needs to be done in this line.

5. **Explore the limits of the FCFV solver in front of well-established FV codes.**
   The proposed FCFV solver has demonstrated a robust optimal accuracy in

highly stretched and distorted cells, besides an inherent non-oscillatory be-
haviour in the approximation of sharp fronts or in low Mach scenarios without
shock capturing or pressure corrections. These features describe some of the
most prominent qualities of this FV paradigm by which the presented method
can be established as a competitive alternative to traditional CCFV or VCFV
solvers. However, a deeper comparison with respect to conventional FV strate-
gies in those scenarios would be of high interest in order to explore the limits
or the FCFV formulation with respect to open-source or commercial solvers.

6. **Introduce an h-adaptivity strategy within the FCFV method for au-
tomatic mesh refinement.**
The FCFV scheme has been employed in this thesis for the simulation of steady-
state compressible flow problems solved in general meshes of academic interest.
In those problems, complex flow features requiring high grid resolution such
as shock waves can appear in a priori unknown locations of the domain. In
this context, the present work has employed meshes displaying a progressive
refinement near regions of interest while keeping a uniformly fine grid resolu-
tion in the surrounding area. However, this *ad hoc* refinement cannot guarantee
neither the desired resolution of the flowfield nor that an excessive number of
degrees of freedom are introduced in regions where the solution could be already
well-resolved with coarser meshes.

In order to overcome the high computational cost derived from this strategy, a
mesh refinement procedure could efficiently provide an efficient and inexpensive
way to reach desired levels of accuracy. In this manner, the method could de-
liver high resolution of localised flow phenomena with minimal computational
cost by exploiting its accurate behaviour in highly non-isotropic meshes. Fur-
thermore, it would contribute in the design of a robust framework for automatic
mesh generation with adaptation to the flowfield necessities with minimal user
intervention.

7. **Formulate a second-order accurate FCFV method for compressible
flows.**
The FCFV method proposed in this thesis for the simulation of compressible
flow problems provides first-order accuracy for the approximation of the conser-
vation quantities and mixed variables. Despite the good performance demon-

strated with respect to other numerical or experimental results, conventional and well-established FV solvers generally display second-order accuracy for the primal quantities.

To this end, a second-order strategy within the FCFV paradigm has been recently devised for elliptic problems on simplicial elements by Vieira et al. (2020), and later extended to general meshes by Giacomini and Sevilla (2020). This approach relies on the piecewise linear approximation of the primal variable inside each element, whereas a constant approximation of the mixed and hybrid variables are considered in each cell and face, respectively. In addition, a particular definition of the numerical fluxes, employing a projection operator similarly to reduced stabilisation approaches by Oikawa (2015, 2016) and Qiu and Shi (2016), is introduced.

This second-order FCFV paradigm could be seamlessly explored for the formulation of compressible flows. The resulting FV solver would be expected to retain first-order and second-order accuracy of mixed and conservation variables, respectively, even in presence of high stretching or distortion of the mesh cells, and to display a robust behaviour in the incompressible limit. However, differently from the first-order approach presented in this thesis, a special treatment for shock capturing would be required in this case, since the second-order accuracy of the approximation would not guarantee the monotonicity of the solution.

Bibliography

Aliabadi, S. K., S. E. Ray, and T. E. Tezduyar (1993). SUPG finite element computation of viscous compressible flows based on the conservation and entropy variables formulations. *Computational Mechanics 11*(5-6), 300–312.

Allmaras, A. R., F. T. Johnson, and P. R. Spalart (2012). Modifications and clarifications for the implementation of the Spalart-Allmaras turbulence model. In *Seventh International Conference on Computational Fluid Dynamics (ICCFD7)*, Volume 1902.

ANSYS Inc. (2017). ANSYS Fluent tutorial guide. Technical report, ANSYS Inc.

Arnold, D. N., F. Brezzi, B. Cockburn, and L. D. Marini (2002, jan). Unified analysis of discontinuous Galerkin methods for elliptic problems. *SIAM Journal on Numerical Analysis 39*(5), 1749–1779.

Asouti, V. G., X. S. Trompoukis, I. C. Kampolis, and K. C. Giannakoglou (2010, may). Unsteady CFD computations using vertex-centered finite volumes for unstructured grids on Graphics Processing Units. *International Journal for Numerical Methods in Fluids 67*(2), 232–246.

Balan, A., M. Woopen, and G. May (2015, jun). Hp-adaptivity on anisotropic meshes for hybridized discontinuous Galerkin scheme. *AIAA paper*.

Ball, D. N. (2008). Contributions of CFD to the 787 - and future needs. In *IDC HPC User Forum – Europe*.

Bank, R. E. and D. J. Rose (1987, aug). Some error estimates for the Box method. *SIAM Journal on Numerical Analysis 24*(4), 777–787.

Bartels, R. E., C. L. Rumsey, and R. T. Biedron (2006). CFL3D Version 6.4 — General usage and aeroelastic analysis. Technical report, NASA/TM-2006-214301.

Bassi, F. and S. Rebay (1995). Accurate 2D Euler computations by means of a high order discontinuous finite element method. In S. M. Deshpande, S. S. Desai, and

R. Narasimha (Eds.), *Fourteenth International Conference on Numerical Methods in Fluid Dynamics. Lecture Notes in Physics*, Volume 453, pp. 234–240. Springer Berlin Heidelberg.

Bassi, F. and S. Rebay (1997a). A high-order accurate discontinuous finite element method for the numerical solution of the compressible Navier-Stokes equations. *J. Comput. Phys. 131*(2), 267–279.

Bassi, F. and S. Rebay (1997b). High-order accurate discontinuous finite element solution of the 2D Euler equations. *J. Comput. Phys. 138*(2), 251–285.

Bassi, F. and S. Rebay (2002). Numerical evaluation of two discontinuous Galerkin methods for the compressible Navier-Stokes equations. *Int. J. Numer. Methods Fluids 40*(1-2), 197–207.

Biedron, R. T., J.-R. Carlson, J. M. Derlaga, P. A. Gnoffo, W. T. Dana P. Hammond, B. K. Jones, E. M. Lee-Rausch, E. J. Nielsen, M. A. Park, C. L. Rumsey, J. L. Thomas, K. B. Thompson, and W. A. Wood (2019). FUN3D Manual: 13.6. Technical report, NASA/TM-2019-220416.

Blasius, H. (1908). Grenzschichten in fluessigkeiten mit kleiner reibung. *Zeitschrift fuer Mathematik und Physik 56*(1), 1–37.

Bristeau, M. O., R. Glowinski, J. Periaux, and H. Viviand (1987). Numerical simulation of compressible Navier-Stokes flows: a GAMM workshop. In *Notes on Numerical Fluid Mechanics*, Volume 18. Vieweg+Teubner Verlag.

Bui-Thanh, T. (2015, aug). From Godunov to a unified hybridized discontinuous Galerkin framework for partial differential equations. *J. Comput. Phys. 295*, 114–146.

Cangiani, A., Z. Dong, E. H. Georgoulis, and P. Houston (2017). *hp-Version Discontinuous Galerkin Methods on Polygonal and Polyhedral Meshes*. Springer-Verlag.

Carter, J. E. (1972). Numerical solutions of the Navier-Stokes equations for the supersonic laminar flow over a two-dimensional compression corner. Technical report, NASA-TR-R-385.

Casoni, E., J. Peraire, and A. Huerta (2012, oct). One-dimensional shock-capturing for high-order discontinuous Galerkin methods. *Int. J. Numer. Methods Fluids 71*(6), 737–755.

Chalot, F. and P.-E. Normand (2010). Higher-order stabilized finite elements in an industrial Navier-Stokes code. In N. Kroll, H. Bieler, H. Deconinck, V.Couaillier, H. van der Ven, and K. Sørensen (Eds.), *ADIGMA – A European initiative on the development of adaptive higher-order variational methods for aerospace applications*, pp. 145–165. Springer-Verlag GmbH.

Chalot, F. L. and P. Perrier (2004). Industrial aerodynamics. *Encyclopedia of computational mechanics*.

Chassaing, J.-C., S. Khelladi, and X. Nogueira (2013). Accuracy assessment of a high-order moving least squares finite volume method for compressible flows. *Computers & Fluids 71*, 41–53.

Chiocchia, G. (1985). Exact solutions to transonic and supersonic flows. *AGARD Technical Report AR–211*.

Cockburn, B. (2001, mar). Devising discontinuous Galerkin methods for non-linear hyperbolic conservation laws. *J. Comput. Appl. Math. 128*(1-2), 187–204.

Cockburn, B. (2016). Static condensation, hybridization, and the devising of the HDG methods. In *Lecture Notes in Computational Science and Engineering*, pp. 129–177. Springer International Publishing.

Cockburn, B., D. A. Di Pietro, and A. Ern (2016, may). Bridging the hybrid high-order and hybridizable discontinuous Galerkin methods. *ESAIM: Mathematical Modelling and Numerical Analysis 50*(3), 635–650.

Cockburn, B. and G. Fu (2016a, nov). Superconvergence by M-decompositions. part II: Construction of two-dimensional finite elements. *ESAIM: Mathematical Modelling and Numerical Analysis 51*(1), 165–186.

Cockburn, B. and G. Fu (2016b, dec). Superconvergence by M-decompositions. part III: Construction of three-dimensional finite elements. *ESAIM: Mathematical Modelling and Numerical Analysis 51*(1), 365–398.

Cockburn, B. and G. Fu (2017, jun). Devising superconvergent HDG methods with symmetric approximate stresses for linear elasticity by M-decompositions. *IMA Journal of Numerical Analysis 38*(2), 566–604.

Cockburn, B., G. Fu, and W. Qiu (2016, jul). A note on the devising of supe convergent HDG methods for Stokes flow by M-decompositions. *IMA Journal of Numerical Analysis*.

Cockburn, B., G. Fu, and F. J. Sayas (2016, nov). Superconvergence by M-decompositions. part I: General theory for HDG methods for diffusion. *Mathematics of Computation 86*(306), 1609–1641.

Cockburn, B. and J. Gopalakrishnan (2004). A characterization of hybridized mixed methods for second order elliptic problems. *SIAM Journal on Numerical Analysis 42*(1), 283–301.

Cockburn, B. and J. Gopalakrishnan (2005a). Incompressible finite elements via hybridization. Part i: the Stokes system in two space dimensions. *SIAM Journal on Numerical Analysis 43*(4), 1627–1650.

Cockburn, B. and J. Gopalakrishnan (2005b). Incompressible finite elements via hybridization. Part ii: the Stokes system in three space dimensions. *SIAM Journal on Numerical Analysis 43*(4), 1651–1672.

Cockburn, B. and J. Gopalakrishnan (2009, jan). The derivation of hybridizable discontinuous Galerkin methods for Stokes flow. *SIAM Journal on Numerical Analysis 47*(2), 1092–1125.

Cockburn, B., J. Gopalakrishnan, and R. Lazarov (2009). Unified hybridization of discontinuous Galerkin, mixed, and continuous Galerkin methods for second order elliptic problems. *SIAM J. Numer. Anal. 47*(2), 1319–1365.

Cockburn, B., G. E. Karniadakis, and C.-W. Shu (2000). The development of discontinuous Galerkin methods. In *Discontinuous Galerkin Methods*, pp. 3–50. Berlin, Germany: Springer-Verlag Berlin Heidelberg.

Cockburn, B., S.-Y. Lin, and C.-W. Shu (1989a). TVB Runge-Kutta local projection discontinuous Galerkin finite element method for conservation laws III: one-dimensional systems. *J. Comput. Phys. 84*(1), 90–113.

Cockburn, B., S.-Y. Lin, and C.-W. Shu (1989b). TVB runge-kutta local projection discontinuous galerkin finite element method for conservation laws III: One-dimensional systems. *Journal of Computational Physics 84*(1), 90–113.

Cockburn, B. and K. Shi (2012, oct). Superconvergent HDG methods for linear elasticity with weakly symmetric stresses. *IMA Journal of Numerical Analysis 33*(3), 747–770.

Cockburn, B. and C.-W. Shu (1998a). The Local Discontinuous Galerkin method for time-dependent convection-diffusion systems. *SIAM Journal on Numerical Analysis 35*(6), 2440–2463.

Cockburn, B. and C.-W. Shu (1998b). The runge-kutta discontinuous galerkin method for conservation laws v. *Journal of Computational Physics 141*(2), 199–224.

Cockburn, B. and C.-W. Shu (1998c, apr). The Runge–Kutta Discontinuous Galerkin Method for Conservation Laws V. *J. Comput. Phys. 141*(2), 199–224.

Cook, A. W. and W. H. Cabot (2005, mar). Hyperviscosity for shock-turbulence interactions. *J. Comput. Phys. 203*(2), 379–385.

Cueto-Felgueroso, L., I. Colominas, X. Nogueira, F. Navarrina, and M. Casteleiro (2007, sep). Finite volume solvers and moving least-squares approximations for the compressible navier–stokes equations on unstructured grids. *Comput. Methods Appl. Mech. Eng. 196*(45-48), 4712–4736.

Degrez, G., C. H. Boccadoro, and J. F. Wendt (1987, apr). The interaction of an oblique shock wave with a laminar boundary layer revisited. An experimental and numerical study. *J. Fluid Mech. 177*, 247–263.

Di Pietro, D. and A. Ern (2015). A hybrid high-order locking-free method for linear elasticity on general meshes. *Comput. Methods Appl. Mech. Eng. 283*, 1–21.

Di Pietro, D. A., A. Ern, and S. Lemaire (2014, oct). An arbitrary-order and compact-stencil discretization of diffusion on general meshes based on local reconstruction operators. *Computational Methods in Applied Mathematics 14*(4), 461–472.

Diskin, B. and J. L. Thomas (2011, apr). Comparison of node-centered and cell-centered unstructured finite-volume discretizations: Inviscid fluxes. *AIAA Journal 49*(4), 836–854.

Diskin, B., J. L. Thomas, E. J. Nielsen, H. Nishikawa, and J. A. White (2010, jul). Comparison of node-centered and cell-centered unstructured finite-volume discretizations: Viscous fluxes. *AIAA Journal 48*(7), 1326–1338.

Donea, J. and A. Huerta (2003). *Finite Element Methods for Flow Problems*. John Wiley & Sons, Ltd.

Drikakis, D. (2003, aug). Advances in turbulent flow computations using high-resolution methods. *Prog. Aerosp. Sci. 39*(6-7), 405–424.

Drosson, M., K. Hillewaert, and J.-A. Essers (2013, jan). Stability and boundary resolution analysis of the discontinuous Galerkin method applied to the Reynolds-averaged Navier–Stokes equations using the Spalart–Allmaras model. *SIAM Journal on Scientific Computing 35*(3), B666–B700.

Dumbser, M. and D. S. Balsara (2016, jan). A new efficient formulation of the HLLEM Riemann solver for general conservative and non-conservative hyperbolic systems. *J. Comput. Phys. 304*, 275–319.

Dumbser, M., M. Kser, V. A. Titarev, and E. F. Toro (2007, sep). Quadrature-free non-oscillatory finite volume schemes on unstructured meshes for nonlinear hyperbolic systems. *J. Comput. Phys. 226*(1), 204–243.

Eça, L., M. Hoekstra, A. Hay, and D. Pelletier (2007). On the construction of manufactured solutions for one and two-equation eddy-viscosity models. *Int. J. Numer. Methods Fluids 54*(2), 119–154.

Egger, H. and J. Schöberl (2009). A hybrid mixed discontinuous Galerkin finite-element method for convection-diffusion problems. *IMA J. Numer. Anal. 30*(4), 1206–1234.

Egger, H. and C. Waluga (2012a, oct). *hp*-analysis of a hybrid DG method for Stokes flow. *IMA Journal of Numerical Analysis 33*(2), 687–721.

Egger, H. and C. Waluga (2012b). A hybrid mortar method for incompressible flow. *Int J Numer Anal Model 9*(4), 793–812.

Einfeldt, B. (1988). On Godunov-type methods for gas dynamics. *SIAM Journal on Numerical Analysis 25*(2), 294–318.

Einfeldt, B., C. Munz, P. Roe, and B. Sjgreen (1991, feb). On Godunov-type methods near low densities. *J. Comput. Phys. 92*(2), 273–295.

Ekaterinaris, J. A. (2005, apr). High-order accurate, low numerical diffusion methods for aerodynamics. *Prog. Aerosp. Sci. 41*(3-4), 192–300.

Ekelschot, D., D. Moxey, S. Sherwin, and J. Peiró (2017, mar). A p-adaptation method for compressible flow problems using a goal-based error indicator. *Computers & Structures 181*, 55–69.

Ern, A. and D. A. Di Pietro (2011). *Mathematical Aspects of Discontinuous Galerkin Methods.* Springer-Verlag.

Eymard, R., T. Gallout, and R. Herbin (2000). Finite volume methods. In *Handbook of Numerical Analysis*, pp. 713–1018. Elsevier.

Fernández, P., C. Nguyen, and J. Peraire (2018, jan). A physics-based shock capturing method for unsteady laminar and turbulent flows. *AIAA Paper*.

Fernández, P., N. C. Nguyen, and J. Peraire (2017, may). The hybridized Discontinuous Galerkin method for Implicit Large-Eddy Simulation of transitional turbulent flows. *J. Comput. Phys. 336*, 308–329.

Fish, J. and T. Belytschko (2007). *A First Course in Finite Elements.* John Wiley and Sons Ltd.

Fleischmann, N., S. Adami, X. Y. Hu, and N. A. Adams (2019, oct). A low dissipation method to cure the grid-aligned shock instability. *J. Comput. Phys.*, 109004.

Gerhold, T. (2005). Overview of the hybrid RANS code TAU. In *MEGAFLOW-Numerical Flow Simulation for Aircraft Design*, pp. 81–92. Springer.

Giacomini, M., A. Karkoulias, R. Sevilla, and A. Huerta (2018, oct). A superconvergent HDG method for Stokes flow with strongly enforced symmetry of the stress tensor. *J. Sci. Comput. 77*(3), 1679–1702.

Giacomini, M. and R. Sevilla (2019). Discontinuous Galerkin approximations in computational mechanics: hybridization, exact geometry and degree adaptivity. *SN Appl. Sci. 1*, 1047.

Giacomini, M. and R. Sevilla (2020, jul). A second-order face-centred finite volume method on general meshes with automatic mesh adaptation. *Int. J. Numer. Methods Eng. 121*(23), 5227–5255.

Giacomini, M., R. Sevilla, and A. Huerta (2020). *Tutorial on Hybridizable Discontinuous Galerkin (HDG) Formulation for Incompressible Flow Problems*, pp. 163–201. Cham: Springer International Publishing.

Giorgiani, G., S. Fernández-Méndez, and A. Huerta (2014, jul). Hybridizable discontinuous Galerkin with degree adaptivity for the incompressible Navier-Stokes equations. *Comput. Fluids 98*, 196–208.

Godunov, S. K. and I. Bohachevsky (1959). Finite difference method for numerical computation of discontinuous solutions of the equations of fluid dynamics. *Mat. Sb. 47*(3), 271–306.

Guyan, R. J. (1965, feb). Reduction of stiffness and mass matrices. *AIAA Paper 3*(2), 380–380.

Hakkinen, R. J., I. Greber, L. Trilling, and S. S. Abarbanel (1959). The interaction of an oblique shock wave with a laminar boundary layer. Technical report, NASA Memo 2-18-59W.

Harten, A. and J. M. Hyman (1983, may). Self adjusting grid methods for one-dimensional hyperbolic conservation laws. *J. Comput. Phys. 50*(2), 235–269.

Harten, A., P. D. Lax, and B. van Leer (1983, jan). On Upstream Differencing and Godunov-Type Schemes for Hyperbolic Conservation Laws. *SIAM Review 25*(1), 35–61.

Hartmann, R. and P. Houston (2003, jan). Adaptive discontinuous Galerkin finite element methods for nonlinear hyperbolic conservation laws. *SIAM Journal on Scientific Computing 24*(3), 979–1004.

Hassan, O., K. Morgan, and N. P. Weatherill (2008). Flite system. version 4. theoretical manual. Technical report, Swansea University.

Huerta, A., A. Angeloski, X. Roca, and J. Peraire (2013). Efficiency of high-order elements for continuous and discontinuous Galerkin methods. *Int. J. Numer. Methods Eng. 96*(9), 529–560.

Huerta, A., E. Casoni, and J. Peraire (2011, aug). A simple shock-capturing technique for high-order discontinuous Galerkin methods. *Int. J. Numer. Methods Fluids 69*(10), 1614–1632.

Hung, C. and R. MacCormack (1976, apr). Numerical solutions of supersonic and hypersonic laminar compression corner flows. *AIAA Journal 14*(4), 475–481.

Jasak, H. (2009). OpenFOAM: open source CFD in research and industry. *International Journal of Naval Architecture and Ocean Engineering 1*(2), 89–94.

Jaust, A. and J. Schütz (2014, jul). A temporally adaptive hybridized discontinuous Galerkin method for time-dependent compressible flows. *Computers & Fluids 98*, 177–185.

Jaust, A., J. Schütz, and M. Woopen (2014, jun). A hybridized discontinuous Galerkin method for unsteady flows with shock-capturing. In *44th AIAA Fluid Dynamics Conference*. American Institute of Aeronautics and Astronautics.

Jaust, A., J. Schütz, and M. Woopen (2015). An HDG method for unsteady compressible flows. In *Lecture Notes in Computational Science and Engineering*, pp. 267–274. Springer International Publishing.

Johnson, F. T., E. N. Tinoco, and N. J. Yu (2005, dec). Thirty years of development and application of CFD at Boeing Commercial Airplanes, Seattle. *Computers & Fluids 34*(10), 1115–1151.

Katzer, E. (1989, sep). On the lengthscales of laminar shock/boundary-layer interaction. *Journal of Fluid Mechanics 206*, 477–496.

Kawai, S. and S. Lele (2008, nov). Localized artificial diffusivity scheme for discontinuity capturing on curvilinear meshes. *J. Comput. Phys. 227*(22), 9498–9526.

Kawai, S., S. K. Shankar, and S. K. Lele (2010, mar). Assessment of localized artificial diffusivity scheme for large-eddy simulation of compressible turbulent flows. *J. Comput. Phys. 229*(5), 1739–1762.

Komala-Sheshachala, S., R. Sevilla, and O. Hassan (2020, apr). A coupled HDG-FV scheme for the simulation of transient inviscid compressible flows. *Computers & Fluids 202*, 104495.

Kotteda, V. K. and S. Mittal (2014, feb). Stabilized finite-element computation of compressible flow with linear and quadratic interpolation functions. *Int. J. Numer. Methods Fluids 75*(4), 273–294.

Kraft, E. (2010, jan). Integrating computational science and engineering to re-engineer the aeronautical development process. *AIAA Paper*.

Krivodonova, L. and M. Berger (2006, jan). High-order accurate implementation of solid wall boundary conditions in curved geometries. *J. Comput. Phys. 211*(2), 492–512.

Kroll, N. (2009, January). *ADIGMA: A European Project on the Development of Adaptive Higher Order Variational Methods for Aerospace Applications*. Aerospace Sciences Meetings. American Institute of Aeronautics and Astronautics.

Kroll, N., C. Hirsch, F. Bassi, C. Johnston, and K. Hillewaert (Eds.) (2015). *IDIHOM: Industrialization of High-Order Methods - A Top-Down Approach.* Springer International Publishing.

La Spina, A., M. Kronbichler, M. Giacomini, W. A. Wall, and A. Huerta (2020). A weakly compressible hybridizable discontinuous Galerkin formulation for fluid-structure interaction problems. *Computer Methods in Applied Mechanics and Engineering 372*, 113392.

Lax, P. D. (1954, feb). Weak solutions of nonlinear hyperbolic equations and their numerical computation. *Commun. Pure Appl. Math. 7*(1), 159–193.

Lehrenfeld, C. and J. Schberl (2016, aug). High order exactly divergence-free hybrid discontinuous Galerkin methods for unsteady incompressible flows. *Computer Methods in Applied Mechanics and Engineering 307*, 339–361.

Maire, P.-H., R. Abgrall, J. Breil, and J. Ovadia (2007, jan). A cell-centered Lagrangian scheme for two-dimensional compressible flow problems. *SIAM Journal on Scientific Computing 29*(4), 1781–1824.

Malik, M. R. and D. M. Bushnell (2012). Role of computational fluid dynamics and wind tunnels in aeronautics R&D. *NASA TP-2012-217602*.

Mengaldo, G., D. D. Grazia, F. Witherden, A. Farrington, P. Vincent, S. Sherwin, and J. Peiro (2014, jun). A guide to the implementation of boundary conditions in compact high-order methods for compressible aerodynamics. *AIAA Paper*.

Mittal, S. and S. Yadav (2001, dec). Computation of flows in supersonic wind-tunnels. *Comput. Methods Appl. Mech. Eng. 191*(6-7), 611–634.

Montlaur, A., S. Fernández-Méndez, and A. Huerta (2008). Discontinuous Galerkin methods for the Stokes equations using divergence-free approximations. *Int. J. Numer. Methods Fluids 57*(9), 1071–1092.

Morgan, K., J. Peraire, J. Peiro, and O. Hassan (1991, jun). The computation of three-dimensional flows using unstructured grids. *Comput. Methods Appl. Mech. Eng. 87*(2-3), 335–352.

Moro, D., N. Nguyen, and J. Peraire (2011, jun). Navier-Stokes solution using hybridizable discontinuous Galerkin methods. *AIAA Paper*.

Moro, D., N. C. Nguyen, and J. Peraire (2016, mar). Dilation-based shock capturing for high-order methods. *Int. J. Numer. Methods Fluids 82*(7), 398–416.

Moro, D., N. C. Nguyen, J. Peraire, and M. Drela (2017, jun). Mesh topology preserving boundary-layer adaptivity method for steady viscous flows. *AIAA Paper 55*(6), 1970–1985.

Morton, K. W. and T. Sonar (2007, apr). Finite volume methods for hyperbolic conservation laws. *Acta Numerica 16*, 155–238.

Moura, R. C., G. Mengaldo, J. Peiró, and S. J. Sherwin (2017, feb). On the eddy-resolving capability of high-order discontinuous Galerkin approaches to implicit LES / under-resolved DNS of Euler turbulence. *J. Comput. Phys. 330*, 615–623.

Moura, R. C., S. J. Sherwin, and J. Peiró (2015, oct). Linear dispersion–diffusion analysis and its application to under-resolved turbulence simulations using discontinuous Galerkin spectral/hp methods. *J. Comput. Phys. 298*, 695–710.

Nguyen, N., J. Peraire, and B. Cockburn (2015, dec). A class of embedded discontinuous Galerkin methods for computational fluid dynamics. *J. Comput. Phys. 302*, 674–692.

Nguyen, N. C. and J. Peraire (2011). An Adaptive Shock-Capturing HDG Method for Compressible Flows. *AIAA Paper 3060*.

Nguyen, N. C. and J. Peraire (2012). Hybridizable discontinuous Galerkin methods for partial differential equations in continuum mechanics. *J. Comput. Phys. 231*(18), 5955–5988.

Nguyen, N. C., J. Peraire, and B. Cockburn (2009a, may). An implicit high-order hybridizable discontinuous Galerkin method for linear convection–diffusion equations. *J. Comput. Phys. 228*(9), 3232–3254.

Nguyen, N. C., J. Peraire, and B. Cockburn (2009b, dec). An implicit high-order hybridizable discontinuous Galerkin method for nonlinear convection–diffusion equations. *J. Comput. Phys. 228*(23), 8841–8855.

Nguyen, N. C., J. Peraire, and B. Cockburn (2011, feb). An implicit high-order hybridizable discontinuous Galerkin method for the incompressible Navier-Stokes equations. *J. Comput. Phys. 230*(4), 1147–1170.

Nogueira, X., L. Cueto-Felgueroso, I. Colominas, H. Gómez, F. Navarrina, and M. Casteleiro (2009, jun). On the accuracy of finite volume and discontinuous Galerkin discretizations for compressible flow on unstructured grids. *Int. J. Numer. Methods Eng. 78*(13), 1553–1584.

Oikawa, I. (2015, dec). A hybridized discontinuous Galerkin method with reduced stabilization. *J. Sci. Comput. 65*(1), 327–340.

Oikawa, I. (2016, aug). Analysis of a reduced-order HDG method for the Stokes equations. *J. Sci. Comput. 67*(2), 475–492.

Osher, S. and S. Chakravarthy (1986). Very high order accurate TVD schemes. In *The IMA Volumes in Mathematics and Its Applications*, pp. 229–274. Springer New York.

Patankar, S. and D. Spalding (1972). A calculation procedure for heat, mass and momentum transfer in three-dimensional parabolic flows. *International Journal of Heat and Mass Transfer 15*(10), 1787 – 1806.

Peery, K. and S. Imlay (1988, jul). Blunt-body flow simulations. *AIAA Paper 2904*.

Peraire, J., C. Nguyen, and B. Cockburn (2011). An Embedded Discontinuous Galerkin Method for the Compressible Euler and Navier-Stokes Equations. *AIAA Paper 3228*.

Peraire, J., N. C. Nguyen, and B. Cockburn (2010). A hybridizable Discontinuous Galerkin Method for the Compressible Euler and Navier-Stokes Equations. *AIAA Paper 363*.

Persson, P.-O. (2013, jun). Shock Capturing for High-Order Discontinuous Galerkin Simulation of Transient Flow Problems. *AIAA Paper 3061*.

Persson, P.-O. and J. Peraire (2006, jan). Sub-Cell Shock Capturing for Discontinuous Galerkin Methods. *AIAA Paper 0112*.

Perthame, B. and C.-W. Shu (1996, mar). On positivity preserving finite volume schemes for Euler equations. *Numerische Mathematik 73*(1), 119–130.

Qamar, A., N. Hasan, and S. Sanghi (2006, may). New scheme for the computation of compressible flows. *AIAA Journal 44*(5), 1025–1039.

Qiu, J., B. C. Khoo, and C.-W. Shu (2006, mar). A numerical study for the performance of the Runge–Kutta discontinuous Galerkin method based on different numerical fluxes. *J. Comput. Phys. 212*(2), 540–565.

Qiu, W., J. Shen, and K. Shi (2017, may). An HDG method for linear elasticity with strong symmetric stresses. *Mathematics of Computation 87*(309), 69–93.

Qiu, W. and K. Shi (2016). A superconvergent HDG method for the incompressible Navier-Stokes equations on general polyhedral meshes. *IMA J. Numer. Anal. 36*(4), 1943–1967.

Quirk, J. J. (1994, mar). A contribution to the great Riemann solver debate. *Int. J. Numer. Methods Fluids 18*(6), 555–574.

Randall J. Leveque, L. R. J. (2013). *Finite Volume Methods for Hyperbolic Problems*. Cambridge University Press.

Riemann, B. (1860). ber die fortpflanzung ebener luftwellen von endlicher schwingungsweite. *Abhandlungen der Kniglichen Gesellschaft der Wissenschaften in Gttingen 8*, 43–66.

Roca, X., C. Nguyen, and J. Peraire (2013, jun). Scalable parallelization of the hybridized discontinuous Galerkin method for compressible flow. *AIAA Paper*.

Roe, P. L. (1981). Approximate Riemann solvers, parameter vectors, and difference schemes. *J. Comput. Phys. 43*(2), 357–372.

Rohde, A. (2001, jun). Eigenvalues and eigenvectors of the Euler equations in general geometries. *AIAA Paper*.

Rumsey, C. L. and J. L. Thomas (2008). Application of FUN3D and CFL3D to the third workshop on CFD uncertainty analysis. Technical report, NASA/TM-2008-215537.

Samii, A. and C. Dawson (2018, mar). An explicit hybridized discontinuous Galerkin method for Serre–Green–Naghdi wave model. *Computer Methods in Applied Mechanics and Engineering 330*, 447–470.

Samii, A., K. Kazhyken, C. Michoski, and C. Dawson (2019, jul). A comparison of the explicit and implicit hybridizable discontinuous Galerkin methods for nonlinear shallow water equations. *Journal of Scientific Computing 80*(3), 1936–1956.

Schlichting, H. and K. Gersten (2016). *Boundary-Layer Theory*. Springer Berlin Heidelberg.

Schmitt, V. and F. Charpin (1979). Pressure distributions on the ONERA-M6 wing at transonic Mach numbers. Technical report, Report of the fluid Dynamics panel. Working group 04.

Schütz, J. and G. May (2013a, oct). An adjoint consistency analysis for a class of hybrid mixed methods. *IMA Journal of Numerical Analysis 34*(3), 1222–1239.

Schütz, J. and G. May (2013b). A hybrid mixed method for the compressible Navier-Stokes equations. *J. Comput. Phys. 240*, 58 – 75.

Schütz, J., M. Woopen, and G. May (2012, jan). A hybridized DG/mixed scheme for nonlinear advection-diffusion systems, including the compressible Navier-Stokes equations. *AIAA Paper*.

Selmin, V. (1993, jan). The node-centred finite volume approach: Bridge between finite differences and finite elements. *Comput. Methods Appl. Mech. Eng. 102*(1), 107–138.

Sevilla, R., S. Fernández-Méndez, and A. Huerta (2008, jul). NURBS-enhanced finite element method for Euler equations. *Int. J. Numer. Methods Fluids 57*(9), 1051–1069.

Sevilla, R., S. Fernández-Méndez, and A. Huerta (2008). NURBS-enhanced finite element method (NEFEM). *Int. J. Numer. Methods Eng. 76*(1), 56–83.

Sevilla, R., M. Giacomini, and A. Huerta (2018, may). A face-centred finite volume method for second-order elliptic problems. *Int. J. Numer. Methods Eng. 115*(8), 986–1014.

Sevilla, R., M. Giacomini, and A. Huerta (2019, feb). A locking-free face-centred finite volume (FCFV) method for linear elastostatics. *Computers & Structures 212*, 43–57.

Sevilla, R., M. Giacomini, A. Karkoulias, and A. Huerta (2018, aug). A supercon-vergent hybridisable discontinuous Galerkin method for linear elasticity. *Int. J. Numer. Methods Eng. 116*(2), 91–116.

Sevilla, R., A. J. Gil, and M. Weberstadt (2017). A high-order stabilised ale finite element formulation for the euler equations on deformable domains. *Computers & Structures 181*, 89–102.

Sevilla, R., O. Hassan, and K. Morgan (2013, jan). An analysis of the performance of a high-order stabilised finite element method for simulating compressible flows. *Comput. Methods Appl. Mech. Eng. 253*, 15–27.

Sevilla, R. and A. Huerta (2016). Tutorial on Hybridizable Discontinuous Galerkin (HDG) for second-order elliptic problems. In J. Schröder and P. Wriggers (Eds.), *Advanced Finite Element Technologies*, Volume 566 of *CISM International Centre for Mechanical Sciences*, pp. 105–129. Springer International Publishing.

Shakib, F., T. J. Hughes, and Z. Johan (1991, aug). A new finite element formulation for computational fluid dynamics: X. The compressible Euler and Navier-Stokes equations. *Computer Methods in Applied Mechanics and Engineering 89*(1-3), 141–219.

Slotnick, J. P., A. Khodadoust, J. J. Alonso, D. L. Darmofal, W. Gropp, E. Lurie, and D. J. Mavriplis (2014). Cfd vision 2030 study: A path to revolutionary computational aerosciences. Technical report, NASA.

Sørensen, K., O. Hassan, K. Morgan, and N. Weatherill (2003). A multigrid ac-celerated hybrid unstructured mesh method for 3D compressible turbulent flow. *Computational mechanics 31*(1-2), 101–114.

Spalart, P. R. and S. R. Allmaras (1992, jan). A one-equation turbulence model for aerodynamic flows. *AIAA Paper*.

Svärd, M., J. Gong, and J. Nordström (2008, aug). An accuracy evaluation of unstruc-tured node-centred finite volume methods. *Applied Numerical Mathematics 58*(8), 1142–1158.

Thibert, J. J., M. Granjacques, and L. H. Ohman (1979). NACA 0012 Airfoil. *AGARD Advisory Report AR–138 A1*.

Toro, E. F. (2009). *Riemann Solvers and Numerical Methods for Fluid Dynamics.* Springer-Verlag Berlin Heidelberg.

Tuck, E. O. (1991, jan). A criterion for leading-edge separation. *J. Fluid Mech. 222*(-1), 33.

van Leer, B. (1974, mar). Towards the ultimate conservative difference scheme. II. monotonicity and conservation combined in a second-order scheme. *J. Comput. Phys. 14*(4), 361–370.

van Leer, B. (1977a, mar). Towards the ultimate conservative difference scheme III. upstream-centered finite-difference schemes for ideal compressible flow. *J. Comput. Phys. 23*(3), 263–275.

van Leer, B. (1977b, mar). Towards the ultimate conservative difference scheme. IV. a new approach to numerical convection. *J. Comput. Phys. 23*(3), 276–299.

van Leer, B. (1979, jul). Towards the ultimate conservative difference scheme. V. a second-order sequel to Godunov's method. *J. Comput. Phys. 32*(1), 101–136.

Vieira, L. M., M. Giacomini, R. Sevilla, and A. Huerta (2020). A second-order face-centred finite volume method for elliptic problems. *Computer Methods in Applied Mechanics and Engineering 358*, 112655.

Vila-Pérez, J., M. Giacomini, R. Sevilla, and A. Huerta (2020, nov). Hybridisable discontinuous Galerkin formulation of compressible flows. *Arch. Comput. Methods Eng.*.

Von Neumann, J. and R. D. Richtmyer (1950, mar). A method for the numerical calculation of hydrodynamic shocks. *J. Appl. Phys. 21*(3), 232–237.

Vymazal, M., L. Koloszar, S. D'Angelo, N. Villedieu, M. Ricchiuto, and H. Deconinck (2015). High-order residual distribution and error estimation for steady and unsteady compressible flow. In *Notes on Numerical Fluid Mechanics and Multidisciplinary Design*, pp. 381–395. Springer International Publishing.

Wang, Z. and Y. Liu (2006, jan). Extension of the spectral volume method to high-order boundary representation. *J. Comput. Phys. 211*(1), 154–178.

Wang, Z. J., K. Fidkowski, R. Abgrall, F. Bassi, D. Caraeni, A. Cary, H. Deconinck, R. Hartmann, K. Hillewaert, H. T. Huynh, N. Kroll, G. May, P.-O. Persson, B. van Leer, and M. Visbal (2013, jan). High-order CFD methods: current status and perspective. *Int. J. Numer. Methods Fluids 72*(8), 811–845.

Williams, D. M. (2018). An entropy stable, hybridizable discontinuous Galerkin method for the compressible Navier-Stokes equations. *Math. Comp. 87*(309), 95–121.

Wong, J. S., D. L. Darmofal, and J. Peraire (2001, aug). The solution of the compressible Euler equations at low Mach numbers using a stabilized finite element algorithm. *Comput. Methods Appl. Mech. Eng. 190*(43-44), 5719–5737.

Woopen, M., A. Balan, G. May, and J. Schütz (2014). A comparison of hybridized and standard DG methods for target-based hp-adaptive simulation of compressible flow. *Comput. Fluids 98*, 3 – 16.

Woopen, M., T. Ludescher, and G. May (2014, jun). A hybridized discontinuous Galerkin method for turbulent compressible flow. *AIAA Paper*.

Yano, M. and D. L. Darmofal (2012). Case C1. 3: Flow over the NACA 0012 airfoil: subsonic inviscid, transonic inviscid, and subsonic laminar flows. In *First International Workshop on High-Order CFD methods*.

Yoshihara, H. and P. Sacher (1985). Test cases for inviscid flow field methods. *AGARD Advisory Report AR-211*.

Appendix A

Enforcing the symmetry of the mixed variable

In sections 2.2.1 and 3.1, the deviatoric strain rate tensor $\boldsymbol{\varepsilon}^d$ has been introduced as mixed variable in the FCFV formulation. In this appendix, the implementation details to construct this symmetric mixed variable are provided.

First, it is worth recalling that the symmetric second-order tensor $\boldsymbol{\varepsilon}^d$ is commonly represented using a matrix of dimension $\mathtt{n_{sd}} \times \mathtt{n_{sd}}$. Nonetheless, only $\mathtt{m_{sd}} = \mathtt{n_{sd}}(\mathtt{n_{sd}} + 1)/2$ components of this tensor are non-redundant. In order to exploit such symmetry in the discretisation, Voigt notation Fish and Belytschko (2007) is employed. Its discrete counterpart $\boldsymbol{\varepsilon}_{\mathtt{V}}^d$ can thus be expressed as an $\mathtt{m_{sd}}$-dimensional vector after a rearrangement of its non-redundant components, namely

$$
\boldsymbol{\varepsilon}_{\mathtt{V}}^d := \begin{cases} \left[\varepsilon_{11}^d, \ \varepsilon_{22}^d, \ \varepsilon_{12}^d \right]^T & \text{in 2D,} \\ \left[\varepsilon_{11}^d, \ \varepsilon_{22}^d, \ \varepsilon_{33}^d, \ \varepsilon_{12}^d, \ \varepsilon_{13}^d, \ \varepsilon_{23}^d \right]^T & \text{in 3D.} \end{cases} \tag{A.1}
$$

Following remark 2.4, the discrete strain rate tensor is defined as $\boldsymbol{\varepsilon}_{\mathtt{V}}^d = \boldsymbol{D}_{\mathtt{V}} \boldsymbol{\nabla}_{\mathtt{S}} \boldsymbol{v}$. Here, the matrices $\boldsymbol{D}_{\mathtt{V}}$ and $\boldsymbol{\nabla}_{\mathtt{S}}$ stand for the Voigt counterparts of the operator $\mathcal{D}$ and of the symmetric part of the gradient $\boldsymbol{\nabla}^{\mathtt{S}}$, respectively, and are given by

$$
\boldsymbol{D}_{\mathtt{V}} := \begin{bmatrix} 2\mathbf{I}_{\mathtt{n_{sd}}} - \dfrac{2}{3}\mathbf{J}_{\mathtt{n_{sd}}} & \mathbf{0}_{\mathtt{n_{sd}} \times \mathtt{n_{rr}}} \\ \mathbf{0}_{\mathtt{n_{rr}} \times \mathtt{n_{sd}}} & \mathbf{I}_{\mathtt{n_{rr}}} \end{bmatrix} \tag{A.2a}
$$

and

$$
\boldsymbol{\nabla}_{\mathsf{s}} := \begin{cases} \begin{bmatrix} \partial/\partial x_1 & 0 & \partial/\partial x_2 \\ 0 & \partial/\partial x_2 & \partial/\partial x_1 \end{bmatrix}^T & \text{in 2D,} \\[1em] \begin{bmatrix} \partial/\partial x_1 & 0 & 0 & \partial/\partial x_2 & \partial/\partial x_3 & 0 \\ 0 & \partial/\partial x_2 & 0 & \partial/\partial x_1 & 0 & \partial/\partial x_3 \\ 0 & 0 & \partial/\partial x_3 & 0 & \partial/\partial x_1 & \partial/\partial x_2 \end{bmatrix}^T & \text{in 3D.} \end{cases} \tag{A.2b}
$$

where $\mathbf{I}_m$ and $\mathbf{J}_\ell$ denote the $m \times m$ identity matrix and the $\ell \times \ell$ matrix with all components equal to 1, respectively, and $\mathtt{n_{rr}} = \mathtt{n_{sd}}(\mathtt{n_{sd}} - 1)/2$ stands for the number of rigid body rotations, that is, $\mathtt{n_{rr}} = 1$ in 2D and $\mathtt{n_{rr}} = 3$ in 3D.

By employing Voigt notation and exploiting the definitions in (A.2), the second term of equation (2.25a) in the FCFV local problem is implemented as

$$
(\mathcal{D}\widehat{\boldsymbol{v}} \otimes \boldsymbol{n})_{\mathsf{V}} = \boldsymbol{D}_{\mathsf{V}}\boldsymbol{N}_{\mathsf{V}}\widehat{\boldsymbol{v}}, \tag{A.3}
$$

the matrix $\boldsymbol{N}_{\mathsf{V}}$, accounting for the normal to a surface, being defined as

$$
\boldsymbol{N}_{\mathsf{V}} := \begin{cases} \begin{bmatrix} n_1 & 0 & n_2 \\ 0 & n_2 & n_1 \end{bmatrix}^T & \text{in 2D,} \\[1em] \begin{bmatrix} n_1 & 0 & 0 & n_2 & n_3 & 0 \\ 0 & n_2 & 0 & n_1 & 0 & n_3 \\ 0 & 0 & n_3 & 0 & n_1 & n_2 \end{bmatrix}^T & \text{in 3D,} \end{cases} \tag{A.4}
$$

where n_k denotes the k-th component of the unit normal vector $\boldsymbol{n}$.

The expression in (A.3) is also employed for the implementation of equation (3.11a). Indeed, the implementation of such equation of the weak form based on Voigt notation is given by

$$
\left(\boldsymbol{\zeta}_{\mathsf{V}}, \boldsymbol{\varepsilon}_{\mathsf{V}}^d\right)_{\Omega_e} + \left(\boldsymbol{\nabla}_{\mathsf{s}}^T \mathcal{D}\boldsymbol{\zeta}_{\mathsf{V}}, \boldsymbol{v}_e\right)_{\Omega_e} - \left\langle\boldsymbol{\zeta}_{\mathsf{V}}, \boldsymbol{D}_{\mathsf{V}}\boldsymbol{N}_{\mathsf{V}}\widehat{\boldsymbol{v}}\right\rangle_{\partial\Omega_e} = 0, \tag{A.5}
$$

with both $\boldsymbol{\varepsilon}_{\mathsf{V}}^d \in [\mathcal{W}_t^h(\Omega_e)]^{\mathtt{m_{sd}}}$ and $\boldsymbol{\zeta}_{\mathsf{V}} \in [\mathcal{W}_t^h(\Omega_e)]^{\mathtt{m_{sd}}}$ expressed in Voigt notation.

Appendix B

Riemann solvers in standard FV/DG methods

The choice of the convective numerical fluxes has a critical influence on the accuracy and stability of the numerical solution. For this reason, the approximation of such interface fluxes by means of Riemann solvers has received great attention in the context of finite volumes and discontinuous Galerkin methods, see for example the monograph by Toro (2009) or the works by Randall J. Leveque (2013), Cockburn and Shu (1998c), Qiu et al. (2006) or Moura et al. (2017).

This section details the expression of numerical fluxes arising in FV and DG discretisations with some of the most popular approximate Riemann solvers for compressible flows, namely Lax-Friedrichs, Roe, HLL and HLLEM.

To this end, consider a pair of neighbouring elements, Ω^+ and Ω^-, with shared interface $\Gamma_i = \partial\Omega^+ \cap \partial\Omega^- \subset \Gamma$. The solution at each side of the interface is denoted by $\boldsymbol{U}^\pm$, whereas $\boldsymbol{U}^\star(\boldsymbol{U}^+, \boldsymbol{U}^-)$ represents an intermediate state between $\boldsymbol{U}^+$ and $\boldsymbol{U}^-$.

B.1 Lax-Friedrichs Riemann solver

The first option is represented by the Lax-Friedrichs numerical flux, first described by Lax (1954). This Riemann solver is obtained as an extrapolation of the result for

a scalar convection equation and defines the numerical flux as

$$\widehat{\boldsymbol{F}(\boldsymbol{U})\boldsymbol{n}^{\pm}} = \frac{1}{2}\left[\boldsymbol{F}(\boldsymbol{U}^+) + \boldsymbol{F}(\boldsymbol{U}^-)\right]\boldsymbol{n}^{\pm} + \frac{\lambda_{\max}^{\star}}{2}(\boldsymbol{U}^{\pm} - \boldsymbol{U}^{\mp}), \qquad \text{(B.1)}$$

where $\lambda_{\max}^{\star} := |\boldsymbol{v}^{\star}\cdot\boldsymbol{n}| + c^{\star}$ is the maximum eigenvalue of the matrix $\boldsymbol{A}_n(\boldsymbol{U}^{\star})$ evaluated at the intermediate state $\boldsymbol{U}^{\star}$. It is well-known that the Lax-Friedrichs numerical flux is extremely robust but leads to over-diffusive solutions.

B.2   Roe Riemann solver

The Riemann solver by Roe (1981) approximates the complete wave structure of the Riemann problem, as described by Randall J. Leveque (2013) and Toro (2009), by means of the matrix $|\boldsymbol{A}_n(\boldsymbol{U}^{\star})|$ that linearises the convective fluxes $\boldsymbol{F}(\boldsymbol{U}^{\star})$. More precisely, the Roe numerical flux is given by

$$\widehat{\boldsymbol{F}(\boldsymbol{U})\boldsymbol{n}^{\pm}} = \frac{1}{2}\left[\boldsymbol{F}(\boldsymbol{U}^+) + \boldsymbol{F}(\boldsymbol{U}^-)\right]\boldsymbol{n}^{\pm} + \frac{1}{2}|\boldsymbol{A}_n(\boldsymbol{U}^{\star})|(\boldsymbol{U}^{\pm} - \boldsymbol{U}^{\mp}). \qquad \text{(B.2)}$$

In this expression, the spectral decomposition of the Jacobian matrix of the convective flux is employed, namely $\boldsymbol{A}_n(\boldsymbol{U}^{\star}) := [\partial\boldsymbol{F}(\boldsymbol{U}^{\star})/\partial\boldsymbol{U}^{\star}]\cdot\boldsymbol{n} = \boldsymbol{R}\boldsymbol{\Lambda}\boldsymbol{L}$, where $\boldsymbol{\Lambda}$, $\boldsymbol{R}$ and $\boldsymbol{L}$ denote the matrices of eigenvalues, right eigenvectors and left eigenvectors, respectively. Finally, the expression of the matrix $|\boldsymbol{A}_n(\boldsymbol{U}^{\star})|$ is recalled, namely $|\boldsymbol{A}_n(\boldsymbol{U}^{\star})| := \boldsymbol{R}|\boldsymbol{\Lambda}|\boldsymbol{L}$, with $|\boldsymbol{\Lambda}|$ is a diagonal matrix containing the absolute value of the eigenvalues in $\boldsymbol{\Lambda}$.

The expression of the matrices of eigenvectors and eigenvalues, $\boldsymbol{R}$, $\boldsymbol{L}$ and $\boldsymbol{\Lambda}$, can be found in the work by Rohde (2001).

Although more accurate than the Lax-Friedrichs flux, the Roe Riemann solver is not *positivity preserving* and it may produce nonphysical solutions in transonic and supersonic cases due to the violation of entropy conditions, as discussed by Quirk (1994) or Perthame and Shu (1996). In this context, the linearised Roe solver is modified via a so-called *entropy fix* (EF) in order to recover the entropy conditions. The entropy fix by Harten and Hyman (1983) proposes the following modification of the Roe numerical flux

$$\widehat{\boldsymbol{F}(\boldsymbol{U})\boldsymbol{n}^{\pm}} = \frac{1}{2}\left[\boldsymbol{F}(\boldsymbol{U}^+) + \boldsymbol{F}(\boldsymbol{U}^-)\right]\boldsymbol{n}^{\pm} + \frac{1}{2}|\boldsymbol{A}_n^{\delta}(\boldsymbol{U}^{\star})|(\boldsymbol{U}^{\pm} - \boldsymbol{U}^{\mp}), \qquad \text{(B.3)}$$

where $|\boldsymbol{A}_n^{\delta}(\boldsymbol{U}^{\star})|$ denotes a dissipation matrix. The Harten-Hyman (HH) EF dissipation matrix is defined as $|\boldsymbol{A}_n^{\delta}(\boldsymbol{U}^{\star})| := \boldsymbol{R}\boldsymbol{\Phi}\boldsymbol{L}$, being $\boldsymbol{R}$ and $\boldsymbol{L}$ the right and

left eigenvector matrices previously introduced and $\boldsymbol{\Phi}$ a diagonal matrix such that $\Phi_{ii} = \max\left(|\lambda_i|, \delta\right)$, being λ_i the i-th eigenvalue of the matrix $\boldsymbol{A}_n(\boldsymbol{U}^\star)$ and $\delta > 0$ a user-defined threshold for the entropy fix.

Remark B.1. In the expression of the dissipation matrix, a user-defined threshold parameter $\delta > 0$ needs to be appropriately tuned to introduce the correct amount of extra diffusion for the problem under analysis. Note that, generally, $\delta \ll \lambda_{\mathtt{max}}$. Nonetheless, this value is problem-dependent and may require an empirical tuning to provide the best performance of the Roe solver.

B.3 Harten-Lax-van Leer (HLL) Riemann solver

An alternative approach to remedy the entropy violation of the Roe solver is represented by the HLL Riemann solver, named after Harten et al. (1983). Such approach relies on a weighted average of the information in two neighbouring elements Ω^+ and Ω^- and leads to the following numerical flux

$$\widehat{\boldsymbol{F}(\boldsymbol{U})\boldsymbol{n}}^{\pm} = \left[\frac{s^+ \boldsymbol{F}(\boldsymbol{U}^+) - s^- \boldsymbol{F}(\boldsymbol{U}^-)}{s^+ - s^-}\right] \boldsymbol{n}^\pm + \frac{s^+ s^-}{s^+ - s^-}(\boldsymbol{U}^\pm - \boldsymbol{U}^\mp), \qquad \text{(B.4)}$$

where, respectively, $s^+ := \max\left(0, \boldsymbol{v}^\star \cdot \boldsymbol{n}^+ + c^\star\right)$ and $s^- := \min\left(0, \boldsymbol{v}^\star \cdot \boldsymbol{n}^+ - c^\star\right)$ denote the estimates of the largest and smallest wave speeds, with the corresponding signs.

B.4 HLLEM Riemann solver

Finally, the HLLEM Riemann solver is introduced by Einfeldt (1988) and Einfeldt et al. (1991) as a modification of the HLL Riemann solver, which approximates the complete wave structure of the Riemann problem. More precisely, differently from the HLL method, it introduces a special treatment for middle waves, ensuring an accurate description of contact waves and shear layers, as described by Dumbser and Balsara (2016). In addition, HLLEM inherits the positivity-preserving properties of HLL-type Riemann solvers, fulfilling entropy conditions without the need of the user defined entropy fix required by the Roe solver.

In particular, the HLLEM numerical flux is expressed as

$$\widehat{\boldsymbol{F}(\boldsymbol{U})\boldsymbol{n}}^{\pm} = \left[\frac{s^+ \boldsymbol{F}(\boldsymbol{U}^+) - s^- \boldsymbol{F}(\boldsymbol{U}^-)}{s^+ - s^-}\right] \boldsymbol{n}^\pm + \frac{s^+ s^-}{s^+ - s^-}\boldsymbol{\theta}(\boldsymbol{U}^\star)(\boldsymbol{U}^\pm - \boldsymbol{U}^\mp), \qquad \text{(B.5)}$$

being s^+ and s^- the HLL estimates of the largest and smallest wave speeds previously introduced. In addition, it holds that $\boldsymbol{\theta}(\boldsymbol{U}^\star) = \boldsymbol{R}\boldsymbol{\Theta}\boldsymbol{L}$, where $\boldsymbol{\Theta}$ denotes the diagonal matrix $\boldsymbol{\Theta} = \mathrm{diag}\left(1, \theta^\star \mathbf{1}_{\mathrm{n_{sd}}}, 1\right)$ and $\theta^\star = |\boldsymbol{v}^\star \cdot \boldsymbol{n}|/(|\boldsymbol{v}^\star \cdot \boldsymbol{n}| + c^\star)$ is placed in the position of the eigenvalues corresponding to contact waves.

Note that, in contrast to HLL, the HLLEM flux reduces the amount of numerical dissipation associated to contact waves by means of the coefficient $\theta^\star < 1$. Moreover, it maintains an analogous treatment for shock waves and rarefactions, guarenteeing its entropy enforcement and positivity-preserving properties.

Appendix C

FCFV discretisation of the RANS equations

The FCFV formulation of the viscous laminar regime described in section 2 restricts the applicability of the proposed solver to a limited range of operating Reynolds numbers provided that they do not involve turbulent phenomena. Nonetheless, many realistic flows of interest in aerodynamic applications feature turbulent effects which need to be accounted by the corresponding CFD solvers by means of turbulence models, coupled to the system of conservation laws.

This appendix details the FCFV discretisation of the RANS equations equipped with an Spalart-Allmaras turbulence model. The accuracy properties of the resulting method are examined by means of a numerical example with manufactured analytical solution. The convergence results approach the optimal first-order accuracy for all the problem variables and a solid performance is achieved in meshes featuring a high stretching near the boundary layer. Indeed, the behaviour of the approximation in such stretched meshes outperforms the corresponding representation in analogous uniform grids.

This appendix is organised in the the following way. In C.1, the coupling of the Spalart-Allmaras one-equation model within the RANS equations is described. The resulting FCFV formulation is then briefly outlined in C.2. The convergence properties of the proposed formulation are described in C.3, where the simulation results for numerical test with manufactured analytical solution are introduced. Finally, C.4

summarises the main conclusions of this section.

C.1 The Spalart-Allmaras turbulence model for the RANS equations

The effect of turbulence is modelled in this study by means of the RANS equations and employing Boussinesq's assumption. Accordingly, the Navier-Stokes equations detailed in (2.1) are modified by means of augmented viscous stresses and heat flux. In this manner, a turbulent viscosity μ_t and turbulent thermal conductivity, described by means of the turbulent Prandt number Pr_t, which takes the constant value $Pr_t = 0.9$, are introduced to the viscous stresses and heat flux as

$$\boldsymbol{\sigma}^d = \frac{\mu + \mu_t}{Re} \left(2 \boldsymbol{\nabla}^{\mathrm{s}} \boldsymbol{v} - \frac{2}{3} (\boldsymbol{\nabla} \cdot \boldsymbol{v}) \mathbf{I}_{\mathrm{n_{sd}}} \right), \quad \boldsymbol{q} = \frac{1}{Re} \left(\frac{\mu}{Pr} + \frac{\mu_t}{Pr_t} \right) \boldsymbol{\nabla} T. \tag{C.1}$$

Moreover, note that the different variables appearing in the equations denote now time-averaged quantities.

The use of Boussinesq's analogy requires a turbulence model for the closure of the RANS equations. In this study, the non-tripped one-equation turbulence model by Spalart and Allmaras (1992) (SA) is considered, with the corresponding modifications proposed by Allmaras et al. (2012), which is expressed in nondimensional form as

$$\frac{\partial \rho \widetilde{\nu}}{\partial t} + \boldsymbol{\nabla} \cdot \left(\widetilde{\boldsymbol{f}} - \widetilde{\boldsymbol{g}} \right) = \widetilde{s}, \tag{C.2}$$

where the convective flux $\widetilde{\boldsymbol{f}}$, the diffusive flux $\widetilde{\boldsymbol{g}}$ and the source term $\widetilde{s}$ are given by

$$\widetilde{\boldsymbol{f}} = \rho \widetilde{\nu} \boldsymbol{v}, \tag{C.3}$$

$$\widetilde{\boldsymbol{g}} = \frac{\mu + \rho \widetilde{\nu}}{\sigma Re} \boldsymbol{\nabla} \widetilde{\nu}, \tag{C.4}$$

$$\widetilde{s} = c_{b1} \widetilde{S} \rho \widetilde{\nu} - \frac{1}{Re} c_{w1} f_w \frac{\rho \widetilde{\nu}^2}{d^2} + \frac{1}{\sigma Re} \left[c_{b2} \rho \boldsymbol{\nabla} \widetilde{\nu} - \left(\frac{\mu}{\rho} + \widetilde{\nu} \right) \boldsymbol{\nabla} \rho \right] \cdot \boldsymbol{\nabla} \widetilde{\nu}. \tag{C.5}$$

Moreover, the eddy viscosity is described as

$$\mu_t = \rho \widetilde{\nu} f_{v1}, \tag{C.6}$$

and the following relations hold

$$\chi = \frac{\rho\widetilde{\nu}}{\mu}, \qquad f_{v1} = \frac{\chi^3}{\chi^3 + c_{v1}^3}, \qquad f_{v2} = 1 - \frac{\chi}{1 + \chi f_{v1}}, \qquad \widetilde{S} = \|\boldsymbol{\omega}\| + \frac{1}{Re}\frac{\widetilde{\nu}}{\widetilde{\kappa}^2 d^2}f_{v2},$$

$$r = \min\left(\frac{1}{Re}\frac{\widetilde{\nu}}{\widetilde{S}\widetilde{\kappa}^2 d^2}, r_{\lim}\right), \quad g = r + c_{w2}(r^6 - r), \quad f_w = g\left[\frac{1 + c_{w3}^6}{g^6 + c_{w3}^6}\right]^{1/6}.$$

$$\text{(C.7)}$$

In these expressions, $\boldsymbol{\omega} = \nabla \times \boldsymbol{v}$ denotes the vorticity and d is the distance from a given point to the nearest wall. In addition, the set of constants appearing in the above expressions are given by: $c_{b1} = 0.1355$, $c_{b2} = 0.622$, $\sigma = 2/3$, $\widetilde{\kappa} = 0.41$, $c_{w1} = c_{b1}/\widetilde{\kappa}^2 + (1 + c_{b2})/\sigma$, $c_{w2} = 0.3$, $c_{w3} = 2$ and $c_{v1} = 7.1$.

Finally, the problem is closed with the prescription of boundary conditions for the SA model. In particular, a characteristics approach is employed at the far-field, setting $\rho\widetilde{\nu} = 0.1\mu_\infty$ at inflows, whereas $\rho\widetilde{\nu} = 0$ is defined at viscous walls.

C.2 FCFV formulation of the RANS equations with Spalart-Allmaras turbulence model

Following from the derivation of the FCFV method for the compressible Navier-Stokes equations, the corresponding FCFV formulation of the system of PDEs that results from appending the SA turbulence model to the RANS equations is briefly outlined in this section.

C.2.1 A mixed hybrid formulation of the RANS equations

First, the mixed formulation of the Spalart-Allmaras equation is considered in order to formulate the problem as a system of first-order PDEs. To this end, an additional equation expressing the gradient of the eddy viscosity as mixed variable of the problem is introduced, namely, $\boldsymbol{\eta} = \nabla\widetilde{\nu}$. Accordingly, the viscous flux and source term are expressed in terms of $\boldsymbol{\eta}$ as

$$\widetilde{\boldsymbol{g}} = \frac{\mu + \rho\widetilde{\nu}}{\sigma Re}\boldsymbol{\eta},$$

$$\widetilde{s} = c_{b1}\widetilde{S}\rho\widetilde{\nu} - \frac{1}{Re}c_{w1}f_w\frac{\rho\widetilde{\nu}^2}{d^2} + \frac{1}{\sigma Re}\left[c_{b2}\rho\boldsymbol{\eta} - \left(\frac{\mu}{\rho} + \widetilde{\nu}\right)\nabla\rho\right]\cdot\boldsymbol{\eta}.$$

$$\text{(C.8)}$$

At this point, following the FCFV rationale described in 2.2.2, the mixed hybrid FV formulation of the RANS equations is presented as follows, allowing the numerical scheme to solve the problem in two phases via hybridisation.

Therefore, consider the set of hybrid variables of the problem $(\widehat{\boldsymbol{U}}, \widehat{\rho\widetilde{\nu}})$ denoting the traces of the solution on $\Gamma \cup \partial\Omega$. Then, the $\mathtt{n_{el}}$ FCFV local problems describing the RANS equations in each cell Ω_e, for $e = 1, \ldots, \mathtt{n_{el}}$ are written as

$$
\begin{cases}
\boldsymbol{\varepsilon}^d - \mathcal{D}\boldsymbol{\nabla}^{\mathtt{S}}\boldsymbol{v} = \boldsymbol{0} & \text{in } \Omega_e \times (0, \mathrm{T_{end}}], \\
\boldsymbol{\phi} - \boldsymbol{\nabla}T = \boldsymbol{0} & \text{in } \Omega_e \times (0, \mathrm{T_{end}}], \\
\boldsymbol{\eta} - \boldsymbol{\nabla}\widetilde{\nu} = \boldsymbol{0} & \text{in } \Omega_e \times (0, \mathrm{T_{end}}], \\
\dfrac{\partial \boldsymbol{U}}{\partial t} + \boldsymbol{\nabla} \cdot \big(\boldsymbol{F}(\boldsymbol{U}) - \boldsymbol{G}(\boldsymbol{U}, \rho\widetilde{\nu}, \boldsymbol{\varepsilon}^d, \boldsymbol{\phi})\big) = \boldsymbol{0} & \text{in } \Omega_e \times (0, \mathrm{T_{end}}], \\
\dfrac{\partial \rho\widetilde{\nu}}{\partial t} + \boldsymbol{\nabla} \cdot \big(\widetilde{\boldsymbol{f}}(\boldsymbol{U}, \rho\widetilde{\nu}) - \widetilde{\boldsymbol{g}}(\boldsymbol{U}, \rho\widetilde{\nu}, \boldsymbol{\eta})\big) = \widetilde{s} & \text{in } \Omega_e \times (0, \mathrm{T_{end}}], \\
(\boldsymbol{U}, \rho\widetilde{\nu}) = (\boldsymbol{U}^0, \rho\widetilde{\nu}^0) & \text{in } \Omega_e \times \{0\}, \\
(\boldsymbol{U}, \rho\widetilde{\nu}) = (\widehat{\boldsymbol{U}}, \widehat{\rho\widetilde{\nu}}) & \text{on } \partial\Omega_e \times (0, \mathrm{T_{end}}],
\end{cases}
\tag{C.9}
$$

where $(\boldsymbol{U}, \rho\widetilde{\nu}, \boldsymbol{\varepsilon}^d, \boldsymbol{\phi}, \boldsymbol{\eta})$ denote, correspondingly, the primal and mixed variables of the problem, defining the solution inside each cell as function of the hybrid counterparts $(\widehat{\boldsymbol{U}}, \widehat{\rho\widetilde{\nu}})$.

Then, the FCFV global problem prescribing boundary conditions on $\partial\Omega$ and the so-called *transmission conditions* to ensure continuity of the solution and of the normal fluxes on Γ is defined to compute the solution of the hybrid unknowns $(\widehat{\boldsymbol{U}}, \widehat{\rho\widetilde{\nu}})$, namely

$$
\begin{cases}
[\![\big(\boldsymbol{F}(\boldsymbol{U}) - \boldsymbol{G}(\boldsymbol{U}, \rho\widetilde{\nu}, \boldsymbol{\varepsilon}^d, \boldsymbol{\phi})\big)\boldsymbol{n}]\!] = \boldsymbol{0} & \text{on } \Gamma \times (0, \mathrm{T_{end}}], \\
[\![\big(\widetilde{\boldsymbol{f}}(\boldsymbol{U}, \rho\widetilde{\nu}) - \widetilde{\boldsymbol{g}}(\boldsymbol{U}, \rho\widetilde{\nu}, \boldsymbol{\eta})\big) \cdot \boldsymbol{n}]\!] = 0 & \text{on } \Gamma \times (0, \mathrm{T_{end}}], \\
\widehat{\boldsymbol{B}}(\boldsymbol{U}, \widehat{\boldsymbol{U}}, \boldsymbol{\varepsilon}^d, \boldsymbol{\phi}) = \boldsymbol{0}, & \text{on } \partial\Omega \times (0, \mathrm{T_{end}}], \\
\widehat{b}\,(\widehat{\boldsymbol{U}}, \rho\widetilde{\nu}, \widehat{\rho\widetilde{\nu}}) = 0, & \text{on } \partial\Omega \times (0, \mathrm{T_{end}}].
\end{cases}
\tag{C.10}
$$

In these expressions, the usual notation for the unit normal vector and the jump operator is employed, whereas $\widehat{\boldsymbol{B}}$ is the boundary operator described in section 2.2.3. Similarly, an additional boundary operator, $\widehat{b}$, is introduced, being responsible for imposing boundary conditions for the SA model.

Note that, in order to reduce the notation, the transmission conditions imposing continuity of the solution are not expressed in equation (C.10). Indeed, they are automatically satisfied due to the Dirichlet boundary conditions imposed in the local

problems (C.9) and by the unique definition of the hybrid variables $(\widehat{\boldsymbol{U}}, \widehat{\rho\widetilde{\nu}})$ on each face.

C.2.2   Integral form of the local and global problems

The integral form of the FCFV local problems is obtained at each cell Ω_e, $e = 1, \ldots, \mathbf{n_{el}}$, by applying the divergence theorem to equation (C.9) Then, given $(\boldsymbol{U}, \rho\widetilde{\nu}) = (\boldsymbol{U}^0, \rho\widetilde{\nu}^0)$ at the initial time $t = 0$, it holds

$$\int_{\Omega_e} \boldsymbol{\varepsilon}^d \, d\Omega - \int_{\partial\Omega_e} \mathcal{D}\widehat{\boldsymbol{v}} \otimes \boldsymbol{n} \, d\Gamma = \mathbf{0}, \tag{C.11a}$$

$$\int_{\Omega_e} \boldsymbol{\phi} \, d\Omega - \int_{\partial\Omega_e} \widehat{T}\boldsymbol{n} \, d\Gamma = \mathbf{0}, \tag{C.11b}$$

$$\int_{\Omega_e} \boldsymbol{\eta} \, d\Omega - \int_{\partial\Omega_e} \widehat{\widetilde{\nu}}\boldsymbol{n} \, d\Gamma = \mathbf{0}, \tag{C.11c}$$

$$\int_{\Omega_e} \frac{\partial \boldsymbol{U}}{\partial t} \, d\Omega + \int_{\partial\Omega_e} \left(\widehat{\boldsymbol{F}(\boldsymbol{U})\boldsymbol{n}} - \widehat{\boldsymbol{G}(\boldsymbol{U}, \rho\widetilde{\nu}, \boldsymbol{\varepsilon}^d, \boldsymbol{\phi})\boldsymbol{n}} \right) d\Gamma = \mathbf{0}, \tag{C.11d}$$

$$\int_{\Omega_e} \frac{\partial \rho\widetilde{\nu}}{\partial t} \, d\Omega + \int_{\partial\Omega_e} \left(\widehat{\widetilde{\boldsymbol{f}}(\boldsymbol{U}, \rho\widetilde{\nu}) \cdot \boldsymbol{n}} - \widehat{\widetilde{\boldsymbol{g}}(\boldsymbol{U}, \rho\widetilde{\nu}, \beta) \cdot \boldsymbol{n}} \right) d\Gamma = \int_{\Omega_e} \widetilde{s} \, d\Omega, \tag{C.11e}$$

where $\widehat{\boldsymbol{v}}$, $\widehat{T}$ and $\widehat{\widetilde{\nu}}$ denote, respectively, the velocity, temperature and kinematic eddy viscosity fields on the cell faces $\partial\Omega_e$, defined in terms of the hybrid variables.

On the other hand, the integral form of the global problem (C.10) is given by

$$\sum_{e=1}^{\mathbf{n_{el}}} \left\{ \int_{\partial\Omega_e\backslash\partial\Omega} \left(\widehat{\boldsymbol{F}(\boldsymbol{U})\boldsymbol{n}} - \widehat{\boldsymbol{G}(\boldsymbol{U}, \rho\widetilde{\nu}, \boldsymbol{\varepsilon}^d, \boldsymbol{\phi})\boldsymbol{n}} \right) d\Gamma + \int_{\partial\Omega_e\cap\partial\Omega} \widehat{\boldsymbol{B}}(\boldsymbol{U}, \widehat{\boldsymbol{U}}, \boldsymbol{\varepsilon}^d, \boldsymbol{\phi}) \, d\Gamma \right\} = \mathbf{0}, \tag{C.12a}$$

$$\sum_{e=1}^{\mathbf{n_{el}}} \left\{ \int_{\partial\Omega_e\backslash\partial\Omega} \left(\widehat{\widetilde{\boldsymbol{f}}(\boldsymbol{U}, \rho\widetilde{\nu}) \cdot \boldsymbol{n}} - \widehat{\widetilde{\boldsymbol{g}}(\boldsymbol{U}, \rho\widetilde{\nu}, \boldsymbol{\eta}) \cdot \boldsymbol{n}} \right) d\Gamma + \int_{\partial\Omega_e\cap\partial\Omega} \widehat{b}\left(\widehat{\boldsymbol{U}}, \rho\widetilde{\nu}, \widehat{\rho\widetilde{\nu}}\right) d\Gamma \right\} = 0, \tag{C.12b}$$

which allows to solve the problem for the hybrid unknowns, $\widehat{\boldsymbol{U}}$ and $\widehat{\rho\widetilde{\nu}}$.

Note that the terms $\widehat{\boldsymbol{F}(\boldsymbol{U})\boldsymbol{n}}$ and $\widehat{\boldsymbol{G}(\boldsymbol{U}, \rho\widetilde{\nu}, \boldsymbol{\varepsilon}^d, \boldsymbol{\phi})\boldsymbol{n}}$ appearing in equations (C.11d) and (C.12a) stand for the convection and diffusion numerical fluxes described in section 2.2.4, given by

$$\widehat{\boldsymbol{F}(\boldsymbol{U})\boldsymbol{n}} = \boldsymbol{F}(\widehat{\boldsymbol{U}})\boldsymbol{n} + \boldsymbol{\tau}^a(\widehat{\boldsymbol{U}})\,(\boldsymbol{U} - \widehat{\boldsymbol{U}}), \tag{C.13a}$$

$$\widehat{\boldsymbol{G}(\boldsymbol{U}, \rho\widetilde{\nu}, \boldsymbol{\varepsilon}^d, \boldsymbol{\phi})\boldsymbol{n}} = \boldsymbol{G}(\widehat{\boldsymbol{U}}, \widehat{\rho\widetilde{\nu}}, \boldsymbol{\varepsilon}^d, \boldsymbol{\phi})\boldsymbol{n} - \boldsymbol{\tau}^d\,(\boldsymbol{U} - \widehat{\boldsymbol{U}}), \tag{C.13b}$$

where the diffusive stabilisation term $\boldsymbol{\tau}^d$ is given by equation 2.20 and the advective stabilisation matrix is defined in terms of the corresponding Riemann solver employed for the simulation, as detailed in section 2.2.5.

Similarly, equations (C.11e) and (C.12b) introduce the advective and diffusive numerical fluxes for the SA equation, which are described by

$$\widehat{\widetilde{\boldsymbol{f}}(\boldsymbol{U}, \rho\widetilde{\nu}) \cdot \boldsymbol{n}} = \widetilde{\boldsymbol{f}}(\widehat{\boldsymbol{U}}, \widehat{\rho\widetilde{\nu}}) \cdot \boldsymbol{n}_j + \widetilde{\tau}^a(\widehat{\boldsymbol{U}})\,(\rho\widetilde{\nu} - \widehat{\rho\widetilde{\nu}}), \tag{C.14a}$$

$$\widehat{\widetilde{\boldsymbol{g}}(\boldsymbol{U}, \rho\widetilde{\nu}, \beta) \cdot \boldsymbol{n}} = \widetilde{\boldsymbol{g}}(\widehat{\boldsymbol{U}}, \widehat{\rho\widetilde{\nu}}, \boldsymbol{\eta}) \cdot \boldsymbol{n} - \widetilde{\tau}^d\,(\rho\widetilde{\nu} - \widehat{\rho\widetilde{\nu}}). \tag{C.14b}$$

where the corresponding diffusive and advective stabilisation terms are defined as

$$\widetilde{\tau}^d = \frac{1}{Re}, \qquad \widetilde{\tau}^a = |\widehat{\boldsymbol{v}} \cdot \boldsymbol{n}|. \tag{C.15}$$

Note that the corresponding stabilisation terms are decoupled from the conservation variables and just affect the jumps on the turbulent viscosity. Moreover, notice that the SA convective numerical flux is defined following the spirit of the approximation of Riemann solvers, employing a Roe-like strategy that provides an upwinded flux.

C.2.3 FCFV discrete problem

Finally, the discrete forms of the FCFV local and global problems arise from the evaluation of the corresponding integral forms of these problems, provided that the discretisation of the primal, mixed and hybrid variables consists of the constant value at the centroid of the corresponding cells and faces.

Indeed, the FCFV discrete form of the local problems (C.9) is: given the initial state $(\boldsymbol{U}, \rho\widetilde{\nu}) = (\boldsymbol{U}^0, \rho\widetilde{\nu}^0)$ at time $t = 0$ and the hybrid quantities $\widehat{\boldsymbol{U}}_j$ and $\widehat{\rho\widetilde{\nu}}_j$ on the faces $\Gamma_{e,j}$, $j = 1, \ldots, \mathtt{n}_{\mathtt{fa}}^e$, compute $(\boldsymbol{U}_e, \rho\widetilde{\nu}_e, \boldsymbol{\varepsilon}_e^d, \boldsymbol{\phi}_e, \boldsymbol{\eta}_e)$ at each cell Ω_e, for $e = 1, \ldots, \mathtt{n}_{\mathtt{el}}$, satisfying

$$|\Omega_e|\boldsymbol{\varepsilon}_e^d - \sum_{j \in \mathcal{A}_e} |\Gamma_{e,j}|\mathcal{D}\widehat{\boldsymbol{v}}_j \otimes \boldsymbol{n}_j = \boldsymbol{0}, \tag{C.16a}$$

$$|\Omega_e|\boldsymbol{\phi}_e - \sum_{j \in \mathcal{A}_e} |\Gamma_{e,j}|\widehat{T}_j \boldsymbol{n}_j = \boldsymbol{0}, \tag{C.16b}$$

$$|\Omega_e|\boldsymbol{\eta}_e - \sum_{j \in \mathcal{A}_e} |\Gamma_{e,j}|\widehat{\widetilde{\nu}}_j \boldsymbol{n}_j = \boldsymbol{0}, \tag{C.16c}$$

$$|\Omega_e|\frac{d\boldsymbol{U}_e}{dt} + \sum_{j \in \mathcal{A}_e} |\Gamma_{e,j}|\left\{ \boldsymbol{F}(\widehat{\boldsymbol{U}}_j)\boldsymbol{n}_j - \boldsymbol{G}(\widehat{\boldsymbol{U}}_j, \widehat{\rho\widetilde{\nu}}_j, \boldsymbol{\varepsilon}_e^d, \boldsymbol{\phi}_e)\boldsymbol{n}_j \right.$$
$$\left. + \left(\boldsymbol{\tau}^a(\widehat{\boldsymbol{U}}_j) + \boldsymbol{\tau}^d\right)(\boldsymbol{U}_e - \widehat{\boldsymbol{U}}_j)\right\} = \boldsymbol{0}, \tag{C.16d}$$

$$|\Omega_e|\frac{d\rho\widetilde{\nu}_e}{dt} + \sum_{j\in\mathcal{A}_e}|\Gamma_{e,j}|\left\{\widetilde{\boldsymbol{f}}(\widehat{\boldsymbol{U}}_j, \widehat{\rho\widetilde{\nu}_j})\cdot\boldsymbol{n}_j - \widetilde{\boldsymbol{g}}(\widehat{\boldsymbol{U}}_j, \widehat{\rho\widetilde{\nu}_j}, \boldsymbol{\eta}_e)\cdot\boldsymbol{n}_j\right.$$
$$\left.+\left(\widetilde{\tau}^a(\widehat{\boldsymbol{U}}_j) + \widetilde{\tau}^d\right)(\rho\widetilde{\nu}_e - \widehat{\rho\widetilde{\nu}_j})\right\} = |\Omega_e|\widetilde{s}_e, \tag{C.16e}$$

where, $|\Omega_e|\widetilde{s}_e = \int_{\Omega_e}\widetilde{s}d\Omega$ in equation (C.16e) is computed employing a quadrature rule based on a single integration point.

Similarly, the discrete form arising from the FCFV global problem (C.10) reads: find $\widehat{\boldsymbol{U}}$ and $\widehat{\rho\widetilde{\nu}}$ such that

$$\sum_{e=1}^{\mathtt{n_{el}}}|\Gamma_{e,i}|\left\{\left[\boldsymbol{F}(\widehat{\boldsymbol{U}}_i)\boldsymbol{n}_i - \boldsymbol{G}(\widehat{\boldsymbol{U}}_i, \widehat{\rho\widetilde{\nu}_i}, \boldsymbol{\varepsilon}_e^d, \boldsymbol{\phi}_e)\boldsymbol{n}_i + \left(\boldsymbol{\tau}^a(\widehat{\boldsymbol{U}}_i) + \boldsymbol{\tau}^d\right)(\boldsymbol{U}_e - \widehat{\boldsymbol{U}}_i)\right]\chi_{\mathcal{I}_e}(i)\right.$$
$$\left.+\widehat{\boldsymbol{B}}(\boldsymbol{U}_e, \widehat{\boldsymbol{U}}_i, \boldsymbol{\varepsilon}_e^d, \boldsymbol{\phi}_e)\chi_{\mathcal{E}_e}(i)\right\} = \boldsymbol{0}, \tag{C.17a}$$

$$\sum_{e=1}^{\mathtt{n_{el}}}|\Gamma_{e,i}|\left\{\left[\widetilde{\boldsymbol{f}}(\widehat{\boldsymbol{U}}_i, \widehat{\rho\widetilde{\nu}_i})\cdot\boldsymbol{n}_i - \widetilde{\boldsymbol{g}}(\widehat{\boldsymbol{U}}_i, \widehat{\rho\widetilde{\nu}_i}, \boldsymbol{\eta}_e)\cdot\boldsymbol{n}_i + \left(\widetilde{\tau}^a(\widehat{\boldsymbol{U}}_i) + \widetilde{\tau}^d\right)(\rho\widetilde{\nu}_e - \widehat{\rho\widetilde{\nu}_i})\right]\chi_{\mathcal{I}_e}(i)\right.$$
$$\left.+\widehat{b}(\widehat{\boldsymbol{U}}_i, \rho\widetilde{\nu}_e, \widehat{\rho\widetilde{\nu}_i})\chi_{\mathcal{E}_e}(i)\right\} = 0, \tag{C.17b}$$

for all $i\in\mathcal{A}_e$.

Finally, the FCFV discrete forms of the local and global problems, (C.16) and (C.17), are linearised via the Newton-Raphson method. The resulting linear systems of equations are then solved via a hybridisation procedure in an analogous way as described in section 2.2.7.

C.3 Numerical convergence study

The convergence properties of the FCFV approximation of the RANS equations with the Spalart-Allmaras model have been examined by means of an example with manufactured analytical solution introduced by Eça et al. (2007) and Rumsey and Thomas (2008).

The computational domain of the problem consists of the square domain $\Omega = [0.6L, L]\times[0, 0.4L]$, with $L = 1$ being the characteristic length of the problem. Then,

the different flowfield variables are defined as

$$\boldsymbol{v} = \left\{ \begin{array}{c} \mathrm{erf}(\eta) \\ \left(1 - \exp^{-\eta^2}\right) / \left(\sigma\sqrt{\pi}\right) \end{array} \right\}, \qquad T = \frac{1}{(\gamma - 1)M_\infty^2},$$
$$p = 0.5 \log\left(2x - x^2 + 0.25\right) \log\left(4y^3 - 3y^2 + 1.25\right), \qquad \text{(C.18)}$$
$$\widetilde{\nu} = \widetilde{\nu}_{\max}\sqrt{2}\eta_\nu \exp^{0.5 - \eta_\nu^2}$$

where $\eta = \sigma y / x$ and $\eta_\nu = \sigma_\nu y / x$ are similarity variables, with $\sigma = 4$ and $\sigma_\nu = 2.5$, $\widetilde{\nu}_{\max} = 10^3\nu$ and erf stands for the error function. In addition, the non-dimensional quantities of the problem are given by $Re = 10^6$ and $M_\infty = 0.2$. Finally, the source term of the problem and the corresponding boundary conditions on $\partial\Omega$ are computed from the analytical solution.

Four sets of meshes arising from the combination of triangular and quadrilateral cells, and with stretching factor $s = 0$ (uniform meshes) and $s = 1000$ (high stretching) are used in this study.

The eddy viscosity field, $\widetilde{\nu}$, obtained in two different refinements of uniform and stretched meshes of triangular elements and employing an HLLEM Riemann solver is displayed in figure C.1.

(a) Triangles M4   (b) Triangles M7   (c) Triangles M4S   (d) Triangles M7S
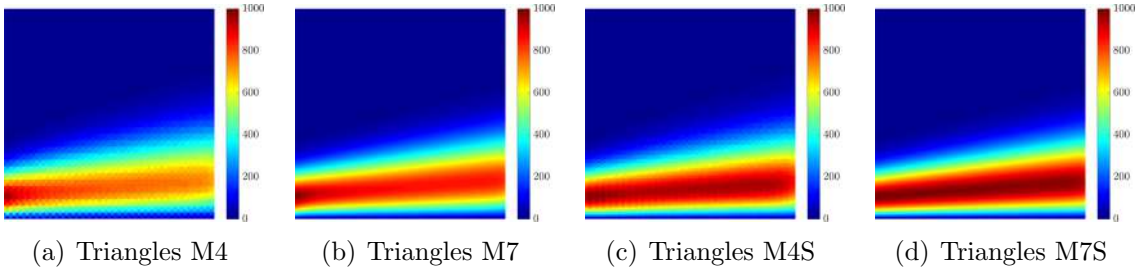
Figure C.1: Turbulent flow with manufactured solution - Eddy viscosity field obtained in (a-b) uniform and (c-d) stretched meshes of triangular elements using an HLLEM Riemann solver.

Similarly, figure C.2 reports the Mach number distribution obtained in different refinements of stretched meshes of triangular and quadrilateral cells.

Those figures illustrate the positive effect of mesh refinement and, foremost, of a high stretching near the bottom boundary over the quality of the approximation. Indeed, the increased resolution provided in the boundary layer allows the eddy viscosity field to develop appropriately and reach its maximum value in the domain.

(a) Quadrilaterals M4S (b) Quadrilaterals M7S (c) Triangles M4S (d) Triangles M7S
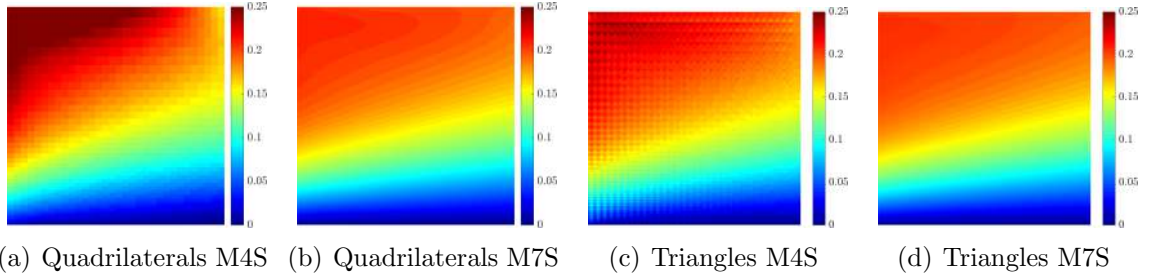
Figure C.2: Turbulent flow with manufactured solution - Mach number distribution using stretched meshes of (a-b) quadrilateral and (c-d) triangular cells and an HLLEM Riemann solver.

Figure C.3 reports the h-convergence study performed in the set of triangular meshes with high stretching, which is taken as baseline, employing the four Riemann solvers described in section 2.2.5.
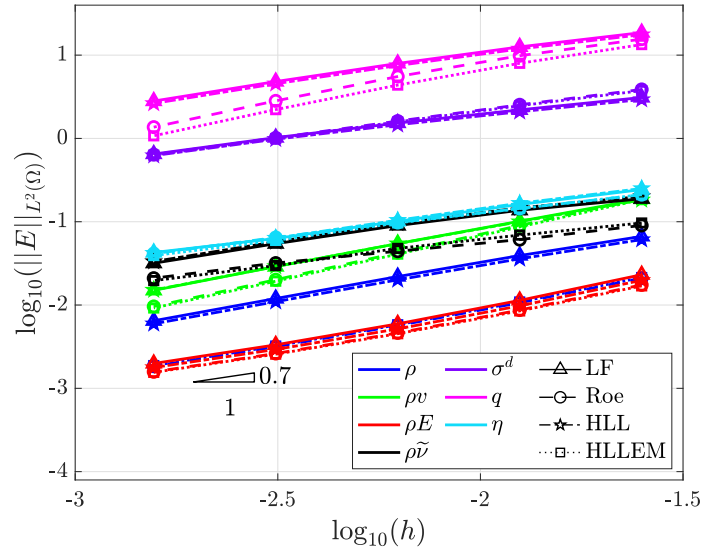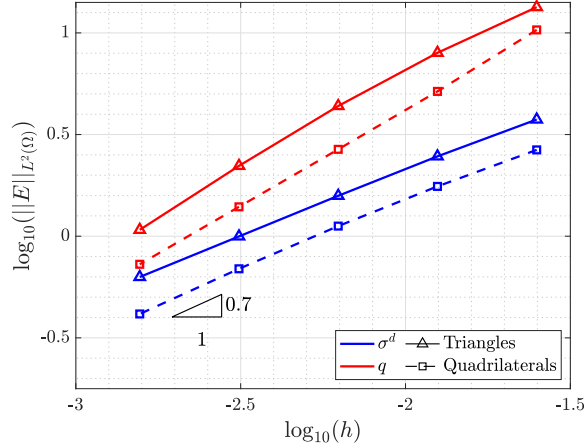

Figure C.3: Turbulent flow with manufactured solution - h-convergence of the error of the flowfield variables in the $\mathcal{L}_2(\Omega)$ norm, using Lax-Friedrichs (LF), Roe, HLL and HLLEM Riemann solvers.

A good evolution of the error is observed, with the respective rates of convergence approaching the optimal rate 1. However, notice the high levels of error displayed by the approximation of the stress tensor and the heat flux. These issues are attributed to the high variations experienced by the flowfield and the tendency of numerical approximations to display suboptimal accuracy in the convective limit.

In addition, the effect of the type of elements of the mesh —triangles or quadrilaterals— is studied in the corresponding sets of stretched meshes, and displayed in figure C.4.

Since differences among the approximations are only observed for the stress tensor and heat flux, only these two variables are reported. Despite displaying nearly

Figure C.4: Turbulent flow with manufactured solution - h-convergence of the error of stress tensor and heat flux in the $\mathcal{L}_2(\Omega)$ norm employing stretched meshes of triangular and quadrilateral cells and using an HLLEM Riemann solver.

identical rates of convergence, lower levels of error are obtained in the meshes of quadrilateral cells. These results confirm the increased accuracy delivered by meshes of quadrilateral cells in the vicinity of walls and in the boundary layer

These results confirm the advantages of using quadrilateral meshes in boundary layers, which are able to provide higher accuracy in the vicinity of walls, as reported by Drosson et al. (2013) and Moro et al. (2017).

Finally, the effect of the mesh stretching, displayed qualitatively in the approximation of the eddy viscosity in figure C.1, is quantified by means of the evolution of the error of such variable and its gradient as function of the mesh size. The h-convergence study is detailed in figure C.5 and confirms the increased accuracy obtained in highly stretched meshes providing very fine grid spacing near the wall in order to accurately resolve these quantities in the boundary layer. Indeed, whereas the approximation obtained in stretched meshes tends to approach the optimal rate of convergence, the level of error of the corresponding curves on uniform meshes stagnates.

C.4   Conclusions

The face-centred finite volume (FCFV) method has been presented for the simulation of steady state compressible flows by means of its formulation of the Reynolds-
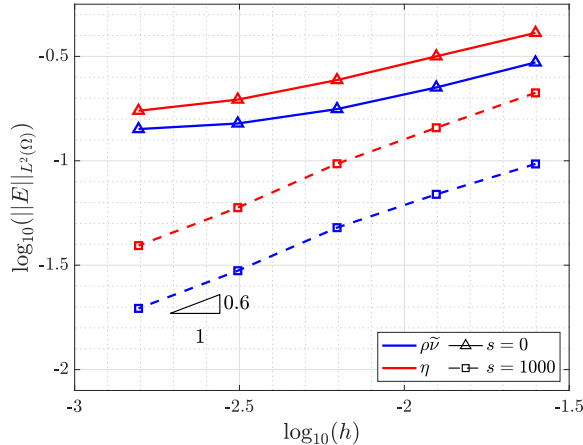
Figure C.5: Turbulent flow with manufactured solution - h-convergence of the error of the eddy viscosity and its gradient in the $\mathcal{L}_2(\Omega)$ norm employing uniform and stretched meshes of triangular cells and using an HLLEM Riemann solver.

averaged Navier-Stokes (RANS) equations employing an Spalart-Allmaras (SA) turbulence model. The proposed numerical scheme extends the formulation devised for laminar viscous compressible flows and devises a mixed hybrid FV approach for the augmented system of equations.

The presented methodology has been tested by means of a numerical example with manufactured analytical solution. It is important to emphasise that these kind of analyses are restricted to significant limitations, since they are based on the description of unrealistic flows. For this reason, despite allowing a first estimation of the performance of the method, the following conclusions cannot be firmly established as absolute judgements.

The FCFV method displays optimal first-order accuracy for the different variables of the problem, i.e. density, momentum, energy, eddy viscosity, stress tensor, heat flux and eddy viscosity gradient. Likewise in the laminar regime, the proposed methodology does not require a reconstruction of the gradients and retains the accuracy properties even in meshes displaying a high stretching. In particular, the presence of highly stretched cells near the boundary layer results fundamental for a good approximation of the flowfield. Conversely, uniform meshes have not been able to provide reasonable accuracy levels. Finally, numerical results have also confirmed the increased accuracy obtained in quadrilateral meshes for the approximation of the mixed variables, that is stress tensor and heat flux.

Overall, these preliminary results suggest a close match between the capabilities of the FCFV paradigm and the current needs of conventional FV methodologies.

141

Indeed, the optimal accuracy delivered in meshes featuring a high grid stretching and its versatility to employ different cell types or hybrid meshes describe some of the advantages of the proposed FCFV approach with respect to traditional FV solvers, motivating its further development for the simulation of such kind of flows.